Imperial College London

Strain Path Dependence in Ferritic Steel Polycrystals

Author:

Tomiwa O. Erinosho

Supervisor:

Prof. F.P.E. Dunne

Submitted in part fulfilment of the requirements for the degree of Doctor of Philosophy in Materials of Imperial College London,

February 2015

Declaration of Authorship

I, Tomiwa O. Erinosho, declare that this thesis titled, `Strain Path Dependence in Ferritic Steel Polycrystals' and the work presented in it are my own. I confirm that:

- This work was done wholly or mainly while in candidature for a research degree at Imperial College London.
- Where any part of this thesis has previously been submitted for a degree or any other qualification at this University or any other institution, this has been clearly stated.
- Where I have consulted the published work of others, this is always clearly attributed.
- Where I have quoted from the work of others, the source is always given. With the exception of such quotations, this thesis is entirely my own work.
- I have acknowledged all main sources of help.
- Where the thesis is based on work done by myself jointly with others, I have made clear exactly what was done by others and what I have contributed myself.

Signed: 

Date: 19th February, 2015

Copyright

The copyright of this thesis rests with the author and is made available under a Creative Commons Attribution Non-Commercial No Derivatives licence. Researchers are free to copy, distribute or transmit the thesis on the condition that they attribute it, that they do not use it for commercial purposes and that they do not alter, transform or build upon it. For any reuse or redistribution, researchers must make clear to others the licence terms of this work.

Contents

List of Figures **6**

Nomenclature **14**

Acknowledgements **16**

Abstract **17**

1. Strain path effects in ferritic steel polycrstals **19**

2. Plasticity fundamentals and literature review **23**

2.1. Slip systems in metal crystals 23

2.2. Critical resolved shear stress for slip (Schmid's Law) 26

2.3. Introduction to Dislocations 27

2.4. Material Characterization techniques 29

2.5. Crystal Plasticity Framework 38

3. Texture, Hardening and Non-proportionality of Strain in Ferritic Steel Polycrystals **44**

3.1. Investigation of non-proportional loading and hardening in single crystal BCC steel 44

3.2. Effects of non-proportional loading on dislocation structures and stress paths in BCC polycrystals 63

3.3. Conclusions 76

4. Coupled effects of texture, hardening and non-proportionality of strain on ductility in ferritic steel polycrystals **78**

4.1. 3-D model development, localization criterion and measure of non-proportionality 78

4.2. Predicted limit diagrams for proportional straining 84
4.3. Measure of non-proportionality 86
4.4. Effects of texture, hardening and non-proportionality on limit strain in BCC polycrystals 88
4.5. Conclusions 95

5. Lattice strain distributions due to elastic distortions and GND development in polycrystals 96
5.1. Lattice spacing changes due to deformation 96
5.1.1. Lattice spacing changes due to elastic distortions 100
5.1.2. Lattice spacing changes due to GND development 101
5.1.3. Lattice spacing changes due to elastic distortions and GNDs 108
5.2. Validation of methodology 108
5.2.1. Elastic distortions 109
5.2.2. Burger discontinuity and GND density 113
5.3. Lattice spacing distributions due to elastic distortions and development of GNDs 114
5.3.1. Analysis of single crystal FCC beam subject to four-point bending 117
5.3.2. Analysis of random and textured FCC polycrystals subject to uniaxial straining 127
5.4. Conclusions 132

6. Role of Texture and Hardening on simulated x-ray diffraction lattice strain measurements under non-proportional strain paths using crystal plasticity 134
6.1. X-ray diffraction modelling 134
6.2. X-ray diffraction lattice strain measurements 138
6.2.1. Single crystal simulations 139
6.2.2. Lattice strains in polycrystals 141
6.3. Effects of texture and hardening on lattice spacing distributions in ferritic steel polycrystals 146
6.4. Non-proportionality of strain and effects on lattice spacing distributions 160

6.4.1. Experimental measurement of lattice spacing changes under non-proportional strain paths 166
6.4.2. Normalized lattice spacing changes for non-proportional strain paths calculated using crystal plasticity 167
6.5. Conclusions 173

7. Conclusions and Future Work 175
7.1. Conclusions 175
7.2. Future work 177

Appendix A: Lattice spacing parameters for triclinic crystal 180

Appendix B: Strain gradient approximation method 181

Appendix C: Justification of calculation of the contribution to lattice distortion from the projection of the Burger's vector discontinuity onto a plane 182

Appendix D: Relationship between the GND deformation tensor d^{gnd} and the Burger's tensor, G 183

Appendix E: Diffraction peaks due to strains in a 2-D spatial field 184

References 185

List of Figures

Fig. 1-1: Non-proportional paths adopted to achieve strain state C such that strain path A involves biaxial followed by uniaxial straining and strain path B undergoes uniaxial followed by biaxial deformation 20

Fig. 2-1: Slip bands on a Titanium crystal deformed at room temperature [21]. 25

Fig. 2-2: Slip systems in FCC crystals. 25

Fig. 2-3: Slip systems in body centered cubic crystals (a) (101) and (101) planes (b) (110) and (110) planes (c) (011) and (011) planes. 25

Fig. 2-4: Slip systems in HCP crystals 26

Fig. 2-5: A single crystal containing slip plane with normal *n*, slip direction *s*, and loaded in direction *t*. 27

Fig. 2-6: Methodology for mechanical testing of limit strain in metals showing (a) Schematic of Nakajima apparatus and (b) test samples [29]. 31

Fig. 2-7: Schematic of the experimental Nakajima test showing an example of a marked sample in (a) and the plastic strain along section A-A denoting the safe and unsafe regions . 31

Fig. 2-8: Schematic of the x-ray diffraction process to obtain Debye Scherer rings showing an x-ray beam incident on a deforming sample leading to diffractions which are collected on an area detector 35

Fig. 2-9: Schematic diagram to show the experimental set up of an EBSD system in a SEM chamber [51]. 37

Fig. 3-1: Displacement controlled non-proportional strain paths. 46

Fig. 3-2: Stress states to activate slip on the slip planes of Fig. 3-3. The labeling corresponds to the families of slip systems indicated in Fig. 3-3 that are activated along different sections of the macroscopic yield surface 47

Fig. 3-3: Slip systems in body centered cubic crystals (a) (110) and (110) planes (b) (101) and (101) planes (c) (011) and (011) planes. 47

Fig. 3-4: (a) Non-proportional strain path B-5I imposed on the BCC single crystal based on isotropic latent-hardening, (b) stress path response for path B-5I, (c) the corresponding stress component responses and (d) the schematic Tresca yield surface representation for path B-5I. Note that $\varphi = \tan - 1v$. 51

Fig. 3-5: (a) Non-proportional strain path B-5S imposed on the BCC single crystal based on anisotropic self-hardening, (b) stress path for response for path B-5S, (c) the yield surface representation for B-5aS. Note that $\varphi = \tan - 1\upsilon$. 52

Fig. 3-6: Dislocation accumulation on slip systems during strain path B-5 (see Fig. 3-3 for slip systems types) (a) self-hardening (b) isotropic latent-hardening. 53

Fig. 3-7: (a) Stress response of the BCC single crystal subjected to the biaxial proportional and non-proportional strain paths shown for isotropic latent-hardening conditions, (b) Tresca yield surface representation showing the stress path followed and the yield surface mode of expansion. 59

Fig. 3-8: (a) Stress path response of the BCC single crystal subjected to non-proportional strain path B-2I for isotropic latent-hardening conditions and (b) the corresponding components of stress over the loading history. 59

Fig. 3-9: (a) Stress path response of BCC single crystal subjected to the proportional and non-proportional biaxial strain paths shown for self-hardening conditions. 60

Fig. 3-10: Total dislocation density ρ in the BCC single crystal as a function of slip direction orientation θ for non-proportional paths to a final biaxial state for anisotropic self-hardening conditions. 61

Fig. 3-11: (a) Resulting stress paths for the BCC single crystal response to the non-proportional uniaxial strain paths indicated to a final uniaxial tension state for isotropic latent-hardening conditions, (b) the schematic Tresca yield surface response illustrating the respective stress paths. Note that $\varphi = \tan - 1\upsilon$. 62

Fig. 3-12: Pole figures showing the initial textures used in the simulations (a) R-1: random texture with 216 grains, (b) R-2 random texture with 216 grains (c) FS-1: ferritic steel texture with 216 grains and (d) FS-2: ferritic steel texture with 125 grains. Note that FS-1 and FS-2 are approximately the same texture however with differing number of grains. 65

Fig. 4-13: The oligocrystal used in the simulations (showing 216 grains).The negative 1-, 2- and 3- surfaces are always constrained such that displacements in these directions are zero. Strain paths shown in Fig. 2 are applied to the positive 1- and 2- surfaces. The positive 3-surface is constrained planar such that the average stress on this face is zero. Note that each colored region represents a grain with similar orientation is approximately 25μm. 65

Fig. 3-14: Stress paths and dislocation structures for textures R-1 under non-proportional strain paths to biaxial tension state. (a) stress path diagram for random texture R-1 under isotropic latent-hardening, (b) stress path diagram for random texture R-1 under self-hardening (c) dislocation structure of R-1 at final biaxial state under anisotropic self-hardening, and (d) dislocation structure of R-1 at final biaxial state under isotropic latent-hardening. 71

Fig. 3-15: Stress paths and dislocation structures for textures FS-1 under non-proportional strain paths to biaxial tension state. (a) stress path diagram for ferritic steel texture FS-1 under isotropic latent-hardening, (b) stress path diagram for ferritic steel texture FS-1 under anisotropic self-hardening (c) dislocation structure of FS-1 at final biaxial state under anisotropic self-hardening, (d) dislocation structure of FS-1 at final biaxial state under isotropic latent-hardening. 72

Fig. 3-16: Stress paths and dislocation structures for textures FS-2 under non-proportional strain paths to biaxial tension state. (a) stress path diagram for ferritic steel texture FS-2 under isotropic latent-hardening, (b) stress path diagram for ferritic steel texture FS-2 under anisotropic self-hardening (c) dislocation structure of FS-2 at final biaxial state under anisotropic self-hardening, and (d) dislocation structure of FS-2 at final biaxial state under isotropic latent-hardening. 73

Fig. 3-17: Stress paths and dislocation structures for textures R-1 under non-proportional strain paths to uniaxial tension state. (a) stress path diagram for random texture R-1 under isotropic latent-hardening, (b) stress path diagram for random texture R-1 under anisotropic self-hardening, (c) dislocation structure of R-1 at uniaxial state under anisotropic self-hardening, (d) dislocation structure of R-1 at uniaxial tension state under isotropic latent-hardening.....74

Fig. 4-18: Stress paths and dislocation structures for textures FS-1 under non-proportional strain paths to uniaxial tension state. (a) stress path diagram for ferritic steel texture FS-1 under isotropic latent-hardening, (b) stress path diagram for ferritic steel texture FS-1 under anisotropic self-hardening, (c) dislocation structure for FS-1 at uniaxial state under anisotropic self-hardening, and (d) dislocation structure of FS-1 at final uniaxial tension state under isotropic latent hardening.....75

Fig. 4-1: 3-D models adopted in developing localization criterion (a) Model I with no imperfection (b) Model II with an inherent imperfection. Note that material properties are specified in Table 3-1.....79

Fig. 4-2: Cross-section of a polycrystal with critical grains accumulating plastic strain relative to the polycrystal indicated by the rings. q represents the normalized average plastic strain increment at a particular deformation state (t_n) i.e. $qjtn = dqjtn(dptn) - 1$ where $dqjtn$ is the plastic strain increment in grain j and $dptn$ is the increment of average plastic strain for all grains in the polycrystal. 81

Fig. 4-3: Characteristic response of the normalized plastic strain in a deforming polycrystal. $\Gamma = 1Nci = 1Ncqitn$ is the average normalized incremental plastic strain of the set of critical grains selected numerically from results such as those shown in Fig. 4-2. 83

Fig. 4-4: Sensitivity of the normalized, average incremental plastic strain to the critical grain set size for an initially random polycrystal subjected to plane strain conditions up to arbitrary

strains. $\Gamma = 1Nci = 1Ncqitn$ is the average normalized incremental plastic strain of the set of critical grains selected numerically from results such as those shown in Fig. 4-2. 83

Fig. 4-5: Proportional strain paths followed for the prediction of limit strain based on the polycrystal in Fig. 4-1. 85

Fig. 4- 6: Predicted limit strains under proportional strains (a) with defect in model (b) without imperfection in model. A, B, C, D and E indicate the proportional strain paths illustrated in Fig. 4-5. 85

Fig. 4-7: Description of the measure of non-proportionality showing the measurement of deviation angles from the proportional case. 87

Fig. 4-8: Dislocation distributions for random polycrystal R-1 under self- and isotropic latent-hardening at an identical strain state (a) dislocation distribution at final biaxial state under self-hardening (b) dislocation distribution at final biaxial state under isotropic latent-hardening (c) dislocation distribution at final uniaxial state under self-hardening (d) dislocation distribution at final uniaxial state under isotropic latent-hardening rules (e) dislocation distribution at final uniaxial state under isotropic latent-hardening rules using 24 slip systems i.e. 12 {110}<111> + 12 {112}<111>. Note that $\varepsilon 1 = \varepsilon 2 = 0.25$ for the biaxial cases and $\varepsilon 1 = -0.5\varepsilon 2 = -0.125$ for the uniaxial case. 92

Fig. 4-9: Non-proportional paths indicating onset of localization (a) Isotropic latent-hardening (b) anisotropic self-hardening Note that R-1 indicates the response of an initially random polycrystal texture and FS-1 is an initially textured polycrystal. The pole figures of both textures are shown in Fig. 4-12. 93

Fig. 4-10: Average plastic strains in the model at failure as a function of non-proportionality for varied strain paths to a final biaxial state (a) isotropic latent-hardening (b) self-hardening. Note that R-1 indicates the response of an initially random polycrystal texture and FS-1 is an initially textured polycrystal. The pole figures of both textures are shown in Fig. 4-12. 93

Fig. 4-11: Average plastic strains in the model at failure as a function of non-proportionality for varied strain paths to a final uniaxial state (a) isotropic latent-hardening (b) self-hardening. Note that R-1 indicates the response of an initially random polycrystal texture and FS-1 is an initially textured polycrystal. The pole figures of both textures are shown in Fig. 4-12. 94

Fig. 5-1: Schematic of crystal structures showing (a) cubic with $a = b = c;\ \alpha = \beta = \gamma = 900$, (b) triclinic with $a' \neq b' \neq c';\ \alpha' \neq \beta' \neq \gamma'$ and (c) a cubic crystal undergoing uniaxial elongation showing the undeformed (100) plane spacing, d^0, and then after elastic distortion, d^f. 99

Fig. 5-2: Flow diagram showing the binning process of lattice spacing, d, the further refinement of the binned lattice spacing by frequency of occurrence and calculation of the width of the distribution at half maximum (FWHM). 99

Fig. 5-3: Schematic diagram showing the relationship between the undeformed, deformed and relaxed configurations and the corresponding crystallographic orientations in relation to the reference crystallographic configuration. 103

Fig. 5-4: Schematic diagram indicating regions of homogenous lattice deformation (without plastic strain gradients) in A and C, containing statistically stored dislocations and region B in which the plastic strain gradient requires geometrically necessary dislocation content leading to open Burger's circuit B. 107

Fig. 5-5: Schematic of RVE discretization to calculate lattice spacing due to GNDs in crystals from crystal plasticity simulations. (a) Representative volume element (RVE) shown schematically within the material, (b) a particular grain (i) with given crystallographic orientation within the RVE and (c) for a particular element j within grain i, the open Burger's circuit is calculated on the orthogonal surfaces S_1, S_2 and S_3 with normal n_1, n_2 and n_3 shown. 107

Fig. 5-6: Schematic diagram of a single crystal (a) whose [100], [010] and [001] direction coincide with the XYZ system shown subject to uniaxial straining in the Y-direction, modelled using crystal plasticity with computational finite element mesh shown in (b). An undeformed lattice is shown in (c) with the undeformed lattice spacing indicated for the (100) and (010) planes denoted by $d1000$and $d0100$respectively. The lattice is subject to uniaxiual straining as shown in (di) and the post deformation lattice spacing for the (100) and (010) planes are shown in (dii) denoted by $d100$f and $d010$f respectively. 111

Fig. 5-7: Lattice spacing for the single cubic crystal shown in Fig. 8 (c) and (d) subject to uniaxial Y-direction straining indicating the initial spacing (d^0) and spacing after deformation for (a) the {100} and (b) {110} planes. 112

Fig. 5-8: Stress fields (σxx component) for edge dislocations in a 2-D spatial field. In each configuration, a varying local distribution of edge dislocation exists however, the total density of edge dislocations ρT remains constant. (a) ρTA(b) ρTB and (c) ρTC. 112

Fig. 5-9: Lattice spacing peaks determined from the strain field corresponding to the dislocation distributions shown in Fig. 10 for the (a) (111) (b) (100) and (c) (110) planes respectively, showing independence from the dislocation distribution. 116

Fig. 5-10: (a) GND density distribution in a Ti- tri-crystal determined by Britton, T.B. [65] and (b) that calculated using the technique used in this chapter from knowledge of the corresponding experimentally measured displacements. GND density is shown in $\mathrm{Log}_{10}(\mathrm{m}-2)$.....121

Fig. 5-11: Schematic diagram (a) of a single crystal beam $(10 \times 10 \times 100;\ 20 \times 20 \times 2000 \times 30 \times 300\mu m3)$ subjected to four-point displacement loading leading to (b) the progressive development of a linearly varying (Y-direction) plastic strain and (c) a representative distribution of GND density. 122

Fig. 5-12: Lattice spacing distributions due to (i) elastic distortions (ED), (ii) the development of GNDs (GND) and (iii) the two combined (ED+GND) in the single crystal beam shown in Fig. 5-12a subject to four-point bending for the (a) (111), (b) (110), and (c) (100) planes respectively for the applied (peak) strains shown. 123

Fig. 5-13: Schematic diagram illustrating the lattice spacing response of the (100) plane in a beam subject to four-point bending as a function of frequency. The region of pure bending is illustrated in (a) and the response of the (100) plane is illustrated in (b). 124

Fig. 5-14: Lattice spacing peak width (FWHM) due to elastic distortions (ED), the development of GNDs (GND), and the two combined (ED+GND) in the single crystal beam show in in Fig. 5-12 subject to four-point bending for the (100), (110) and (111) planes respectively for applied (peak) strains up to 5%. 125

Fig. 5-15: Lattice spacing distributions due to the development of GNDs for three single crystal beams of varying sizes, (see Fig. 5-12a). The (a) (100), (b) (110), and (c) (111) planes respectively for a peak strain of 3%. The broken line indicates the ideal peak position of that particular plane in an unstrained crystal. 126

Fig. 5-16: (a) Example 216 grain polycrystal, each grain discretized using 216 elements with crystallographic orientations assigned in order to represent (bi) random and (bii) textured polycrystals. 129

Fig. 5-17: Mesh sensitivity study carried out on the model polycrystal shown in Fig. 5-16 showing (a) the Y direction macroscopic uniaxial stress-strain response for the number of elements per grain shown, and (b) Change in plastic strain at an identical point in the mesh calculated using the non-local approach presented in appendix B for different mesh configurations. 130

Fig. 5-18: Lattice spacing peak widths for the polycrystal shown in Fig. 5-16 subject to uniaxial Y-direction straining for the {100}, {110}and {111} planes for increasing strains for (a) the random textured polycrystal and (b) the textured polycrystal (for which the pole figures are shown in Fig. 5-16). 131

Fig. 6- 1: Schematic of Debye Scherrer rings corresponding to a particular deformation state. (a) shows the set of rings of planes that satisfy the Bragg condition in BCC ferritic steel and (b) shows a schematic of the binning of azimuthal sectors 137

Fig. 6-2: Schematic of the computational approach used to simulate x-ray diffraction using crystal plasticity 138

Fig. 6-3: Systematic study of diffraction by {110} family of planes in single crystal ferritic steel. 144

Fig. 6-4: Initial textures used in the simulations showing [T-1] a nominally random texture, [T-2] a fully random texture, [T-2(Exp)] an experimentally obtained ferritic steel texture and [T-2 (Sim)] a computational polycrystal representation of the texture [T-2 (Exp)]. 145

Fig. 6-5: The range of polycrystal models with differing number of grains (a) $3 \times 3 \times 3$, (b) $5 \times 5 \times 5$ (c) $6 \times 6 \times 6$ and (d) $8 \times 8 \times 8$ grains which are used to calibrate the simulated diffraction responses. Note that the same mesh refinement ($6 \times 6 \times 6$ elements per grain) was adopted per grain in all oligocrystal models and each grain had dimensions of $25 \times 25 \times 25 \mu m3$ 146

Fig. 6-6: The number of reflections (diffracted points) per orientation (rotation from X-direction shown in Fig. 6-3) for the range of oligocrystal models shown in Fig. 6-7. (a) shows 0.01^0 tolerance on Bragg's condition, (b) 1^0 tolerance and (c) unbounded in which all planes contribute to the Debye Scherrer ring 149

Fig. 6-7: Calculated {110} normalized lattice spacing change for nominally random texture (T-1) subjected to 10 percent biaxial straining in the 1- and 2-directions of the polycrystal shown in Fig. 6-7d for differing levels of satisfaction of Bragg's condition (0.01^0, 1^0 and unbounded). The azimuthal sector binning sizes employed are (a) 5^0 azimuthal sector size and (b) 10^0 azimuthal sector binning size 150

Fig. 6-8: Comparison of normalized lattice spacing change for the nominally random texture T-1 and the strictly random texture, T-2 151

Fig. 6-9: Experimental evolution of {110} normalized lattice spacing change for texture T-3 subjected to uniaxial and biaxial straining 151

Fig. 6-10: Calculated {110} normalized lattice spacing change for single crystal with the initial configuration specified in (a) and the normalized lattice spacing change shown in (b). Note that $R3$, $R2$ and $R1$ are crystallographic rotation matrices with respect to the global 3-2- and 1- axis shown in Fig. 6-3 152

Fig. 6-11: Evolution of {110} normalized lattice spacing change for random texture T-2 and experimental texture T-3 (sim) subjected to biaxial straining calculated under isotropic and self-hardening 152

Fig. 6-12: Evolution of {110} normalized lattice spacing change for random texture T-2 and experimental texture T-3 (sim) subjected to uniaxial straining under isotropic and self-hardening 155

Fig. 6-13: Analysis of lattice spacing distribution under uniaxial straining in the initially textured polycrystal showing the normalized (a) lower bound, (b) upper bound and (c)

experimentally measured lattice spacings. The lattice spacing at 90^0 rotation from X corresponding to the loading direction is compared between experiment and simulation in (d) while the unbounded lattice spacings are shown in (e). Finally, the lattice spacing in the unbounded case in the loading direction is compared for self- and isotropic hardening in (f). Note that unless otherwise specified, the calculated lattice spacings are under isotropic hardening.....162

Fig. 6-14: Analysis of lattice spacing distribution underbniaxial straining in the initially textured polycrystal showing the normalized (a) lower bound, (b) upper bound and (c) experimentally measured lattice spacings. The lattice spacing at 90^0 rotation from X corresponding to a loading direction is compared between experiment and simulation in (d) while the unbounded lattice spacings are shown in (e). Finally, the lattice spacing in the unbounded case in a loading direction is compared for self- and isotropic hardening in (f). Note that unless otherwise specified, the calculated lattice spacings are under isotropic hardening.....163

Fig. 6-15: Normalized lattice spacing changes at 10 percent (a) biaxial strain and (b) uniaxial strain.....164

Fig. 6-16: Non-proportional paths adopted to achieve strain state C such that strain path A involves biaxial followed by uniaxial straining and strain path B undergoes uniaxial followed by biaxial deformation 165

Fig. 6-17: Experimentally measure normalized lattice spacing change for the experimental texture subjected to non-proportional straining. (ai) and (aii) represent the deformation map corresponding to strain path A-1 and A-2 shown in Fig. 6-16 and similarly, (bi) and (bii) are the deformation maps that correspond to strain paths B-1 and B-2 respectively. 170

Fig. 6-18: The normalized lattice spacing change for the range of strain paths shown in Fig. 6-16 under isotropic and self-hardening. (a) and (b) show the lattice spacing change distribution under isotropic and self- hardening for strains paths A and B respectively and (c) compares the lattice spacing change distributions for paths A and B at an identical state C detailed in Fig. 6-16 171

Fig. 6-19: Analysis of the calculated lattice spacing distribution under isotropic and self-hardening in comparison to experimental measurements for strain paths A (a) and B (b) illustrated in Fig. 6-16. Note that the upper bound and lower bound represent the ten largest and smallest lattice spacing for each orientation (rotation from X).....172

Nomenclature

$\boldsymbol{F}$- Total deformation gradient

γ- Shear strain

$\boldsymbol{D}^{\mathrm{p}}$- Symmetric part of deformation gradient

$\boldsymbol{L}^{\mathrm{p}}$- Symmetric part of deformation gradient

τ- Resolved shear stress

$\boldsymbol{s}$- Slip direction

$\boldsymbol{n}$- Slip plane

g- Slip strength/Critical resolved shear stress

γ_{sum}- Accumulated shear strain

$\boldsymbol{D}^{*}$- Jaumann stress

$\boldsymbol{I}$- Identity matrix

ρ- Dislocation density

h'- Hardening constant

n –strain rate sensitivity

υ- Poisson ratio

$\boldsymbol{\sigma}$- Stress tensor

q- Normalized plastic strain increment

p- Plastic strain

λ^{*}- Wavelength

d_{hkl}- Lattice spacing on hkl plane

$\boldsymbol{R}$- Rotation matrix

$\boldsymbol{B}$- Burgers vector discontinuity

$\Delta\boldsymbol{A}$- Finite element area

dS- Finite element surface area

$\boldsymbol{d}^{\mathrm{gnd}}$- Burgers tensor due to GNDs

$\boldsymbol{d}^{e}$- Burgers tensor due to elastic strains

$\boldsymbol{F}^{e}$- Deformation tensor due to elastic distortions

$\boldsymbol{F}^{\mathrm{gnd}}$- Deformation tensor due too GNDs

$\boldsymbol{F}^{\mathrm{tot}}$- Total deformation tensor due to elastic distortions and GNDs

$\boldsymbol{\varepsilon}$- Strain tensor

$\in_{\mathrm{lat}}^{\mathrm{j}}$- Normalized lattice spacing change in sector *j* where j=1. 2. 3… n

E- Elastic modulus

$^{\max}\in_{\mathrm{lat}}^{\mathrm{j}}$- Maximum normalized lattice spacing change in sector *j* where j=1, 2, 3 ….n

$^{\min}\in_{\mathrm{lat}}^{\mathrm{j}}$- Maximum normalized lattice spacing change in sector *j* where j=1, 2, 3 ….n

N_{c} - Number of critical grains

N_{g} - Number of grains

Γ- Normalized, averaged incremental plastic strain

$\boldsymbol{t}$- Force

np- Measure of non-proportionality

Acknowledgements

I would like to express my deepest appreciation to my supervisor, Professor Fionn Dunne, who has played the role of an academic dad throughout my doctoral studies. He continually showed support, provided funding and always provided motivational words that spurred me on to tackle engineering problems. In addition, I appreciate the opportunity to travel extensively to present at conferences within Europe and North America.

I would also like to thank members of my doctoral research project, Professors Alan Cocks, Angus Wilkinson and Richard Todd for their advice. Immense gratitude also goes to Dr. David Collins who provided experimental results to validate my computational model and also for the MATLAB codes used in simulating x-rays.

Further, I appreciate the ever helpful nature of the members of the solid mechanics research group at Oxford and Imperial especially Drs. Ben Britton and Bo Lan. Also, I acknowledge the support of colleagues and friends both in Oxford University and Imperial College who provided support I needed to go through this PhD.

I appreciate my siblings Temitope, Bolanle and Abisola who simply the best sisters in the world and brothers, Dotun Asekun and Oluseye Awofisayo for their support. Lastly, I am eternally grateful to my parents, Professors Olayiwola Erinosho and Stella Erinosho whose constant prayers in addition to moral and financial support helped me through my PhD program.

Abstract

There is evidence to show that subjecting steel sheets to non-proportional biaxial strains can result in higher limit strains or conversely, premature failure depending on the strain path followed. It is therefore imperative to understand the concept of non-proportionality of strain, its relationship with texture and industrially important effects such as material localization and consequent failure in forming processes for high strength steels used in auto components.

The role of texture, hardening and non-proportionality of strain was investigated followed by the consequent effects on ductility under a range of non-proportional strain paths. It was seen that most significant increases in ductility were achievable under non-proportional uniaxial straining as opposed to biaxial strain straining. A methodology was developed to evaluate peak broadening due to lattice spacing distributions in polycrystals by accounting for the contribution of elastic strains and geometrically necessary dislocations (GNDs). This study showed that whilst elastic strains were important, peak broadening is typically dominated by the contribution of GNDs.

This methodology to calculate lattice spacing was then adopted to create a link to experimental x-ray diffraction lattice spacing measurements. It was shown that differing lattice spacing distributions were achieved by following differing strain paths to an identical strain state. Further, biaxial pre-strain had more influence on the subsequent deformation history compared to uniaxial pre-strain. Experiments showed that higher ductility is achievable under a uniaxial pre-strain as opposed to a biaxial pre-strain. Hence, the effects of pronounced strain re-distribution seen in the calculated response of the latter compared to the former was attributed to account for the differences in ductility seen.

To my nephews, Demi, Timi, Tosin, Dara and Ayomide

Chapter I

1. Strain path effects in ferritic steel polycrstals

Sheet processing is an important stage in the manufacturing of automobiles. Generally, large biaxial strains are applied to sheet metals in order to achieve the required geometries and this must be performed without the onset of necking. Empirical evidence suggests that subjecting metals to a non-proportional strain path enables higher levels of strain to be achieved. Conversely, premature failure may also occur when a counter-beneficial strain path is employed.

Fig. 1-1 shows a range of strain paths followed during forming processes in the auto industry. Path C is an example of a proportional strain path while non-proportional strain paths such as A and B are also shown as deviations from the proportional case. The goal of this project is to evaluate and understand the benefits of non-proportionality of strain because it is anticipated that optimizing the benefits of non-proportionality can revolutionize material forming processes in the auto industry. Interestingly, it has been observed that forming limits (i.e. how much deformation can be accommodated by a material) depend upon the degree of non-proportionality, sometimes advantageously and other times detrimentally. It is therefore useful to provide a mechanistic understanding for this, on the basis of the differing slip systems activated and changed by virtue of non-proportional straining, which lead to the establishment of differing spatial dislocation density distributions and limit strains.

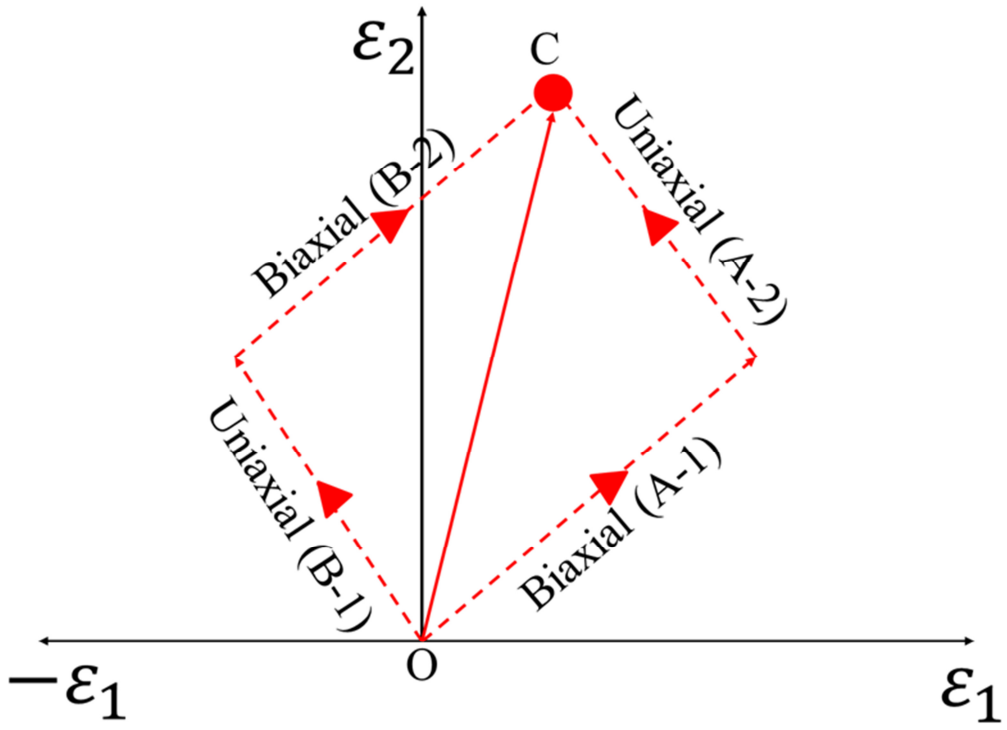


Fig. 1-1: Non-proportional paths adopted to achieve strain state C such that strain path A involves biaxial followed by uniaxial straining and strain path B undergoes uniaxial followed by biaxial deformation

Forming limit diagrams (FLDs) are used to describe strain safe regions in materials prior to neck initiation [1]. They are obtained experimentally by using a hemispherical punch-stretching test on carefully marked flat metal sheets until the onset of necking is observed. Numerous studies based on von Mises plasticity have been used to predict macroscopic behavior of metals and to develop FLDs. Although phenomenological plasticity is limited in modeling crystallographic textures, a number of investigators have used it to model FLDs in conjunction with the Marciniak and Kuczynski (M-K) model [2-4]. The original M-K model was proposed to solve problems related to deep drawing of sheet metals by assuming an initial imperfection exists within the metal which accounts for strain localization [5, 6]. This

model has been widely applied in many investigations and has undergone developments to improve its robustness and applicability [2-4, 7, 8].

Crystal plasticity has been used by many researchers to predict texture evolution, dislocation structures and macro-behavior in metals. Marin et al. [9] investigated the influence of biaxial loading on stress distribution within polycrystals. Ma et al. [10] studied dislocation evolution in body centered cubic (BCC) and face centered cubic (FCC) metals within a crystal plasticity framework and investigated the evolution of geometrically necessary and statistically stored dislocations under proportional biaxial strain paths. A composite approach has also been broadly applied to model dislocation structure evolution in polycrystals [11-15]. Recently, Signorelli et al. [16] used an M-K model to describe limit strains for FCC and BCC metals within a rate-dependent self-consistent plasticity framework. They investigated the effects of initial imperfection, strain-rate sensitivity, hardening coefficients, texture and yield surface shape on forming limits. A comparison was drawn to the crystal plasticity models of Viatkina et al. [17] and Wu et al. [18] and results show improved predictability using a self-consistent model rather than a fully constrained model. Also, Sai et al., [19] have investigated the effects of proportional and non-proportional loading and proposed a unified multi-mechanism model that describes anisotropy effects in aluminum alloys.

The advantages offered by crystal plasticity as described above make it a suitable technique that can be used to study non-proportionality. Using computational crystal plasticity, it is possible to account for microstructurally important effects such as texture and its evolution and how they affect the onset of strain localization under a range of proportional and non-proportional strain paths. Hence, a range of systematic studies to understand the concept of

non-proportionality and its consequences in ferritic steel polycrystals are presented. The structure of the thesis is such that;

Chapter 2 provides a review of the fundamental techniques used in the following chapters.

Chapter 3 contextualizes non-proportionality of strain starting from single crystal behavior to the effects of texture in a polycrystal. This chapter emphasizes the formation of differing dislocation distributions by following non-proportional strain paths under differing forms of hardening.

Next, Chapter 4 provides an extension of this study by understanding non-proportionality effects on predicted ductility. It shows that non-proportional strain paths result in differing levels of ductility which depend on texture as well as the nature of hardening adopted.

Chapter 5 proposes a methodology to differentiate the contribution to lattice deformation resulting from Elastic Strains and Geometrically Necessary Dislocations (GND). This theoretical model attempts to link experimentally measured x-ray diffraction to lattice distortion obtained from crystal plasticity finite element calculations.

Chapter 6 provides a methodology to investigate lattice spacing distribution in polycrystal using simulated x-ray diffraction coupled with crystal plasticity in order to compare with experimentally measured lattice spacing changes.

And finally, conclusions and future work are discussed in Chapter 7.

Chapter II

2. Plasticity fundamentals and literature review

The field of metal plasticity can be traced back to studies on metallic crystals undertaken in the early parts of the nineteenth century [20]. Most notable was the observation of slip deformation bands, which indicated that metals deform along specifically favoured slip planes [20]. Subsequently, a critical value at which slip along these highly favoured slip planes are activated commonly referred to as Schmid's law was proposed. This set off the field of plasticity and in this chapter, a review of the fundamentals are presented. These include slip systems in crystalline materials, Schmid and Non-Schmid behaviour in addition to an introduction to dislocations and material characterization techniques. And finally, the crystal plasticity methodology adopted to investigate non-proportionality of strain is discussed.

2.1. Slip systems in metal crystals

Metallic crystals undergo plastic deformation along particular well defined crystallographic planes described as *slip planes* and whilst doing so, they deform along preferential directions termed as *slip direction*. The combination of a slip plane and its corresponding slip direction which lies normal to that plane constitute a slip system. Slip in materials can be visualized by using powerful microscopes currently available today and Fig. 2-1 shows typical slip bands (indicated with dotted lines) formed on the surface of a Titanium crystal deformed at room temperature. Slip directions have the highest density of atoms along a particular slip plane and this translates to the direction with the shortest Burgers vector between atoms in that

plane [20]. The three common classes of engineering materials can be classified as Face Centered Cubic (FCC), Body Centered Cubic (BCC) and Hexagonal Close Packed (HCP) crystals. The slip planes in FCC crystals are the {111} family of planes and in the <110> direction on each plane giving rise to twelve (12) slip systems shown schematically in Fig. 2-2. Examples of metals that possess this crystal structure include Aluminium, Copper, Gold, Nickel and Silver.

The most notable metal possessing the BCC structure is Iron (Ferritic steel) at room temperature. BCC crystals comprise forty eight (48) slip systems corresponding to the {110}<111>, {112}<111> and {123}<111> slip planes which have 12, 24 and 12 slip directions respectively. The easiest slip systems to be activated in BCC crystals are the {110}<111> systems and are represented schematically in Fig. 2-3. It is worth pointing out that some metals have temperature dependent structures i.e. are face centered at particular temperature and body centered at other temperatures. For example, ferritic steel has a BCC structure at room temperature however, high temperature forms of iron possess the FCC crystal structure. Materials with HCP crystal structure such as Zirconium and Titanium and their range of alloys are applied widely in the aero and nuclear industry. The HCP crystal structure consists of three families of slip planes namely basal, prismatic and pyramidal planes shows in Fig. 2-4. It is important to note the elastic anisotropic associated with HCP crystal such that material properties are direction dependent. Plastically, the basal and prismatic slip planes are the easiest to slip followed by the <a> pyramidal and then the <c+a> pyramidal shown schematically in Fig. 2-4.

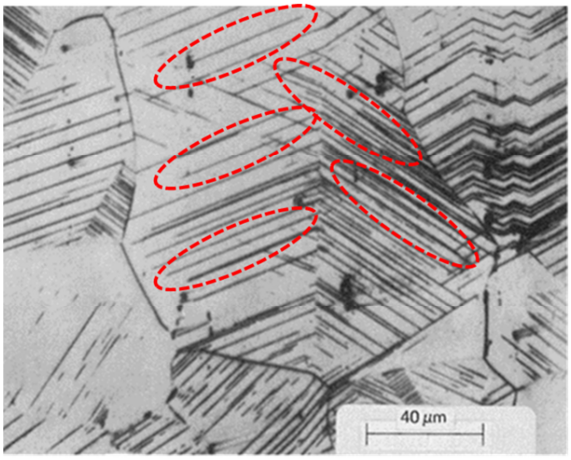


Fig. 2-1: Slip bands on a Titanium crystal deformed at room temperature [21].

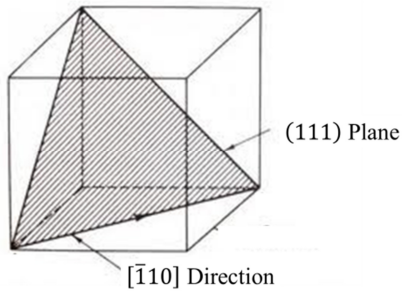


Fig. 2-2: Slip systems in FCC crystals.

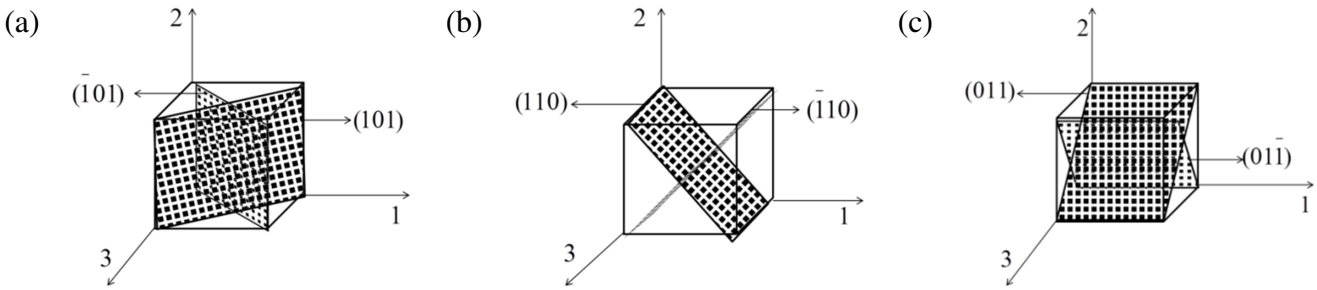


Fig. 2-3: Slip systems in body centered cubic crystals (a) (101) and ($\bar{1}0\bar{1}$) planes (b) (110) and ($\bar{1}$10) planes (c) (011) and ($0\bar{1}$1) planes.

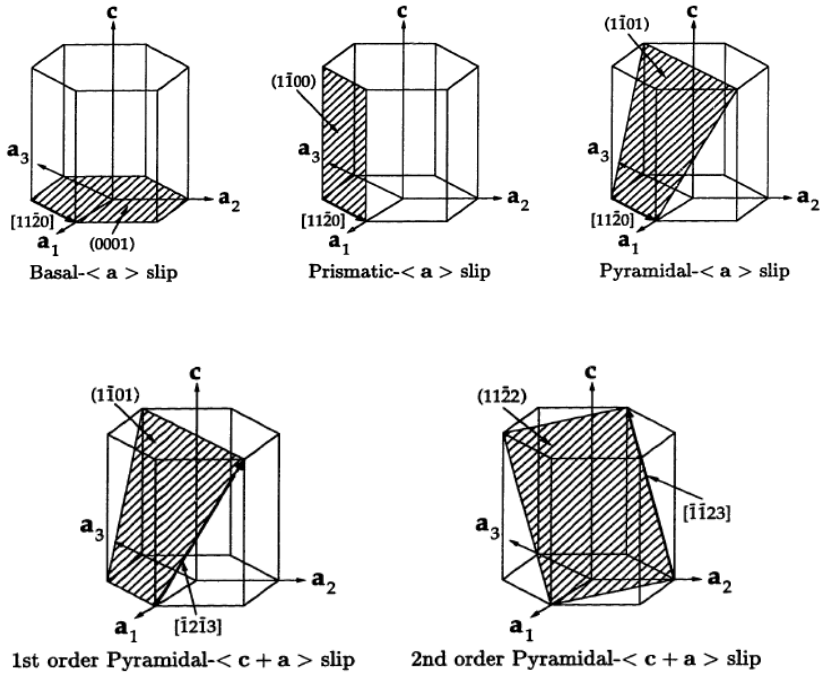


Fig. 2-4: Slip systems in HCP crystals.

2.2. Critical resolved shear stress for slip (Schmid's Law)

Schmid postulated that yielding (slip) on a slip system is initiated when the resolved shear stress on the slip planes corresponding to that system exceeds a critical value [20]. This results in shear along the densest packed direction (slip direction) on that slip plane. Consider Fig. 2-5, the force, $\boldsymbol{t}$ acting on a slip plane shown can be resolved into it its tangential and normal components. $\boldsymbol{t}$ forms an angle $\emptyset$ with the plane and λ, with the normal to that plane. The resolved shear stress can thus be calculated such that

$$\boldsymbol{\tau} = \boldsymbol{t}\cos(\emptyset)\cos(\boldsymbol{\lambda}) \qquad 2\text{- }1$$

where $\cos(\emptyset)\cos(\lambda)$ is referred to as Schmid's factor.

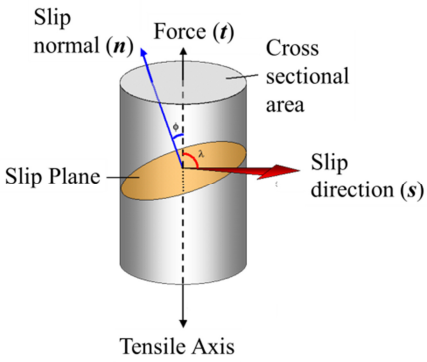


Fig. 2-5: A single crystal containing slip plane with normal ***n***, slip direction ***s***, and loaded in direction ***t***.

Non-Schmid Behaviour

Schmid's law holds true in most cubic crystal systems (FCC OR BCC), however deviations can be observed in BCC crystals as variations in critical resolved shear stress (CRSS) are apparent in the {112}<111> and {123}<111> slip system sets with respect to the {110}<111> types. Intrinsic non-Schmid effects are apparent during shear on the {112} slip planes but are only observed at low temperatures and high strain rates [11]. Extrinsic factors such as temperature and pressure can also account for variations in CRSS observed on the {123} slip plane.

2.3. Introduction to Dislocations

Deviations from ideal structure in a metallic crystal results in the development of internal stress fields of quantifiable magnitude and directions. Dislocations are generated as a result and can be defined as the boundary between the slipped and un-slipped parts of a crystal structure illustrated schematically in Fig. 2-6 [22]. Depending on the scale at which the

dislocations are quantified, they can be termed as either *geometrically necessary* (GN) or *statistically stored* (SS) [22].

Geometrically necessary dislocations (GNDs) are directly related to local non-uniform plastic deformations between grains of a polycrystal and are needed to accommodate lattice misorientations across grain boundaries [22]. However, SSDs are heterogeneous distributions of dislocations that accumulate due to trapping of dislocations during plastic slip and have no geometric consequence [22]. It can be argued that every dislocation is necessary depending on the associated length scale and there have been extensive studies on the physical meaning of GNDs and SSDs. A brief summary is provided next.

Numerous studies have shown the effect of dislocations particularly GNDs on metal deformation [5, 23-27] using various constitutive formulations. Nye [28] developed the widely known Nye tensor generally adopted as a measure of quantifying densities of GNDs. Ashby [23] furthered Nye's dislocation theory in order to distinguish between GNDs and SSDs by adopting a dislocation redundancy characterization method. The Nye tensor represents a sum of individual dislocation line segments under the assumption that the path of the dislocation is irrelevant and that only the initiation and termination point of the dislocation loop are significant.

Many refinements to the Nye dislocation model have been proposed. For example, Arsenlis and Parks [5] investigated the crystallographic aspects of GNDs and SSDs by incorporating length scale effects into classical plasticity (no size effects) formulations. They developed higher order gradient models to predict material behavior at the micron level taking account of size effects. The main difference between the Arsenlis and Parks formulation of the Nye

tensor is in the description of dislocation distributions. In the equivalent Nye formulation, dislocations within a reference volume are considered to be continuously distributed and the tangent line vectors implicitly constant. However, Arsenlis and Parks considered a discrete case in which a material was segmented into volume elements having arbitrary dislocation arrangements.

Overall, the subject of dislocations is still being studied today and the appropriate volume over which the density of dislocation can be measured still remains inconclusive. Hence, the generally accepted norm involves explicitly specifying the volume about which the density of dislocations has been quantified.

2.4. Material Characterization techniques

The computational studies in this thesis have benefitted from many materials characterization techniques. Mechanical tests such as *Nakajima* and *tensile tests* were used to obtain material properties which were then adopted to fit the crystal plasticity simulation parameters whilst characterization tools such as *electron back scattered diffraction* (EBSD) was used to obtain crystallographic orientation (textures) adopted in the simulations. Lattice strain distributions under differing strain paths were obtained using *x-ray diffraction* and this is also discussed.

Forming Limits - Nakajima Testing Machine

Nakajima testing is widely adopted in the auto industry and is used to experimentally determine the strain to failure in metallic samples. Fig. 2-6a is a schematic of a typical Nakajima testing station and Fig. 2.6b illustrates the deformed test samples. Consider Fig. 2-6a, a punch is used to progressively apply load to a test sample (examples shown in Fig. 2-6b) and the two high resolution cameras are used to track the strain state on the carefully

marked metallic sample. The test is completed once fracture occurs and the strain state is calculated based on the applied load to failure. The strain state is then plotted in a 2-D strain space typically referred to as a forming limit curve.

The forming limit for a particular sample is obtained according to the schematic shown in Fig. 2-7. Consider Fig. 2-7a which is a schematic of a carefully marked sample. Now consider path A-A shown, it is possible to track the plastic strain (p) along this path which is shown schematically in Fig. 2-7b. Away from the region of interest is regarded as safe due to homogenous deformation however local to the onset of localization is a significant increase in plastic strain as seen. The region which has significantly high plastic strains is referred to as unstable and unsafe and is undergoing necking. Finally, the marked point that borders the safe and unsafe region is then referred to as the forming limit strain.

It is worth noting that the Nakajima test process described above produces a proportional deformation state and can only be used to generate the forming limit curve for proportion deformation. This is typically a safe processing route however there is evidence to suggest that ductility can be maximized rather than settling for the risk free cases associated with proportional deformation. The concept of non-proportionality is not yet fully understood and the associated risks adequately quantified. Hence, this thesis will provide a further understanding of the role of texture and potential benefits of non-proportionality, thus leading to the birth of new processing possibilities.

(a) (b)

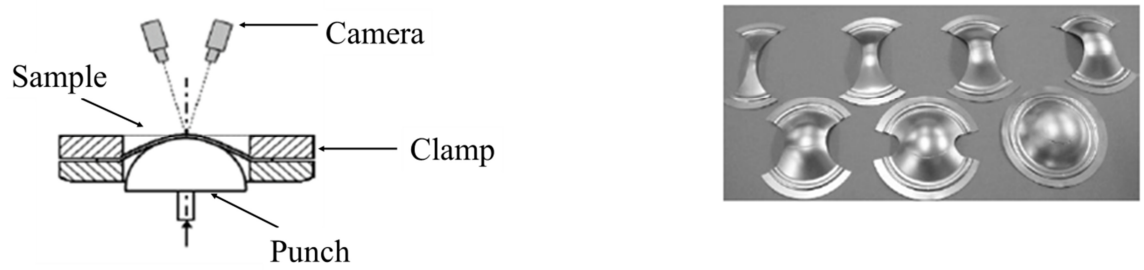


Fig. 2-6: Methodology for mechanical testing of limit strain in metals showing (a) Schematic of Nakajima apparatus and (b) test samples [29].

(a)

(b)

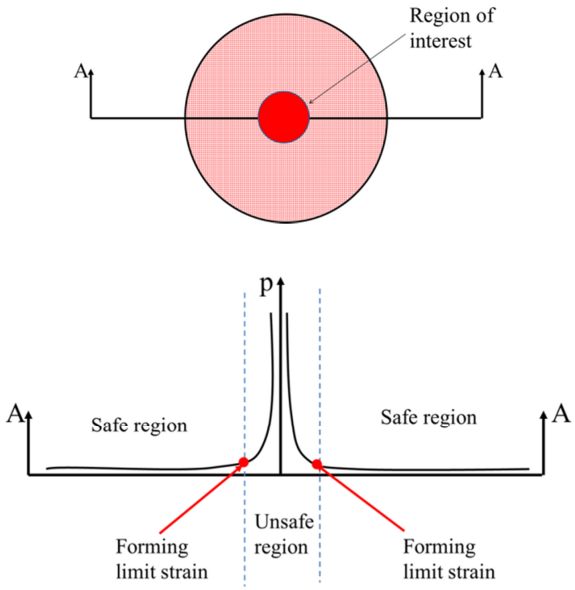


Fig. 2-7: Schematic of the experimental Nakajima test showing an example of a marked sample in (a) and the plastic strain along section A-A denoting the safe and unsafe regions

Numerous studies have attempted to predict forming limits under proportional deformation. The Marciniak and Kuczynski (M-K) model is the most commonly adopted model used to define failure [2-4]. The M-K model was proposed to solve problems related to deep drawing of sheet metals by assuming that an initial imperfection exists within the metal which accounts for strain localization [6]. In this model, the region of imperfection serves as a weaker region whereby instabilities can be measured relative to the outer and stronger region. It is implemented by evaluating the ratio of strain rates in both regions as deformation proceeds. The M-K model is widely used due to its simplicity and flexibility. However, the incorporation of a defect within a material model is not particularly ideal since the location of instability is pre-determined.

Other methods comprising both local and global measurements have been adopted to evaluate the onset of necking in polycrystalline metals. Three additional approaches will be discussed here. One local technique assumes that, at the onset of localization, the thickness strain in the localized region undergoes a significant change and hence, the deformation evolution of a localized region can be described by the strain rate and the strain acceleration. Here, the maximum of strain acceleration is considered to correspond to the onset of necking and the reduction from the maximum value is referred to as the process of localization [30]. Another technique considers localization as the stage at which a continuous decline in the force required to deform a polycrystal is observed [31, 32]. This is a global technique and has been observed to either over-predict or under-predict limit strains and hence, not widely adopted.

Lastly, a bifurcation method has been reported by Volk and Hora [29] to predict limit strains based on the thinning rate measured in the polycrystal. They undertook a 2-D analysis

composed of identifying critical elements prior to fracture and evaluating the average thinning rate of these critical elements along the deformation history. The onset of necking corresponds to the cross-point between the stable region representing homogenous deformation and an unstable section denoted by a significant increase in gradient. A number of other studies on failure prediction have been carried out; see for example [17, 33-36]. However, so far, none has yet addressed the effects of non-proportionality, combined with texture and hardening, on forming limit.

Here, a failure criterion implemented within a crystal plasticity framework is proposed and validated for proportional straining in representative polycrystals. An appropriate measure of non-proportionality is proposed which enables symmetrical but non-proportional strain paths in textured materials to be differentiated, and the polycrystal formulation is then used to investigate the onset of strain localization and its dependence on non-proportionality of strain path.

Lattice Strain Distributions- X-ray Diffraction

The planes that satisfy Bragg's law within a material produce intensities to form a diffraction peak and the presence of many such independent planes result in a diffraction pattern. Bragg's law states that diffraction through crystalline materials occurs preferentially at certain crystallographic planes based on the inter-planar spacing (d_{hkl}) and wavelength (λ^*) of the incident beam as illustrated by Eq. (2-2)

$$\lambda^* = 2d_{hkl}sin\theta. \qquad 2\text{-}2$$

Diffraction techniques based on this formulation vary, but of particular interest to this study is x-ray diffraction which has a wide range of applicability in the understanding of

polycrystalline metals [37]. There are various x-ray diffraction configurations that can be adopted such as *Near field* and *Far field* techniques depending on the distance of the sample to the output detector [38]. The *near field* configuration of diffraction is used to map grain morphologies and orientations within materials while the *far field* method is used to determine strain distributions as well as orientations whilst neglecting morphology. Fig. 2-8 shows a schematic of the x-ray diffraction (Far field) technique. It shows an x-ray beam incident on a sample leading to diffraction from planes that satisfy Bragg's condition. The incident beam interacts with a material volume depending on the bandwidth of the beam and the diffracted beams from planes that satisfy Bragg's condition are then recorded on the 2-D area detector shown. A successfully diffracted beam that hits the detector results in a point (usually called a reflection) and a combination of differing crystallographic orientations within the interaction volume results in the generation of a ring typically referred to as the Debye Scherrer ring. Now, assuming the sample shown in Fig. 2-8 is unstrained, the diffracted beams will only contain information about crystallographic orientations. However, upon straining the sample, changes in the ellipticity of the ring result. Thus, by comparing the deformed ring with a reference ring, it is possible to extract information about the deformation history of the sample under investigation [39-41].

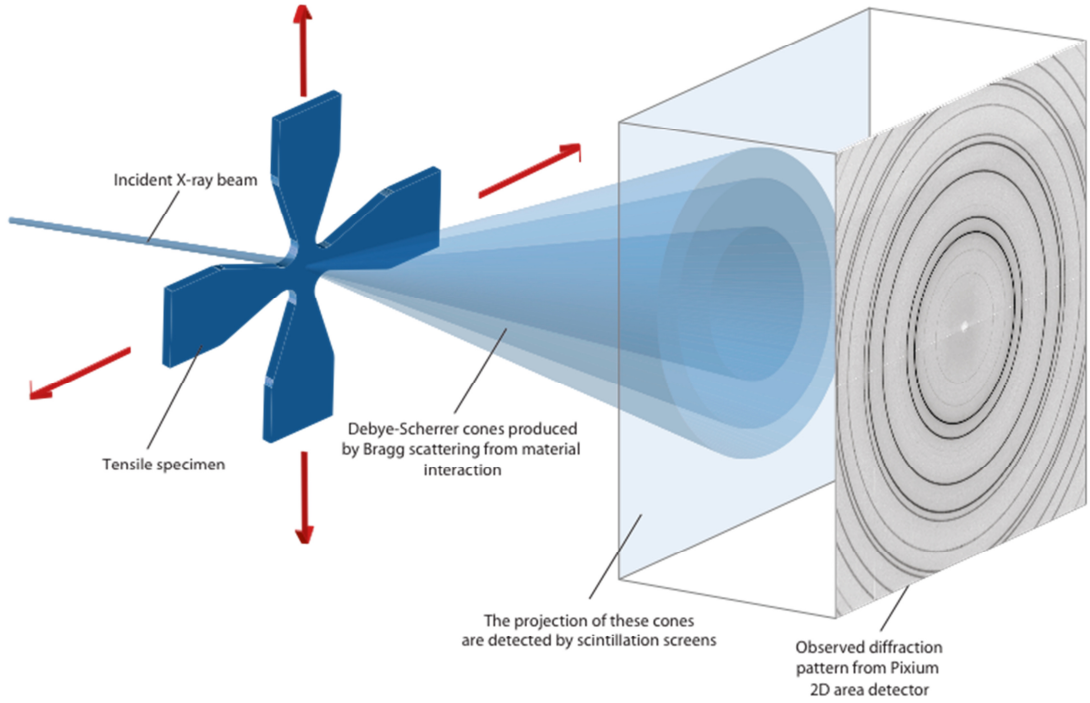


Fig. 2-8: Schematic of the x-ray diffraction process to obtain Debye Scherer rings showing an x-ray beam incident on a deforming sample leading to diffractions which are collected on an area detector

The x-ray diffraction technique is widely adopted and provides useful insight into the lattice strain distribution within the material. However, there are several inherent assumptions associated with the technique. The most obvious is that the beam interaction volume is sufficiently large to provide a statistical representation of the lattice strain within the material. It remains unclear at what point the statistics become less reflective of the true nature since the technique provides an average strain which makes interpretation difficult. In addition, planes that lie parallel to the beam remain invisible which in effect leads to a loss of information. An attempt to solve this limitation involves sample rotation in order to capture adequately differing plane orientations within the interaction volume as reported by Wong et al. [42] leading to increasingly diffused and averaged measurements.

Regardless of the limitations, the x-ray diffraction technique remains a useful method of characterizing orientation dependent strain distributions within metals which is evident from the extensive literature available on the subject. It has been used to study fusion welding [43], residual stresses [44-47], deformation substructure [48] and cracks [49]. For this reason, x-ray diffraction is used to further understand the lattice spacing distributions which are developed for the range of non-proportional considered.

Texture Measurement - Electron Back Scattered Diffraction Microscopy (EBSD)

An important aspect of this study relates to understanding the influence of texture on non-proportionality of strain. EBSD is used to determine crystallographic information (texture) of a material within a conventional *scanning election microscope* (SEM). Consider Fig. 2-9 which shows a schematic of an EBSD setup, it is possible to determine the Euler angles which denote stereographic orientations of individual grains in a 3-D space. Fig. 2-9 shows an experimental EBSD setup in which a focused electron beam is emitted from SEM and incident on a 60°-70° pre-tilted surface of a bulk sample. The sample is tilted in order to maximize the back scatted electron signals. The electrons penetrate into the sample surface and undergo elastic and inelastic interactions. At a high acceleration voltage, the inelastic scattered electron is diffracted if they travel at the Bragg angle to a set of planes and the diffracted rays are collected using a detector (Low light CCD camera). The output from the camera is then processed to form orientation distribution functions and subsequently material texture.

Texture, denoting the presence of a preferred orientation of grains present in a material is important in non-proportional deformation because of its significance in determining the role

of slip system activation and deactivation during deformation. Numerous Von-mises studies on deformation and forming limits such as [39-43] neglect this important aspect, and for this reason, forms an important aspect of this thesis.

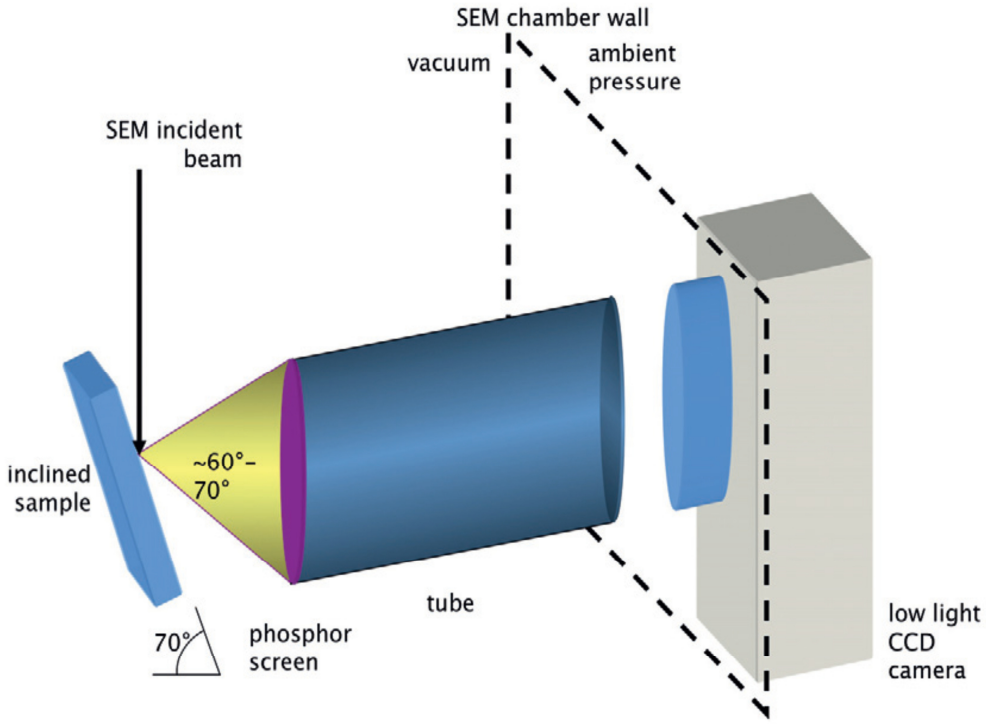


Fig. 2-9: Schematic diagram to show the experimental set up of an EBSD system in a SEM chamber [50].

2.5. Crystal Plasticity Framework

The crux of this project is to understand non-proportional deformation by relating micromechanical processes with macroscopic manifestations using *crystal plasticity*. Engineering materials are subject to strains during use and the magnitude of the strains can be either small or otherwise. Small strains result in elastic responses in which the material reverts to its initial shape while larger strains result in plastic deformation and consequently, permanent lattice distortion. In order to capture material response, a crystal plasticity framework based on the kinematic decomposition of the deformation gradient into elastic ($\boldsymbol{F}^{\mathrm{e}}$) and plastic ($\boldsymbol{F}^{\mathrm{p}}$) tensors laid out by Lee [51] is adopted such that

$$\boldsymbol{F} = \boldsymbol{F}^{\mathrm{e}}\boldsymbol{F}^{\mathrm{p}} \qquad 2\text{- }3$$

and the deformation resulting from crystallographic slip is given in terms of the slip systems directions ($\boldsymbol{s}$) and normal ($\boldsymbol{n}$) together with the slip on any given system

$$\boldsymbol{F}^{\mathrm{p}} = \boldsymbol{I} + \sum \boldsymbol{\gamma}^{\alpha}\,(\boldsymbol{s}^{\alpha} \otimes \boldsymbol{n}^{\alpha}). \qquad 2\text{- }4$$

The plastic part of the velocity gradient may be written

$$\boldsymbol{L}^{\mathrm{p}} = \sum \dot{\gamma}^{\alpha}\,(\boldsymbol{s}^{\boldsymbol{\alpha}} \otimes \boldsymbol{n}^{\boldsymbol{\alpha}}) = \boldsymbol{D}^{\mathrm{p}} + \boldsymbol{\Omega}^{\mathrm{p}} \qquad 2\text{- }5$$

where $\boldsymbol{D}^{\mathrm{p}}$ and $\boldsymbol{\Omega}^{\mathrm{p}}$ are the symmetric and antisymmetric parts of the plastic velocity gradient respectively.

Lattice rotations are determined from the antisymmetric part of the elastic velocity gradient, $\boldsymbol{\Omega}^{\mathrm{e}}$, given by

$$\boldsymbol{\Omega}^{\mathrm{e}} = \mathrm{asym}(\boldsymbol{L}) - \mathrm{asym}((\sum \dot{\gamma}^{\alpha}\,\boldsymbol{s}^{\alpha} \otimes \boldsymbol{n}^{\alpha}) \qquad 2\text{- }6$$

and crystallographic orientations are updated by rotating the slip ($\boldsymbol{s}^{\alpha}$) and normal ($\boldsymbol{n}^{\alpha}$) directions using $\boldsymbol{s}^{\alpha^*} = \boldsymbol{\Omega}^{\mathrm{e}}\boldsymbol{s}^{\alpha}$ and $\boldsymbol{n}^{\alpha^*} = \boldsymbol{n}^{\alpha}\boldsymbol{\Omega}^{\mathrm{e}-1}$ respectively.

Finally, the resolved shear stress on each slip system is calculated from the symmetric rate of stretching of the lattice, $\boldsymbol{D}^*$, Jaumann stress rate, $\widehat{\boldsymbol{\sigma}}^*$ and Cauchy stress $\boldsymbol{\sigma}$ [52] where

$$\dot{\tau}^{\alpha} = \boldsymbol{n}^{*\alpha} \cdot [\widehat{\boldsymbol{\sigma}}^* + \boldsymbol{\sigma}(\boldsymbol{I}:\boldsymbol{D}^*) - \boldsymbol{D}^* \cdot \boldsymbol{\sigma} + \boldsymbol{\sigma} \cdot \boldsymbol{D}^*] \cdot \boldsymbol{s}^{*\alpha} \qquad 2\text{- }7$$

For simplicity, the slip rule employed here is a power law relationship between slip rate and resolved shear stress for a given slip system. Hence the slip rule used is given by

$$\dot{\gamma}^{\alpha} = \dot{\gamma}_0 \left|\frac{\tau^{\alpha}}{g^{\alpha}}\right|^{n} \mathrm{sgn}(\dot{\gamma}) \qquad 2\text{- }8$$

where the slip rate ($\dot{\gamma}^{\alpha}$) evolves on individual slip systems and depends on the reference strain rate, $\dot{\gamma}_0^{\alpha}$, resolved shear stress, τ^{α}, and slip system strength, g^{α}.

The hardening law adopted by McDowell and McGinty [53] and others such as Serenelli et al. [54] and Signorelli et al. [16] has been employed. Consider the slip system strength g, also indicative of the resistance to dislocation motion calculated such that the hardening modulus h_0, and fitting parameter, m are determined for a particular material being investigated. Hence, the strength on each slip system is calculated using

$$\dot{g}^{\alpha} = h_0\left(1 + \frac{h_0\gamma_{\mathrm{sum}}}{\tau_0 m}\right)^{m-1}\dot{\gamma}^{\alpha} \qquad 2\text{- }9$$

where the accumulated slip is given by

$$\gamma_{\mathrm{sum}} = \sum_{\beta=1}^{N_{\mathrm{slip}}}\left(\int_0^t \dot{\gamma}\,dt\right). \qquad 2\text{- }10$$

and dislocation densities on active slip systems are updated according to

$$\rho^{\alpha} = \int_0^t \dot{\rho}^{\alpha} dt. \qquad 2\text{- }11$$

The physical relationship between slip system strength and dislocation density is given by

$$g^{\alpha} = g_0 + \beta\sqrt{\rho^{\alpha}} \qquad 2\text{- }12$$

where the density of dislocations on each slip system is calculated based on an initial value of strength for a particular slip system and updated by

$$\dot{\rho}^{\alpha} = h' \dot{g}^{\alpha} \qquad 2\text{- }13$$

where h' is constant. In passing, it is worth commenting on the nature of the dislocation density evolution adopted here. The relationship between hardening and dislocation density is very simple and results in dislocation accumulation without accounting for annihilation. Whilst this can be adopted for the simple cases presented in this study, it becomes imperative to develop a more advanced strain path dependent dislocation accumulation methodology which accounts for both annihilation and accumulation mechanisms.

Based on the aforementioned hardening mechanisms, two forms of hardening have been considered. One possible form of latent hardening is that all slip systems, active or otherwise, undergo the same level of hardening, referred to here as isotropic latent-hardening. In this case, the slip resistance is assumed to be the same for all slip systems and corresponds to the maximum resistance currently developed, whereby

$$\dot{g}^{\alpha} = h_0\left(1 + \frac{h_0 \gamma_{\text{sum}}}{\tau_0 m}\right)^{m-1} (\dot{\gamma}^{\alpha})_{\max} \qquad 2\text{- }14$$

A second possible form is termed self-hardening. In this case, the slip resistance only develops on active slip systems and dislocation densities are calculated based on these active systems. In this case, for self-hardening,

$$\dot{g}^{\alpha} = h_0\left(1 + \frac{h_0 \gamma_{\text{sum}}}{\tau_0 m}\right)^{m-1} \dot{\gamma}^{\alpha} \,. \qquad 2\text{- }15$$

It is worth pointing out that the exact nature of hardening developed in BCC ferritic steel under investigation is currently unknown. Hence, these ideal forms of hardening are employed to provide a basic understanding of the extremes of mechanisms potentially acting under non-proportional straining. Although, it is anticipated that the nature of hardening in BCC ferritic steel lies between isotropic latent- and anisotropic self- hardening, in the absence of experimental data, the ideal forms provide a basis on which various studies can be undertaken.

The calibration of hardening models for use in crystal plasticity calculations is a longstanding problem due to the variability of behavior exhibited by materials of differing chemical composition. Typically, phenomenological rules such as that presented above are adopted and calibrated, for example, with knowledge of the experimental mechanical response of a material, it is possible to calibrate the parameters of the hardening rule such that the mechanical response obtained from crystal plasticity agrees with experiment. However, this is by no means the most accurate method to account for hardening developed under deformation and for this reason, it is important to develop a methodology to account for the nature of hardening. In the following chapters however, the ideal forms of hardening described in this section are adopted.

Crystal plasticity implementation and code development

The crystal plasticity framework presented in the previous section as implemented within an ABAQUS explicit framework. Details of the implementation is available in the report by

Huang [55] and a further in-depth analysis of the explicit routine can be obtained in [56]. The currently adopted explicit framework is advantageous for many reasons.

First, it is worth pointing out the difference between the implicit and explicit frameworks. In the implicit approach a solution to the set of finite element equations involves iteration until a convergence criterion is satisfied for each increment however, these equations are reformulated as being dynamic in the explicit framework such that they can be solved directly to determine the solution at the end of the increment, without iteration.

The non-proportionality problem investigated in this thesis is a quasi-static process which is typically best suited for an implicit framework. Adopting this framework is reasonable at low deformation levels however, at higher deformation levels, the calculations become problematic. For example, due to non-linearity resulting from localization processes at large deformation levels, the convergence criterion may not be easily satisfied, hence leading to very long simulation times. This problem is eliminated within the explicit framework in which large deformation levels are easily attained albeit by monitoring the dynamics of the system in this quasi-static problem. Solving a quasi-static problem within the explicit framework requires the dampening of inertia effects by using small time-steps. The time-steps can be optimized to improve simulation times [56] however, in order to achieve accurate simulation result, it is imperative to ensure that the inertia forces do not affect the mechanical response. Typically, this is achieved by monitoring the kinetic energy of the system and ensuring that it remains below 5 percent of the total energy. Further, in order to cater for local non-linearity and convergence problems typically associated with the implicit framework, a cut-off time adopted resulting in an approximately accurate response.

Other advantages of the explicit framework within ABAQUS include automatic remeshing and parallelization. Whilst automatic remeshing is useful to cater for non-linearity by refining the mesh locally, it was not used in this thesis. Parallelization was however adopted to improve the speed of calculations by splitting the simulation onto many computer cores. More details on the benefits of ABAQUS explicit and implantation can be obtained from the ABAQUS user manual available online. Note that, the standard crystal plasticity framework used here to obtain material response was inherited however the GND and lattice spacing calculations as well as simulated x-ray measurements were coded in MATLAB.

On this basis, the subsequent chapters individually address different aspects of non-proportionality of strain. A further understanding of the concept and the differing stress states and dislocation structures developed by adopting non-proportional strain paths is presented next.

Chapter III

3. Texture, Hardening and Non-proportionality of Strain in Ferritic Steel Polycrystals

This chapter addresses the effects of non-proportionality, hardening and texture in body centered cubic (BCC) polycrystal aggregates using finite element crystal plasticity. In particular, given the range of self- and latent hardening known to develop within such polycrystals, combined with differing textures, the role of non-proportional strain-paths on those effects is investigated. Single crystal behavior is considered in section 3.1 followed by a systematic study on the effects of texture in section 3.2. Finally, conclusions of this chapter are presented in section 3.3.

3.1. Investigation of non-proportional loading and hardening in single crystal BCC steel

In order to develop an understanding of the combined effects of non-proportionality and hardening in polycrystals, we first consider the simple case of a single crystal in its reference configuration modeled using an ABAQUS C3D8R element subjected to a range of proportional and non-proportional straining paths shown in Fig. 3-1 using the material properties shown in Table 3-1. Note that, 1 and 2-direction strains correspond to the [100] and [010] directions respectively for the crystal in its reference configuration.

The two proportional paths considered are those for biaxial and uniaxial straining, shown as B-1 and U-1 respectively. The non-proportional paths are all variations of these two cases and each comprises two components. An extreme example, shown in Fig. 3-1 for biaxial

straining begins with uniaxial straining in the 2-direction (B-5a) followed by straining in the 1-direction (B-5b) whilst the 2-direction strain is held constant. Note that in all analyses carried out, the positive 3-direction surface is constrained to remain planar, with the average stress in this direction set equal to zero. It is also worth pointing out that some of the strain paths indicated such as U-4a cannot be achieved in reality during sheet processing but are still studied for the purpose of providing a general understanding.

Fig. 3-2 shows the initial macroscopic yield surface in plane stress space for the situation where the in-plane principal stresses are applied in the 1 and 2-directions normal to the faces of the unit cell, which takes the form of a Tresca yield surface. For stress states along AB and DE of Fig. 3-2 slip is activated on the Σ_1-type slip systems shown in Fig. 3-3a, while for stress states along CD and FA it is activated on the Σ_3-type slip systems of Fig. 3-3c, with the Σ_2-type systems of Fig. 3-3b activated by stress states along BC and EF of Fig. 3-2. For isotropic latent hardening the yield surface expands uniformly in stress space, while for self-hardening only the sections of the surface associated with the active slip systems translate.

Consider, initially, the extreme non-proportional biaxial strain path B-5 detailed in Fig. 3-4a with isotropic latent-hardening considered first; the resulting stress path is shown in Fig. 3-4b. To ensure clarity, individual components of stress for loading stages B-5a and B-5b are detailed in Fig. 3-4c and the evolution of the macroscopic yield surface is shown in Fig. 3-4d to describe fully the stress path for the loading regime on the basis of the prescribed hardening rule. The stress path response for strain path B-5 is best visualized by following through key stages in Fig. 3-4a.

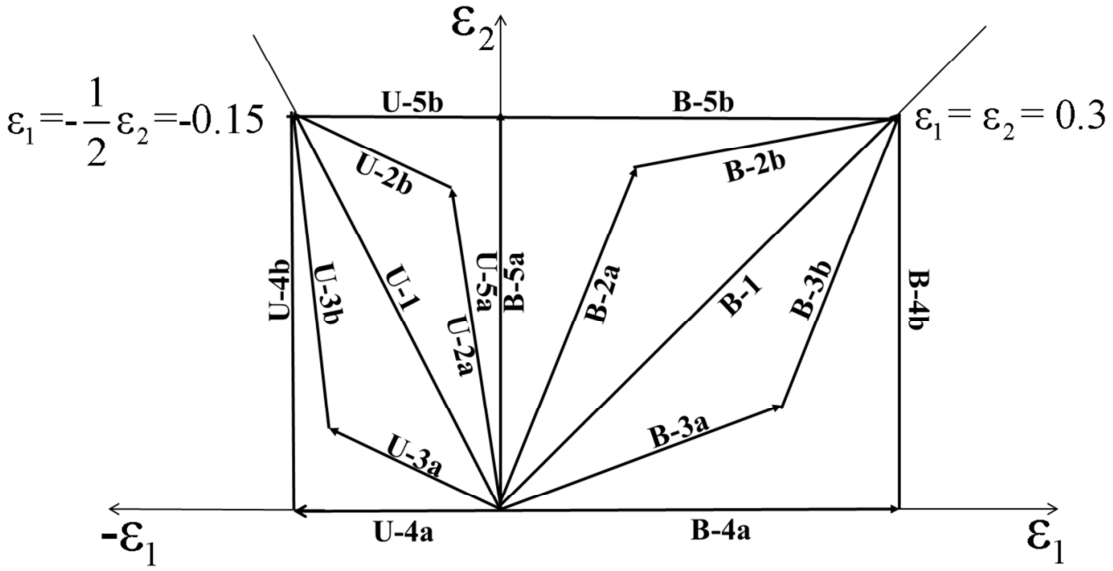


Fig. 3-1: Displacement controlled non-proportional strain paths.

Table 3-1

Material properties of ferritic steel obtained from experiment and used to fit simulation parameters.

Experiment		**Simulation parameters**			
Yield strength	140-300 MPa	ρ_0	10^{10}m^{-2}	E	211GPa
Tensile strength	270-400 MPa	n	800	ν	0.3
Elastic modulus	211GPa	$\dot{\gamma}_0$	1s^{-1}	τ_0	70MPa
		m	0.245	h_0	0.9GPa

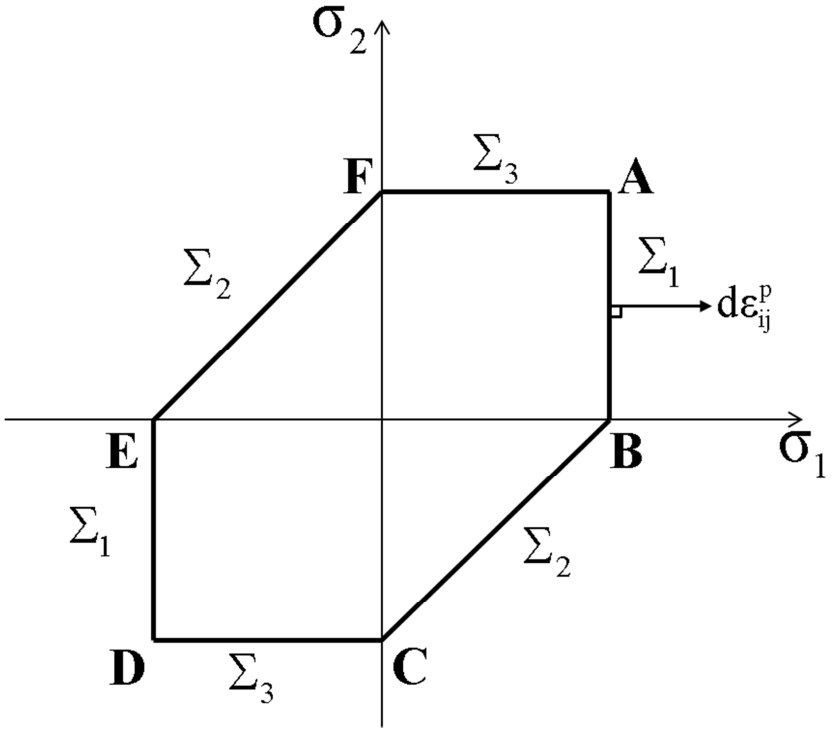


Fig. 3-2: Stress states to activate slip on the slip planes of Fig. 3-3. The labeling corresponds to the families of slip systems indicated in Fig. 3-3 that are activated along different sections of the macroscopic yield surface.

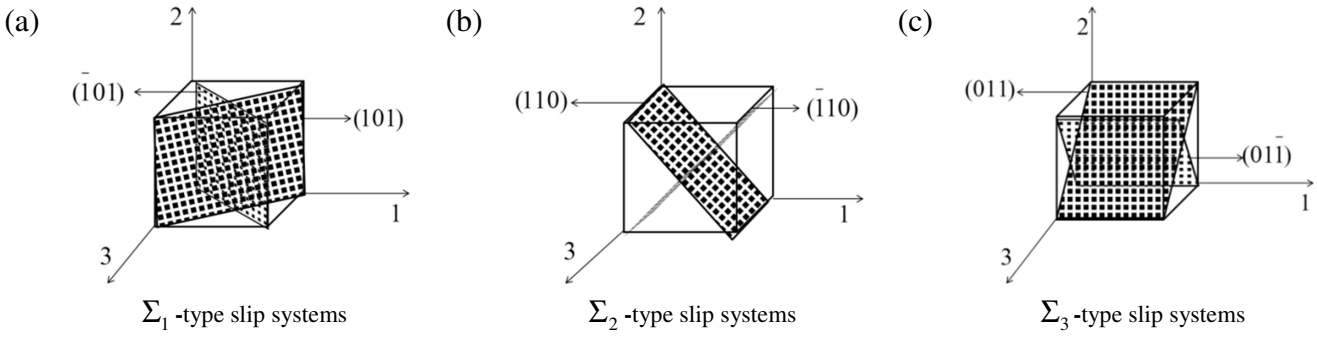


Fig. 3-3: Slip systems in body centered cubic crystals (a) (110) and $(\bar{1}10)$ planes (b) (101) and $(\bar{1}01)$ planes (c) (011) and $(0\bar{1}1)$ planes.

As uniaxial strain is applied in the 2-direction, yielding at A' is followed by plastic deformation towards B. In terms of the individual component of stress, the uniaxial strain in the 2-direction generates the stress response A'-B in Fig. 3-4ci, in addition to a characteristic stress response in the 1-direction observed along A'-B in Fig. 3-4cii. A change in strain path to uniaxial strain in the 1-direction at B causes yielding of newly activated slip systems at B' evident from the elastic jump from B-B' in Fig. 3-4cii before further hardening towards the final biaxial state, C. This process can be more fully illustrated by examining the path followed in stress space combined with the evolution of the macroscopic yield surface. The initial response is elastic and the uniaxial straining path requires that $\sigma_1 = \upsilon\sigma_2$ as shown in Fig. 3-4d. Plastic deformation is initiated at A′ with activation of the Σ_3-type slip systems of Fig. 3-3c, producing a plastic strain increment, $d\varepsilon_2^{\mathrm{p}}$, in the 2-direction. The stress path continues along the path $\sigma_1 = \upsilon\sigma_2$ (due to the requirement that the total strain is uniaxial) to point B as the yield surface expands isotropically. The change of direction of the strain path from B to B′ in Fig 3-4a, results in the stress point moving along the yield surface of Fig. 3-4d from B to B′. Along this section the elastic strain in the 2-direction changes and this is balanced by a positive plastic strain-rate in the 2-direction of the same magnitude. At B′ slip is initiated on the Σ_1-type slip systems of Fig 3-3a, which produce a plastic strain increment, $d\varepsilon_1^{\mathrm{p}}$, in the 1-direction. As the yield surface expands to C on Fig 3-4d the requirement that the elastic component of strain is also uniaxial requires the stress to move along the path

$$\frac{d\sigma_2}{d\sigma_1} = \upsilon. \qquad 3\text{-}1$$

The above analysis has been repeated for a self-hardening rule. The nature of self-hardening is such that now hardening only occurs on active slip systems. The result is an overall reduction of the level of stress compared with isotropic hardening to the B-5 straining path of Fig 3-1. Fig. 3-5 provides a full description of the characteristic response of a BCC steel single crystal to this strain path.

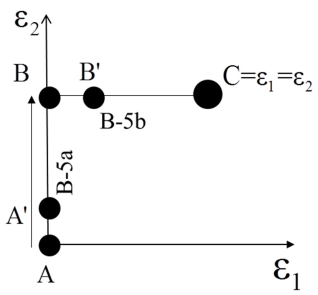
As previously described, uniaxial straining in the 2-direction results in $\sigma_1 = \upsilon\sigma_2$ until point B of Fig. 3-5, yielding initially occurring at A′ on the Σ_3-type slip systems of Fig. 3-3c. As plastic strain accumulates, only the sections of the yield surface associated with slip on these planes expand as shown in Fig. 3-5c. After the direction of straining is changed, these sections continue to expand as the stress moves from B to B′ on Fig. 3-5c. At B′, slip is initiated on the Σ_1-type slip systems of Fig. 3-3a. With continued straining in the 1-direction, the elements of the yield surface associated with these slip systems expand. Plastic flow also continues on the Σ_3-type slip systems to keep the total strain in the 2-direction constant, which results in a small expansion of the elements of the yield surface associated with these slip systems. Therefore, from B to B′ slip occurs on two families of slip systems and the stress remains on a vertex on the yield surface as the body is deformed.

Fig. 3-6 further illustrates the accumulation of dislocations on the slip system types shown in Fig. 3-3 for both cases of self and isotropic latent-hardening under strain path B-5. Consider firstly, the case of self-hardening shown in Fig. 3-7a, strain path B-5a causes the Σ_3-type slip systems to accumulate dislocations, however, the Σ_1-type slip systems only accumulate

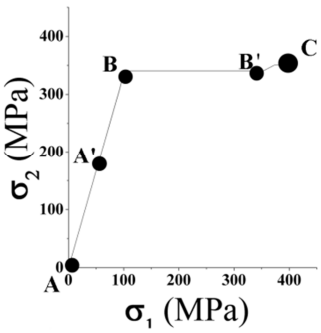
dislocations when the strain path is changed to B-5b. Note that Σ_2-type systems are not active throughout this loading history. Fig. 3-6b shows dislocation accumulation on slip systems under isotropic latent-hardening in which case, slip systems whether active or otherwise undergo the same levels of hardening. Fig. 3-6b shows that higher dislocation levels are expected under this hardening rule and this is hypothesized to affect dislocation structures formed within polycrystals.

In what follows, comparisons of different strain paths under both self- and isotropic latent-hardening are presented for the full range of loading paths shown in Fig. 3-1. This provides a foundation for subsequent investigations of the role of hardening on non-proportionality of strain in BCC polycrystals.

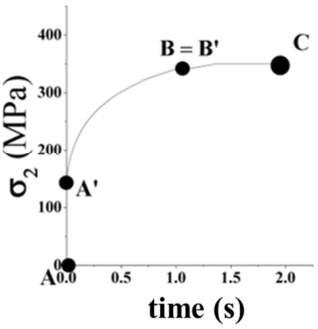
(a)



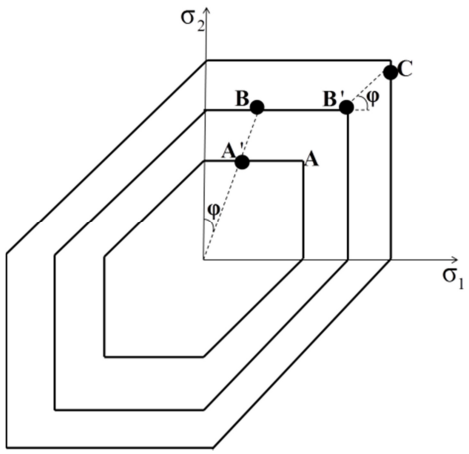
(b)



(ci)



(d)



(cii)

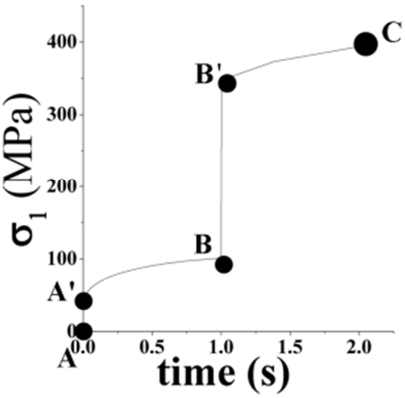


Fig. 3-4: (a) Non-proportional strain path B-5I imposed on the BCC single crystal based on isotropic latent-hardening, (b) stress path response for path B-5I, (c) the corresponding stress component responses in the 1- and 2- directions and (d) the schematic Tresca yield surface representation for path B-5I. Note that $\varphi = \tan^{-1}\upsilon$.

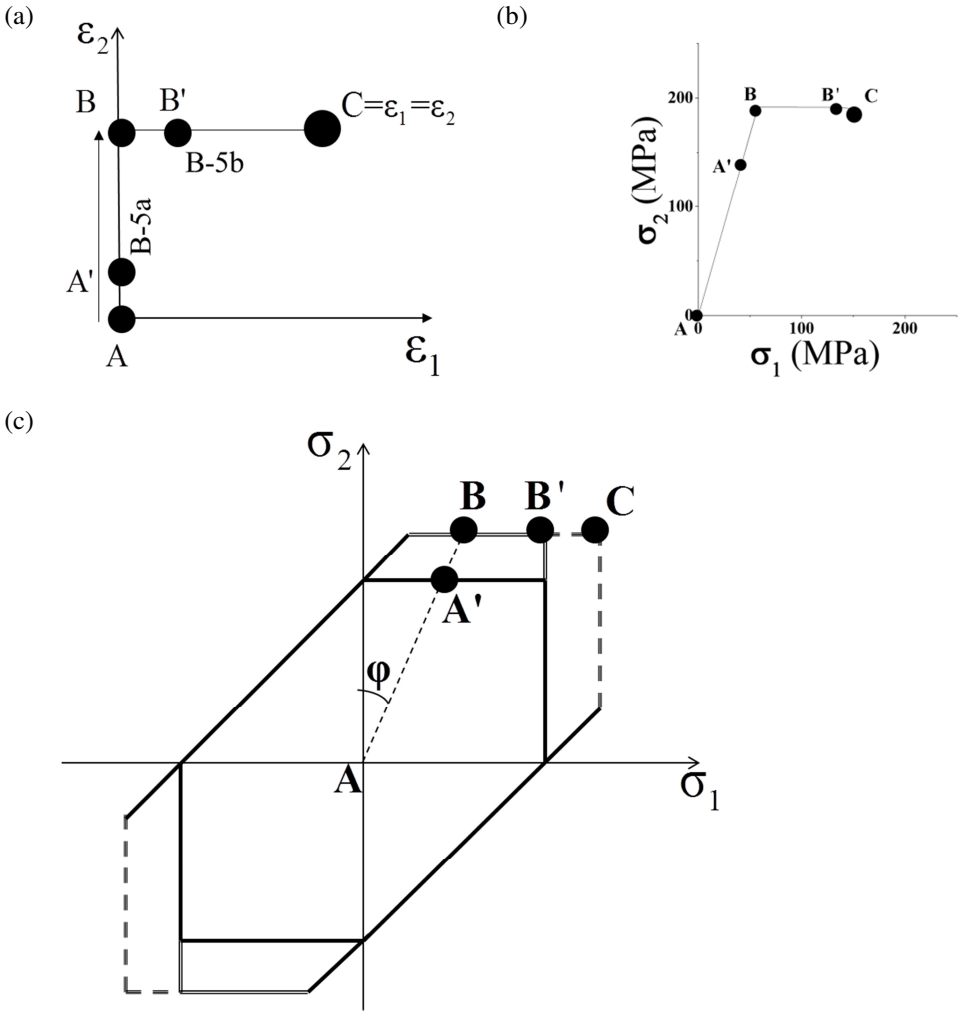
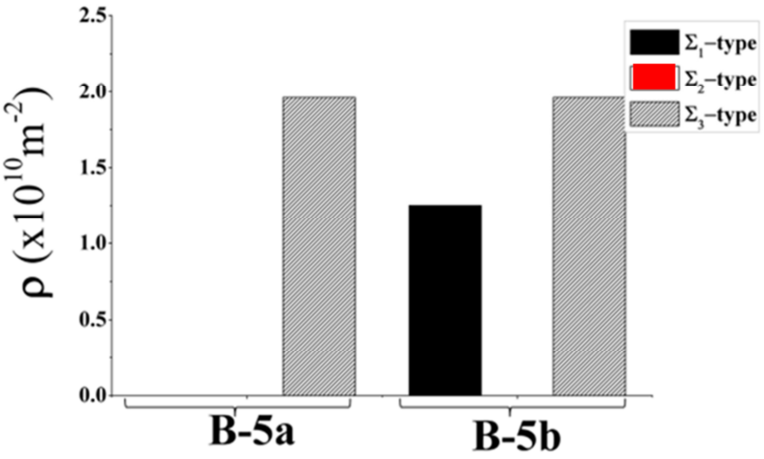


Fig. 3-5: (a) Non-proportional strain path B-5S imposed on the BCC single crystal based on anisotropic self-hardening, (b) stress path for response for path B-5S, (c) the yield surface representation for B-5aS. Note that $\varphi = \tan^{-1} v$.

(a)



(b)

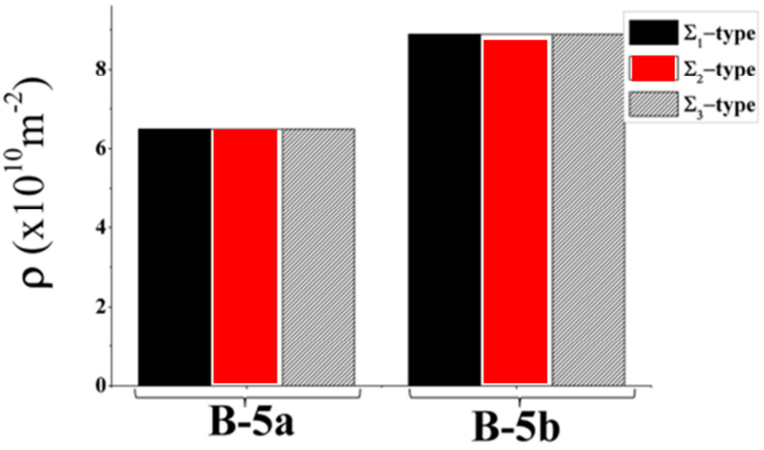


Fig. 3-6: Dislocation accumulation on slip systems during strain path B-5 (see Fig. 3-3 for slip systems types) (a) self-hardening (b) isotropic latent-hardening.

Effects of non-proportional biaxial strains on single crystal BCC steel

It is evident from the results presented in the last sub-section that the material's response under non-proportional loading is best illustrated by examining the paths followed in stress space. We follow this approach here and employ stress path diagrams to examine the response for the full range of straining paths shown in Fig. 3-1. This allows comparisons to be made between proportional and non-proportional strain paths and different descriptions of yield surface behaviour provide a physical interpretation of predicted stress responses. The stress paths experienced by a single crystal of BCC steel for the strain paths of Fig. 3-1 up to a final equi-biaxial state are shown in Fig. 3-7a for isotropic latent-hardening. For path B-1 (proportional loading) $\sigma_1 = \sigma_2$ and in terms of yield surface evolution, loading proportionally corresponds to yielding along B-1 with the stress state remaining at vertex A of the yield surface as it expands as shown in Fig. 3-7b.

Minor deviations from proportionality under isotropic latent-hardening are found to have small effects on the predicted stress response, as evident for B-2 and B-3. Considering B-2 (see Fig. 3-1) as an example for which the stress path and individual stress components are shown in Fig 4-8a and 4-8b respectively, $\dot{\varepsilon}_2 > \dot{\varepsilon}_1$ during B-2a, corresponds to path B-2 in Fig. 3-7b initially until the yield surface is reached. Slip is then initiated on the Σ_3-type slip systems of Fig. 3-3c, producing a plastic strain in the 2-direction. In order to maintain the stain path, elastic strains of comparable magnitude must be generated in the 1-direction. This results in the stress point moving rapidly to the vertex at A', where it remains throughout the remainder of the straining path as slip takes place on the Σ_1 and Σ_2-type slip systems of Fig 3-3. For all loading paths apart from the extreme paths of B-4 and B-5 of Fig 4-1 vertex A of

the yield surface is reached soon after plastic flow is initiated and remains there throughout the straining process as the surface expands isotropically. During the second stage of the straining paths for B-4 and B-5 only a single set of slip systems is activated, i.e. the stress point lies on a face of the yield surface as shown in Fig 4-4d and the stress path is determined by Poisson's ratio υ, see Eq. (3-1).

Following the description of non-proportional strain paths under isotropic latent-hardening up to a final biaxial state, a corresponding study for the self-hardening case is presented in Fig. 3-9. Stress path responses are illustrated in Fig. 3-9. For all the loading paths of Fig. 3-1 the stress state moves to vertex A early in the process and stays at the vertex as the material hardens, even for loading paths B-4 and B-5 as illustrated in Fig. 3-5. Now, as the element is strained, the Σ_1 and Σ_3-type slip systems harden at different rates, with the relative hardening rates determined by the details of the strain path. Thus the evolving shapes of the yield surface and the trajectory of the vertex in stress space is different for different loading paths. This gives rise to a broader range of stress paths and terminal stress states at the end of the straining paths than for isotropic hardening.

Under self-hardening and similarly but to a lesser extent in isotropic latent-hardening, differing stress states are developed for deviations from proportionality. Although this is evident at the single crystal level, it remains to be seen if similar behavior is shown in polycrystals. Analysis of dislocation structures can give insight into the effects of non-proportionality both at the single- and polycrystal level. The dislocation densities on all slip systems as a function of orientation, θ, are shown for single crystals in Fig. 3-10. The orientation parameter θ is obtained by rotating each slip direction into the 1-2 plane and

based on the angle formed between the rotated slip vector and the [100] direction, similar slip systems are binned. The binning process is such that slip vector orientations within a cutoff angle of one degree are classified as being identical and dislocation densities on these similarly oriented slip directions are summed such that

$$\rho_{\theta}^{\mathrm{tot}} = \sum_{\alpha=1}^{N_{\mathrm{slip}}} \rho_{\theta}^{\alpha} \qquad 3\text{- }2$$

where N_{slip} is the number of slip systems (12 for BCC) and $\rho_{\theta}^{\mathrm{tot}}$ is the sum of dislocation densities on each slip system ρ_{θ}^{α} that lie within the cutoff criterion.

There are four unique slip directions in a BCC single crystal in the case where the {110}<111> type slip systems are present, as illustrated in Fig 3-3. Based on slip activity in a single crystal BCC loaded in its reference configuration along the [100] and [010] directions, two unique slip directions exist. Thus, rotating each slip direction in the single crystal onto the 1-2 plane and calculating the angle θ between the rotated vector and the [100] direction results in two peaks seen at θ=36^0 and θ=90^0 in Fig. 3-10. Although a similar geometry in attained at the final state, it is interesting to note that the resulting densities of dislocations vary depending on the strain path. Here, the extreme path to non-proportionality (B-4) shows the highest dislocation density while minor deviations from proportionality (B-2 and B-3) result in lower levels compared to proportional straining (B-1). From an experimental point of view, the difference is relatively small, however, it still remains that some path dependency does exist during non-proportional loading of BCC single crystals.

Non-proportional biaxial straining of single crystal BCC comprising a series of tension and compression strains applied to achieve a uniaxial state have been investigated for both cases of hardening; however, only the isotropic latent-hardening case is presented here as shown in

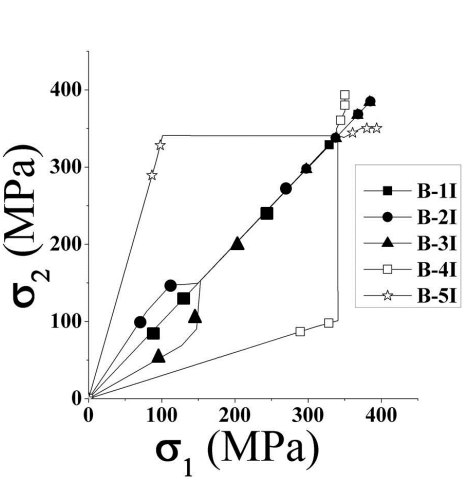
Fig. 3-11. As before, the initial response and where the stress path first meets the yield surface are determined by the elastic response. In order to satisfy the imposed strain pattern the loading point either stays on a planar surface of the yield surface as it expands or moves towards a vertex. Consider the proportional path U-1 (shown in Fig. 3-1) in which the stress path to the yield surface shown in Fig. 3-11b is denoted by U-1, at the point where it reaches the yield surface plastic strain is generated in the 2 direction, with elastic components generated in the 1-direction, which drives the stress towards vertex B as denoted on the yield surface in Fig. 3-11b. The stress point remains on this vertex as the yield surface expands. Deviating from proportionality produces different stress paths as seen in Fig. 3-11. For path U-2 for example, $\dot{\varepsilon}_2 > \dot{\varepsilon}_1$ during U-2a the path A-A′ is followed initially on Fig. 3-11c. The stress point is then driven to the vertex at B where it again stays as the surface expands to C until the direction of the strain path is changed to U-2b. The stress then moves along the yield surface towards the vertex at C′ where it stays throughout the remainder of the strain path. The terminal state produced by this path is significantly different to that generated by path U-1.

Now consider the case of extreme non-proportionality to a uniaxial state such as U-5, tensile strain in the 2-direction (U-5a) is followed by compressive strain in the 1-direction (U-5b). During U-5a,$\sigma_1 = \upsilon\sigma_2$ in the elastic region, hence, the yield surface is reached via U-5 in Fig. 3-11d. This initial step is equivalent to B-5a of Fig. 3-4 and the stress point remains on the planar part of the yield surface as it expands and continues along the path $\sigma_1 = \upsilon\sigma_2$. Applying a compressive strain in the 1-direction results in unloading along the path shown, taking the stress path initially inside the yield surface. This path meets the yield surface at C

and the stress point moves along the yield surface to the vertex at D. The stress point then translates along the planar surface of the yield surface as it expands giving a compressive plastic strain increment in the 1-direction. The stress path is such that Eq. 3-1 is satisfied, thus meeting the requirement that both the plastic and elastic components of strain are zero in the 2-direction.

Whilst understanding the effect of non-proportionality in single crystals is important and provides useful background information for evaluating the response of polycrystals, additional factors such as texture and effects of lattice rotations must be evaluated when considering polycrystals. This is presented in the following section.

(a) (b)



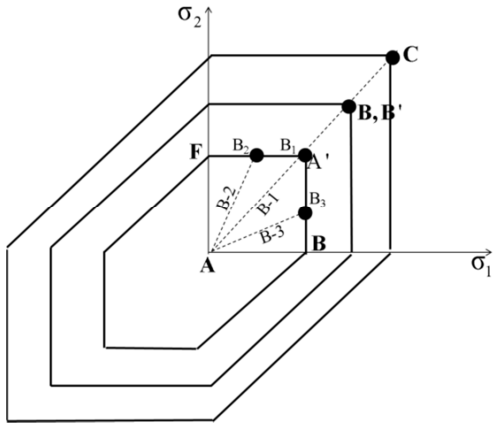
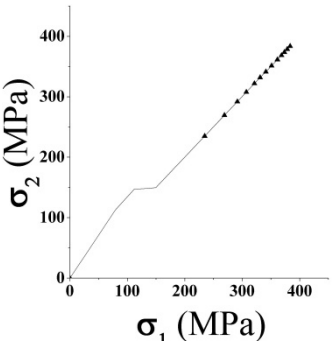
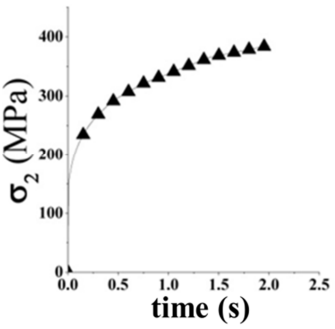


Fig. 3-7: (a) Stress response of the BCC single crystal subjected to the biaxial proportional and non-proportional strain paths shown for isotropic latent-hardening conditions, (b) Tresca yield surface representation showing the stress path followed and the yield surface mode of expansion.

(a) (bi)





(bii)

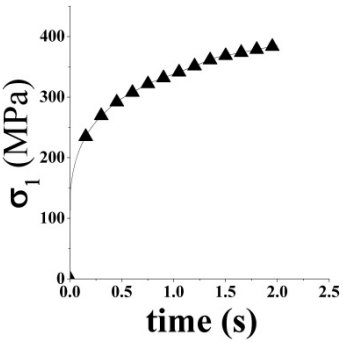


Fig. 3-8: (a) Stress path response of the BCC single crystal subjected to non-proportional strain path B-2I for isotropic latent-hardening conditions and (b) the corresponding components of stress over the loading history in the 1- (bi) and 2- (bii) directions.

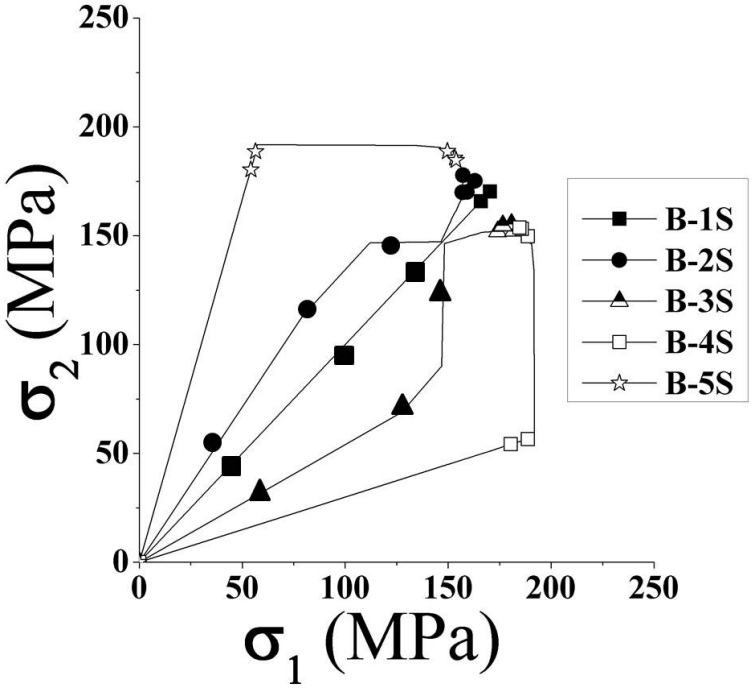


Fig. 3-9: (a) Stress path response of BCC single crystal subjected to the proportional and non-proportional biaxial strain paths shown for self-hardening conditions.

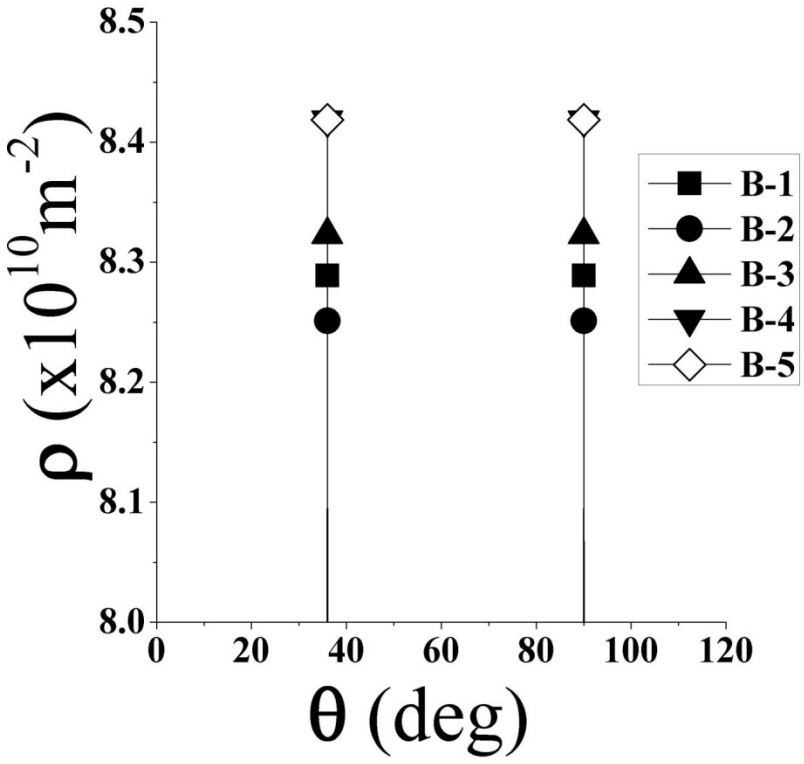


Fig. 3-10: Total dislocation density ρ in the BCC single crystal as a function of slip direction orientation θ for non-proportional paths to a final biaxial state for anisotropic self-hardening conditions.

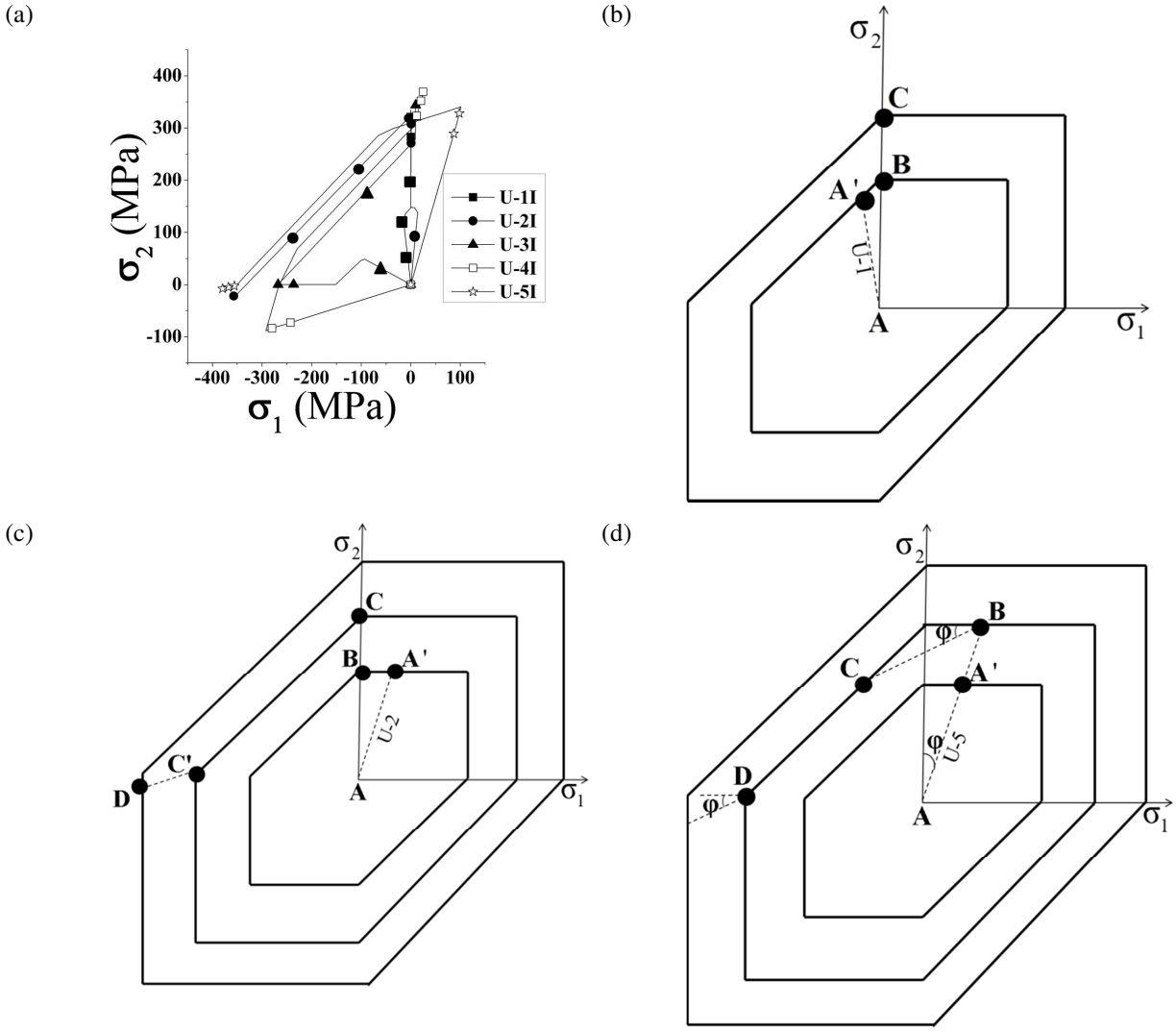


Fig. 3-11: (a) Resulting stress paths for the BCC single crystal response to the non-proportional uniaxial strain paths indicated to a final uniaxial tension state for isotropic latent-hardening conditions, (b) the schematic Tresca yield surface response illustrating the respective stress paths. Note that $\varphi = \tan^{-1}\upsilon$.

3.2. Effects of non-proportional loading on dislocation structures and stress paths in BCC polycrystals

The response of a BCC single crystal to non-proportional strain paths described in the previous section has provided a basis against which non-proportionality effects in BCC polycrystals can be investigated. Since the effects of rotation, stress localization and grain misorientations are not captured by the single crystal, a polycrystalline analysis provides a representation of the material used in automotive applications.

In this study, an oligocrystal with 3×3×3 C3D8R cubic elements per grain is employed in the evaluation of non-proportionality effects in polycrystals. An oligocrystal has been adopted to investigate the response of a representative polycrystal, as well as to evaluate the effects of texture on polycrystal response under non-proportional strain paths. A convergence study was carried out on the oligocrystal adopted in this study presented in Fig. 5-17. It should however be noted that the 3×3×3 elements per grain mesh refinement here was suitable for the current study as well as for efficiency.

Initial Textures, Boundary Conditions and FE Model

To provide a broad understanding of BCC metal behavior, three textures denoted R-1, FS-1 and FS-2 are employed. The pole figures representing these BCC textures can be found in Fig. 3-12. R-1 is an initially random texture illustrated in Fig. 3-12a and has 216 grains. In addition, two ferritic steel textures, FS-1 and FS-2, with 216 and 125 grains respectively are also used here.

The ferritic steel textures, FS-1 and FS-2 were obtained using electron backscatter diffraction (EBSD). The three textures were incorporated into the oligocrystal shown in Fig. 3-13 and implemented within an ABAQUS user material subroutine. In all simulations, the negative 1, 2 and 3 surfaces of the 3-D model are fixed to prevent translation in that direction while strain-controlled displacements are applied to the positive 1- and 2-surfaces based on the strain paths in Fig. 3-1. All surfaces are constrained to remain planar. It is indeed possible to apply other boundary conditions and whilst these may affect the calculated crystal plasticity response slightly, it is hypothesized that the bulk response of the polycrystal will dominate the non-proportionality effects seen and for this reason, the current bulk plasticity planar boundary conditions are adopted.

Similar to the single crystal simulations, non-proportional biaxial strains were applied to achieve a final biaxial- or uniaxial tension state. Two deviations from proportionality were investigated denoted as B-3, B-4 and U-3, U-4 respectively for biaxial and uniaxial loading shown in Fig. 3-1, with each non-proportional path having two loading phases. Note that, in the polycrystal, $\varepsilon_1 = \varepsilon_2 = 0.25$ is attained at the final biaxial state and $\varepsilon_1 = -0.5\varepsilon_2 = -0.125$ for the uniaxial case. Based on these, the effects of non-proportionality, hardening and texture on dislocation structures formed are discussed in addition to evaluating the role of hardening on non-proportionality in polycrystals.

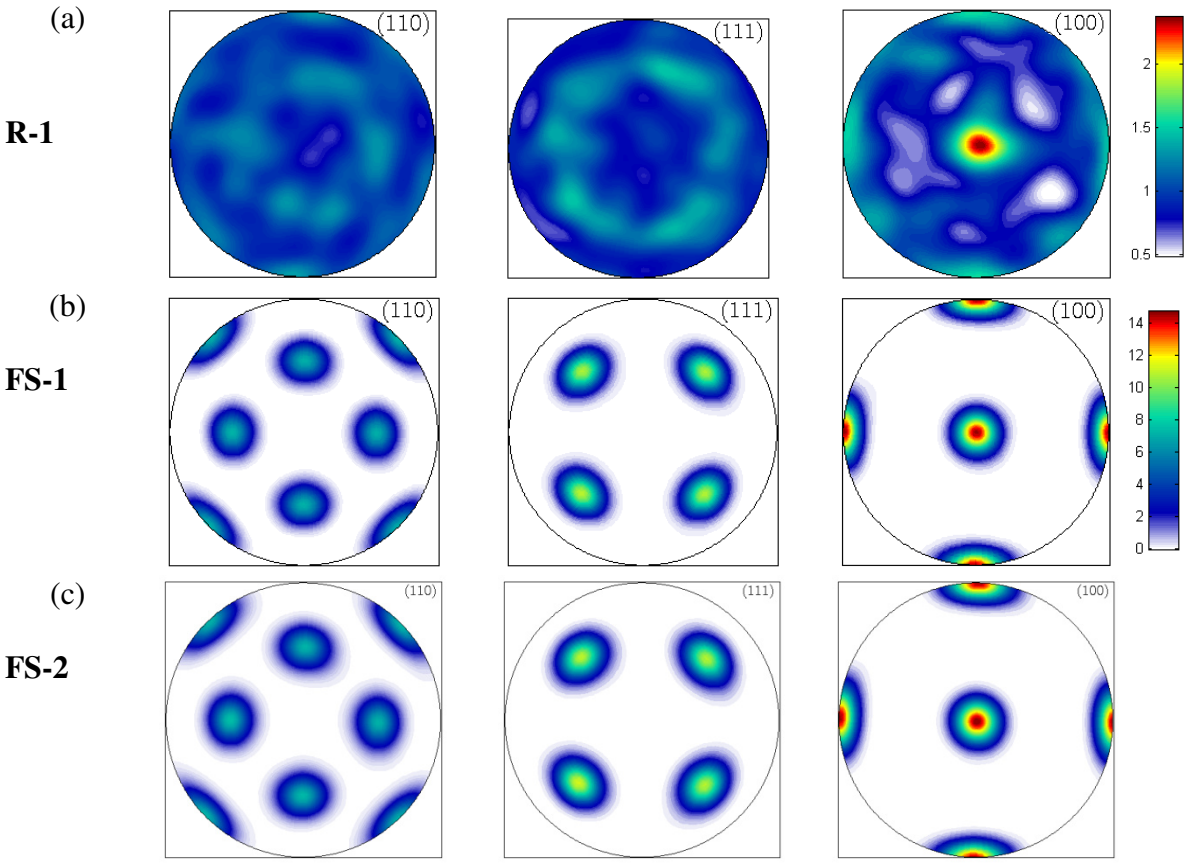


Fig. 3-12: Pole figures showing the initial textures used in the simulations (a) R-1: random texture with 216 grains, (b) R-2 random texture with 216 grains (c) FS-1: ferritic steel texture with 216 grains and (d) FS-2: ferritic steel texture with 125 grains. Note that FS-1 and FS-2 are approximately the same texture however with differing number of grains.

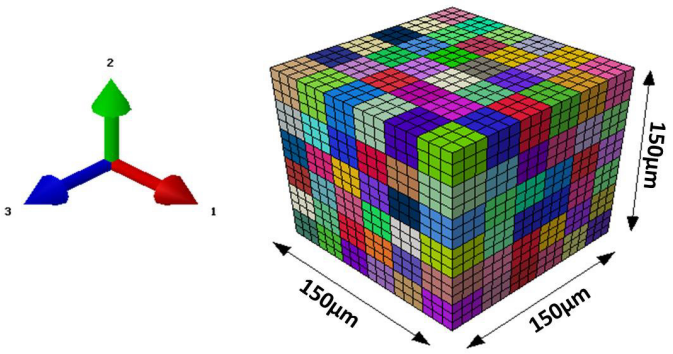


Fig. 4-13: The oligocrystal used in the simulations (showing 216 grains).The negative 1-, 2- and 3- surfaces are always constrained such that displacements in these directions are zero. Strain paths shown in Fig. 2 are applied to the positive 1- and 2- surfaces. The positive 3-surface is constrained planar such that the average stress on this face is zero. Note that each colored region represents a grain with similar orientation is approximately 25μm.

Effects of texture, non-proportional straining and hardening on stress path and dislocation structures in BCC steel polycrystals

The stress responses and associated dislocation structures during loading of the polycrystalline ferritic steels are presented below. The notation used in the figures that follow is such that B-1S indicates the response to strain path B-1 under self-hardening and similarly, B-1I represents the response to strain path B-1 under isotropic-latent hardening. The response of texture R-1 to non-proportional straining up to a final biaxial state shown in Figs. 3-14 is addressed first. Fig. 3-14a gives the averaged stress path response of random texture R-1 under isotropic latent-hardening. Similarly, the averaged stress response of the random polycrystal under self-hardening is shown in Fig. 3-14b and the associated dislocation structures under self-hardening and isotropic latent-hardening are shown in Fig. 3-14c and 3-14d respectively.

Although similar to the single crystal case, albeit considering the effects of texture, proportional strains B-1 result in an equibiaxial stress state ($\sigma_1 \cong \sigma_2$) in the 1 and 2-directions respectively. This holds true because no preferred orientation exists in texture R-1. However, deviating from proportionality (B-3 and B-4) in which $\dot{\varepsilon}_1 \neq \dot{\varepsilon}_2$, the initial texture and more importantly, the form of hardening affects the predicted stress response. Consider the extreme deviation from proportionality, B-4, made up of uniaxially straining in the 1-direction followed by the 2-direction until a biaxial tension state is attained. The first loading phase B-4a corresponding to uniaxially straining in the 1-direction promotes grain alignment in that strain direction as well as hardening on favorably oriented slip systems. Following strain in the 1-direction, uniaxially straining in the 2-direction prompts grain realignment to the new loading direction and consequently, the activation and hardening of slip systems oriented

favorably for slip due to the current strain path. A jump denoted by $P' - Q'$ is observed, however, contrary to a similar jump seen in the stress response of single crystals, this jump results from the stresses developed in the polycrystal due to the realignment of hardened slip systems as well as movement along the average macroscopic yield surface in order to compensate for the imposed macroscopic strains. This is further evident from the difference in gradient between $P - P'$ and $Q' - Q$ such that a steeper gradient occurs from $Q' - Q$ as a result of further hardening on previously hardened slip systems.

The effects of hardening can be further visualized by considering a minor deviation from proportionality, B-3. Here, strain path B-3a in which $\dot{\varepsilon}_1 > \dot{\varepsilon}_2$ results in hardening on slip systems that slip due to the effective 1-direction strain. However, changing the strain ratio during B-3b causes a relatively smaller jump in stress state compared to $Q' - Q$ during B-3 in Fig. 3-14a. This behavior is contrary to the single crystal case in which minor deviations from proportionality do not result in clear differences in stress paths under isotropic latent-hardening.

The stress response of random texture R-1 to non-proportional straining up to a biaxial tension state under self-hardening is shown in Fig. 3-14b. Stress paths similar to those for isotropic latent-hardening presented in Fig. 3-13a are seen. However, considering paths B-1, B-3 and B-4, an overall lower stress response is observed since hardening is only prescribed on active slip systems. Also, similar to isotropic latent-hardening, a varied stress state (although less apparent) is attained at the final biaxial state.

Dislocation structures provide a basis for examining the effects of non-proportionally straining BCC polycrystals. The average dislocation density in the polycrystal is obtained by

using the binning method described earlier for single crystals. Here, slip directions in each grain are rotated into the 1-2 plane and dislocation densities binned based on the angle θ between the rotated slip vector and the [100] direction such that

$$\rho_{\theta}^{\text{avg}} = \frac{\rho_{\theta}^{\text{tot}}}{N_{\boldsymbol{\theta}}} = \sum_{\beta=1}^{N_{\text{grains}}} \sum_{\alpha=1}^{N_{\text{slip}}} \rho_{\theta}^{\alpha}. \qquad 3\text{- }3$$

N_{grains} and N_{slip} represent the number of grains in the oligocrystal and the number of slip directions in each grain respectively and $\rho_{\theta}^{\text{avg}}$ denotes the average density of dislocations of orientation θ based on the summation of binned slip direction densities $\rho_{\theta}^{\text{tot}}$ and the total number of slip directions within each grain that fall within the cutoff criterion of 1 degree, $N_{\boldsymbol{\theta}}$.

Fig. 3-14c illustrates the dislocation structures of initially random texture R-1 subjected to non-proportional strain paths under self-hardening. The dislocation structure can be classified into three regions of importance, namely I, II, and III. These regions indicate the slip response of texture R-1 to non-proportional strain paths for a random texture in which a preferred orientation is initially non-existent. The topology of dislocation structures seen in Fig. 3-14c are similar, notwithstanding the imposed strain path. In effect, the symmetry associated with biaxial loading result in minimal differences in the predicted structures under the applied non-proportional strain paths. Similarly to anisotropic self-hardening, dislocation structures under isotropic latent-hardening are presented in Fig. 3-14d and accordingly, relatively small differences do exist depending on the strain path. The results show a much more uniform distribution of dislocation densities with slip direction angle.

In addition to the initially random texture R-1, two ferritic steel initial textures FS-1 and FS-2 have been subjected to similar non-proportional strain paths up to a final biaxial state as shown in Figs. 3-15 and 3-16 respectively. For each texture, the stress paths under isotropic latent-hardening and anisotropic self-hardening are presented as well as the dislocation structures corresponding to each loading path under both hardening rules. Evident in Figs 3-15a-b and Figs. 3-16a-b, the initial textured nature of FS-1 and FS-2 affects the predicted stress levels and varying final stress states are predicted under both isotropic latent and self-hardening cases respectively. Also, similar dislocation structures are predicted for both ferritic steel textures under self-hardening as clear peaks seen in Fig 3-15c and 3-16c suggesting the presence of preferred orientations in both textures. Furthermore, comparing corresponding regions of interest in the three textures, that is, I, II, and III, relatively sharper peaks are seen in the ferritic steel textures, FS-1 and FS-2, compared to the initially random texture R-1 (Fig. 3-14c). This indicates a preferred orientation exists, however, the results do not show considerable effects of non-proportionality on formed dislocation structures. This is also evident under isotropic latent-hardening in Figs. 3-14d and 3-15d.

Non-proportional strain paths to a uniaxial stress state have also been investigated and presented in Fig. 3-17 and 4-18. In this case, two textures, random texture R-1 and ferritic steel texture FS-1 are evaluated as they adequately describe behavioral trends exhibited by steel polycrystals under non-proportional strain paths with or without an initially preferred orientation. Let us consider the stress path response for random texture R-1 subjected to non-proportional biaxial strains to a uniaxial state shown in Fig. 3-17. Deviating from proportionality such that $\dot{\varepsilon}_1 \neq 0.5\dot{\varepsilon}_2$, results in varying stress states at the final uniaxial state

are seen in Figs. 3-17a and 3-17b for the initially random texture and similarly in Figs. 3-18a and 3-18b for the polycrystal with an initially preferred orientation. In fact, significantly different stress states are predicted by comparing U-1 and U-5 under both hardening modes. Furthermore, the dislocation structures under anisotropic self- and isotropic latent-hardening at the final uniaxial state further illustrate the responses of both textures under varying strain paths. Here, four regions of importance in the structures generated under self-hardening are indicated as I, II, III and IV with random texutre R-1 discussed first for clearer understanding. Consider random texture R-1 subjected to non-proportional strain paths up to a final uniaxial state in which the stress paths are as shown in Fig. 3-17a and Fig. 3-17b for isotropic latent and self-hardening. The differences in stress paths observed at the final state are apparent also in the dislocation structures in Fig. 3-17c and even more pronounced in Fig. 3-17d. A close look at the four regions of interest in Fig. 3-17c illustrates path U-5 as having significantly different and higher densities of dislocation for varying slip system orientation, θ. The differences are clearly more visible under isotropic latent-hardening in Fig. 3-17d. In comparison to the dislocation structures of ferritic steel texture FS-1 shown in Figs. 3-18c - d, relatively sharper peaks are observed in the dislocation structures under both self- and latent hardening; however, the trends in non-proportionality effects are similar.

R-1

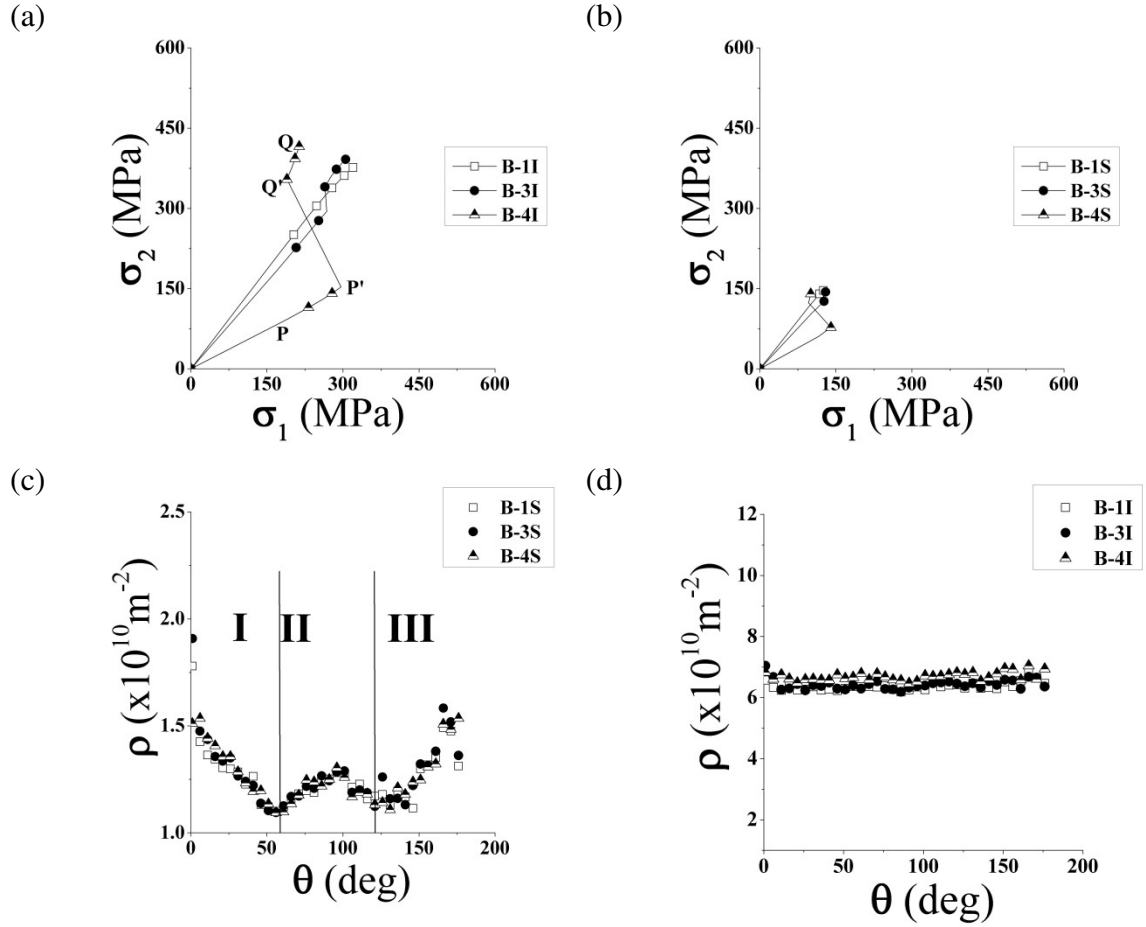


Fig. 3-14: Stress paths and dislocation structures for textures R-1 under non-proportional strain paths to biaxial tension state. (a) stress path diagram for random texture R-1 under isotropic latent-hardening, (b) stress path diagram for random texture R-1 under self-hardening (c) dislocation structure of R-1 at final biaxial state under anisotropic self-hardening, and (d) dislocation structure of R-1 at final biaxial state under isotropic latent-hardening.

FS-1

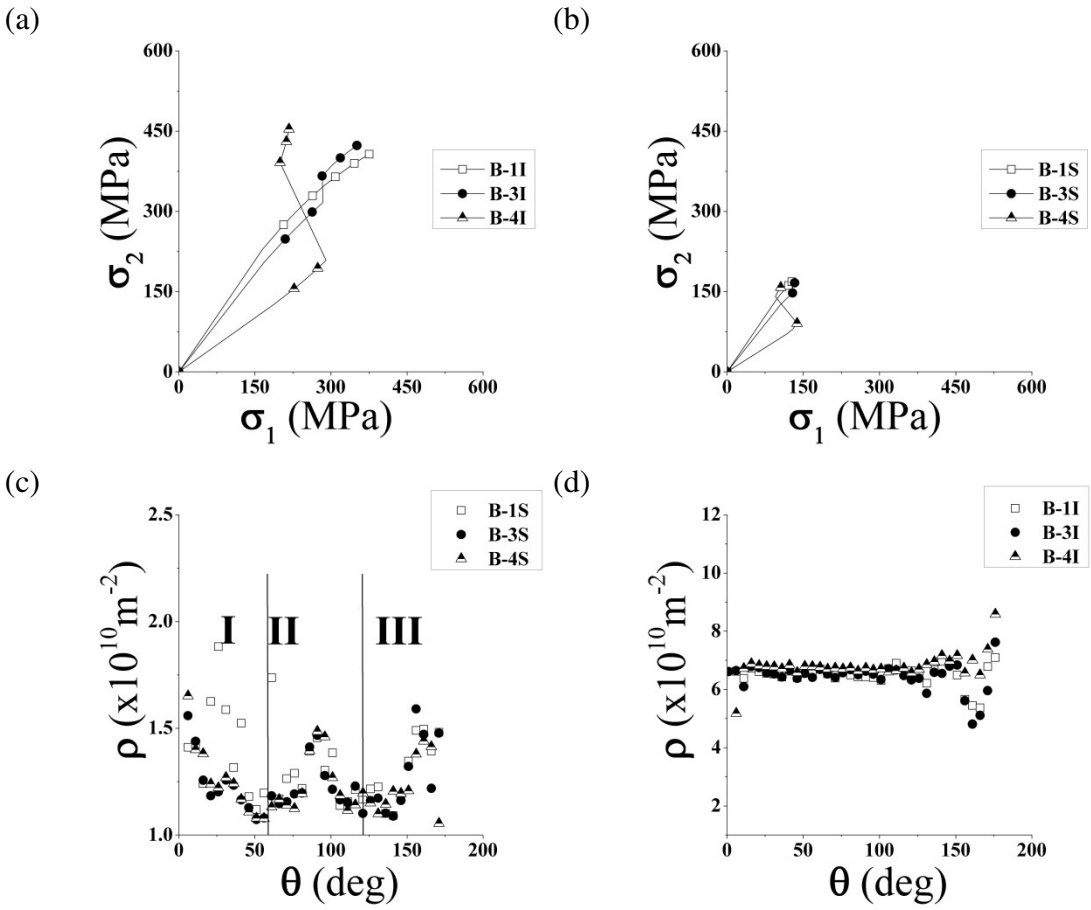


Fig. 3-15: Stress paths and dislocation structures for textures FS-1 under non-proportional strain paths to biaxial tension state. (a) stress path diagram for ferritic steel texture FS-1 under isotropic latent-hardening, (b) stress path diagram for ferritic steel texture FS-1 under anisotropic self-hardening (c) dislocation structure of FS-1 at final biaxial state under anisotropic self-hardening, (d) dislocation structure of FS-1 at final biaxial state under isotropic latent-hardening.

FS-2

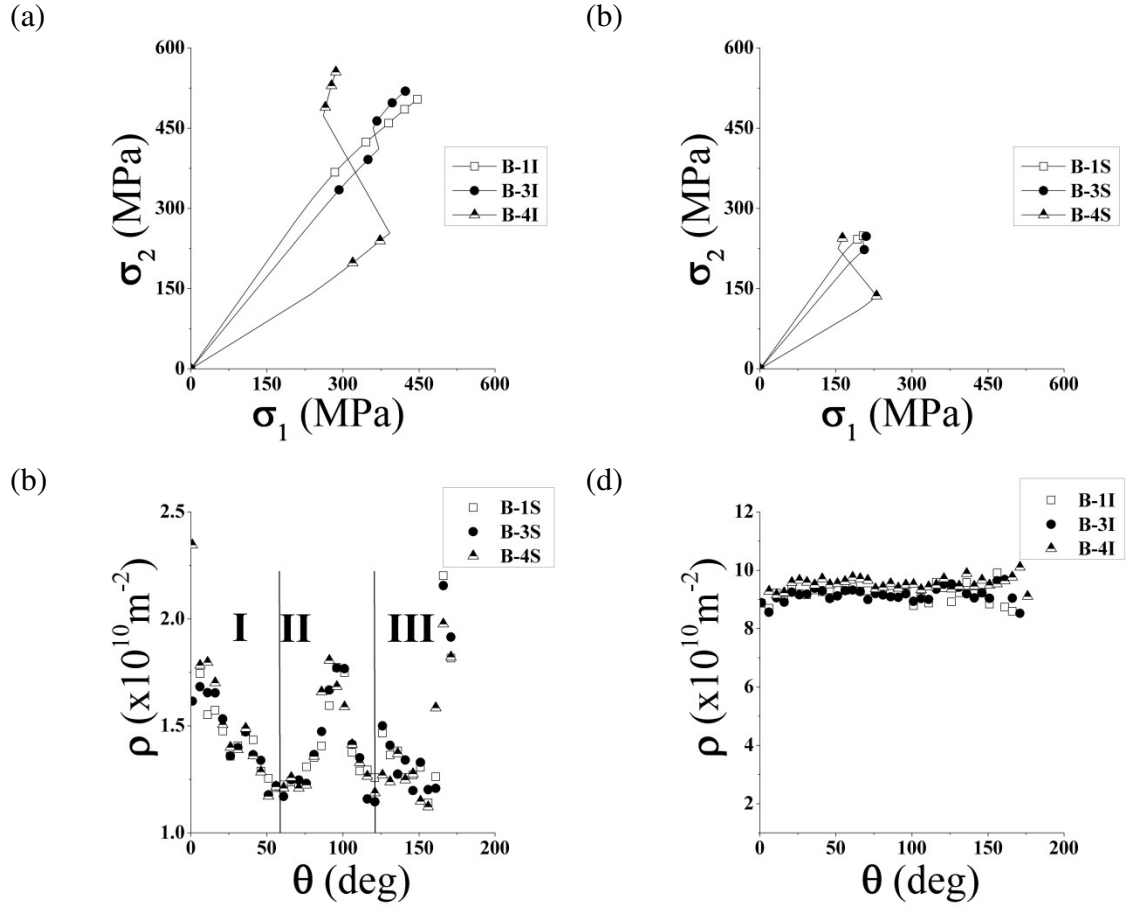


Fig. 3-16: Stress paths and dislocation structures for textures FS-2 under non-proportional strain paths to biaxial tension state. (a) stress path diagram for ferritic steel texture FS-2 under isotropic latent-hardening, (b) stress path diagram for ferritic steel texture FS-2 under anisotropic self-hardening (c) dislocation structure of FS-2 at final biaxial state under anisotropic self-hardening, and (d) dislocation structure of FS-2 at final biaxial state under isotropic latent-hardening.

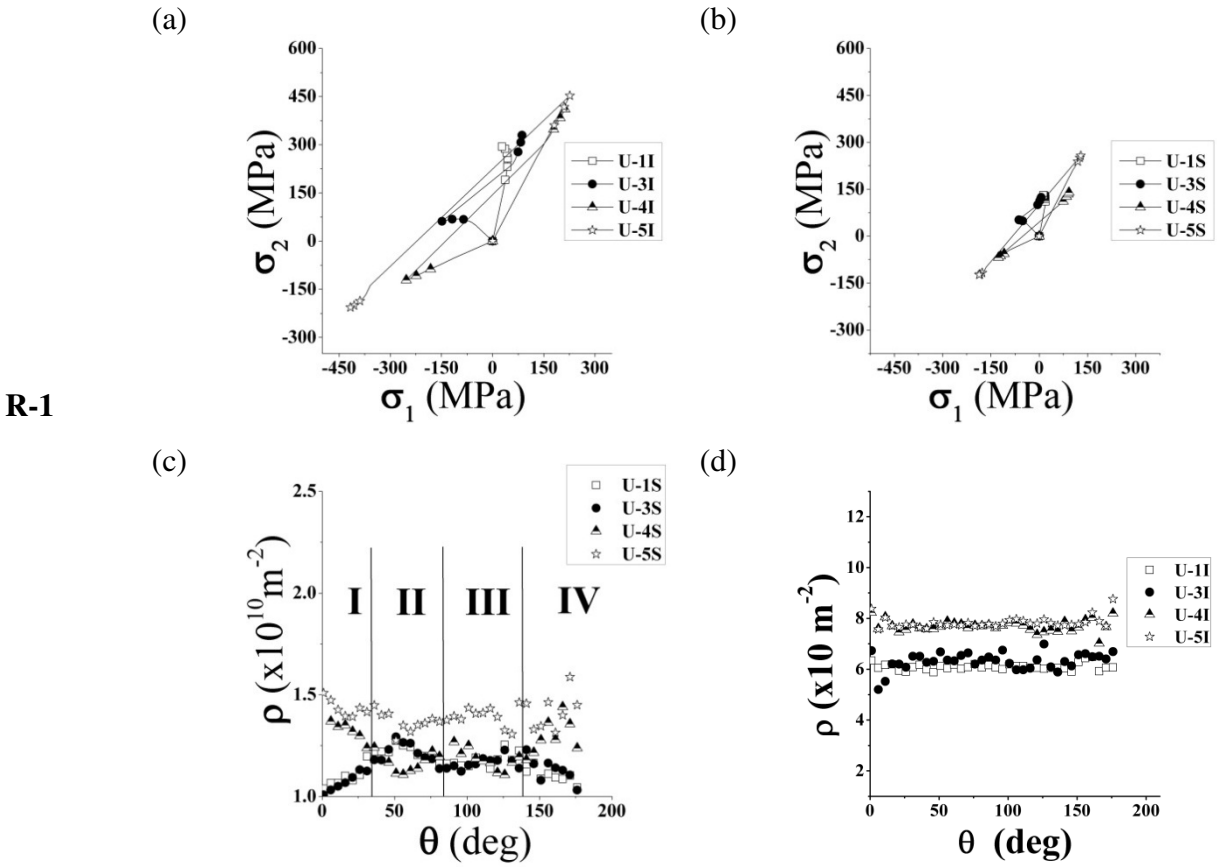


Fig. 3-17: Stress paths and dislocation structures for textures R-1 under non-proportional strain paths to uniaxial tension state. (a) stress path diagram for random texture R-1 under isotropic latent-hardening, (b) stress path diagram for random texture R-1 under anisotropic self-hardening, (c) dislocation structure of R-1 at uniaxial state under anisotropic self-hardening, (d) dislocation structure of R-1 at uniaxial tension state under isotropic latent-hardening.

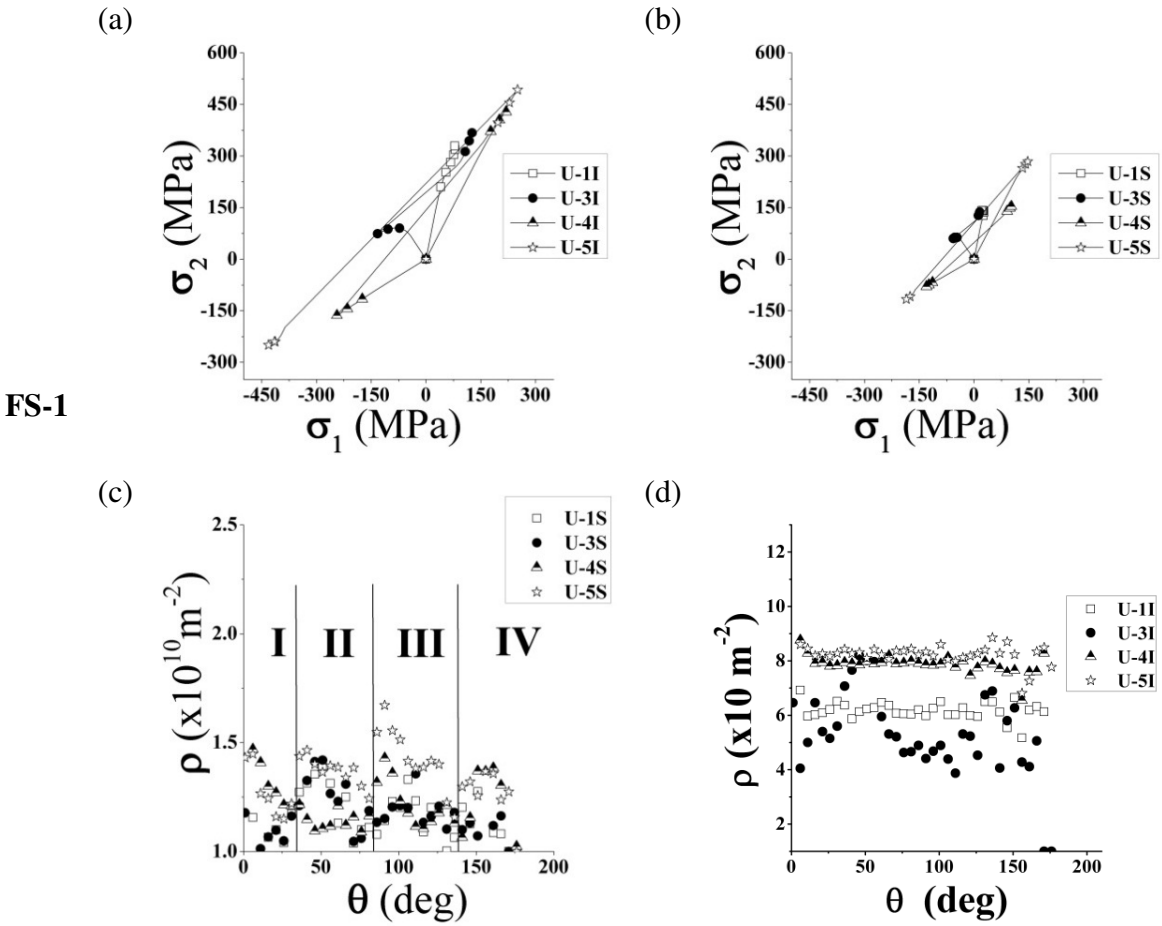


Fig. 4-18: Stress paths and dislocation structures for textures FS-1 under non-proportional strain paths to uniaxial tension state. (a) stress path diagram for ferritic steel texture FS-1 under isotropic latent-hardening, (b) stress path diagram for ferritic steel texture FS-1 under anisotropic self-hardening, (c) dislocation structure for FS-1 at uniaxial state under anisotropic self-hardening, and (d) dislocation structure of FS-1 at final uniaxial tension state under isotropic latent hardening.

3.3. Conclusions

The effects of straining BCC steel single- and polycrystals under non-proportional paths have been investigated within a crystal plasticity finite element framework incorporating a hardening law to impose isotropic latent hardening and (anisotropic) self-hardening respectively. Systematic studies have also been carried out for polycrystal aggregates in order to investigate the effects of initial texture in combination with non-proportionality.

The effect of the differing forms of hardening is significantly more apparent for single-crystal behaviour than that for the polycrystal response. The nature of the hardening has a significant effect at the single-crystal level on the manifestation of non-proportionality, but also affects the resulting behaviour in polycrystals, where the effects of non-proportionality are seen to be larger in the case of isotropic latent hardening than for anisotropic self-hardening. Increasing the degree of non-proportionality is seen to produce greater changes in the final stress state.

Dislocation densities have been calculated on all the independent slip systems, and the roles of hardening and non-proportionality in textured polycrystals have been investigated. Under self-hardening, quite clearly defined dislocation structures are established, which are largely independent of initial texture. However, the level of non-proportionality shows moderate effects on the structure developed. The dislocation structures formed under isotropic latent-hardening are less pronounced since the dislocation densities are more uniform in all orientations resulting from the isotropic nature of the hardening, but the results show clearly the effects of non-proportionality as very strong differences in dislocation structures are seen especially at a final uniaxial tension state.

The initial polycrystal texture is found to have limited effect on the observed macro-scale stress response under non-proportional straining, but does have a much more significant effect on the dislocation structures developed.

Non-proportionality, texture and the nature of the hardening have been shown to be important in determining the final material stress state and dislocation structures developed. It is therefore reasonable to hypothesize that they similarly play a key role in localization at large strain, and hence on likely forming limits. The establishment of forming limits and the corresponding diagrams (FLDs) should therefore be developed in full cognizance of the key role played by non-proportionality.

Chapter IV

4. Coupled effects of texture, hardening and non-proportionality of strain on ductility in ferritic steel polycrystals

This chapter addresses the effects of texture, hardening and non-proportionality on predicted forming limit in body centered cubic (BCC) polycrystal aggregates using finite element crystal plasticity. A failure criterion is used to investigate the onset of strain localization in a range of ferritic steel textures under self- and isotropic latent-hardening rules and a measure of non-proportionality is proposed to represent ductility achieved resulting from the non-proportional strain paths adopted.

4.1. 3-D model development, localization criterion and measure of non-proportionality

This section outlines a description of the models adopted in this study. Further, the localization criterion calibrated using an initially random textured polycrystal and on the basis of isotropic latent hardening is presented. Finally, a measure of non-proportionality, which relates the non-proportional levels to average plastic strain developed within the polycrstal, is discussed.

3-D model development

In order to provide insight into the proposed localization criterion, two representative oligocrystal models with an initially random texture have been examined, shown schematically in Fig. 4-1. Model I is a regular polycrystal containing 216 grains with each grain consisting of 3×3×3 C3D8R elements. Model II is similarly a polycrystal but containing

a central imperfection in which all grains in the region of the imperfection are in the reference crystallographic configuration. That is, the local [100] orientations of the grains coincide with the corresponding global directions in the polycrystal. The purpose of incorporating an imperfection region is to mimic the M-K model, and to carry out comparisons with the regular polycrystal (which, of course, in itself already contains many 'imperfections' resulting from the heterogeneous grain crystallographic orientations). With reference to Fig. 4-1a, simulations have been carried out such that displacements are applied to the in-plane (positive x- and y-) surfaces, and the negative x- and y- surfaces are constrained to remain planar. The positive z- surface is left unconstrained in all cases.

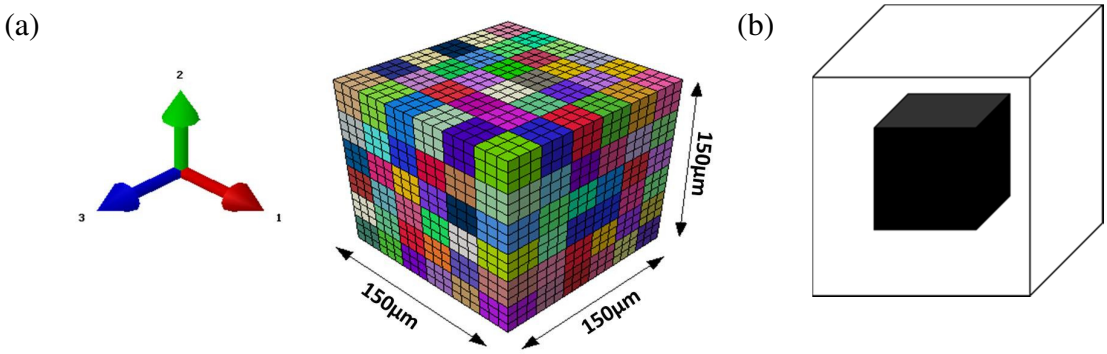


Fig. 4-1: 3-D models adopted in developing localization criterion (a) Model I with no imperfection (b) Model II with an inherent imperfection. Note that material properties are specified in Table 3-1.

Initial textures

Two textures have been investigated in this study as shown by the pole figures in Fig. 3-12. Texture R-1 shown in Fig. 3-12a is a nominally random BCC texture while FS-1 represents a ferritic steel texture of interest to the auto-industry. Although texture R-1 is approximately

random, it should be realized that in fact a certain degree of non-randomness remains and the consequences of this are discussed later.

Localization criterion

The onset of necking is determined by evaluating local critical grains developing plastic strains in the polycrystal model based on the increments of plastic strain between incremental loading times t_n and t_{n+1}, normalized with respect to the macro plastic strain increment within the corresponding states. This criterion is similar to the approach adopted by Situ and Jain [30] and Volk and Hora [29]. However, unlike these aforementioned approaches which are hybrid techniques based on experimental prediction of limit strain based on computational algorithms, the method presented here accounts for localization at the granular level based entirely on a crystal plasticity framework.

Here, the average plastic strain increment (dq_j) in each grain (j) is normalized with respect to the overall average plastic strain increment ($d\bar{p}$) generated in the polycrystal such that

$$dq_j = \frac{1}{V}\int \dot{p}_j \Delta t \, dV = \frac{1}{V}\sum_{i=1}^{N_g} \Delta p_{j_i} \Delta V_j \qquad 4\text{- }1$$

where i represents elements within a grain j in a polycrystal with a total number of grains, N_g. The normalized average plastic strain increment for each grain at each deformation state $t=t_1$, t_2,…, t_n is calculated such that;

$$\hat{q}_j^{t_n} = \frac{dq_j^{t_1}}{d\bar{p}^{t_1}}, \frac{dq_j^{t_2}}{d\bar{p}^{t_2}}, \ldots, \frac{dq_j^{t_n}}{d\bar{p}^{t_n}} \qquad 4\text{- }2$$

Fig. 4-2 shows a typical result of the calculation for a section through the random polycrystal subjected to uniaxial plane strain deformation, in which the highly localized nature of $\hat{q}_j^{t_n}$ is apparent. A set of critical grains is then selected numerically from results such as those

shown in Fig. 4-2 at each deformation state based on the highest values of $\hat{q}_j^{t_n}$ and the average value, Γ is obtained. That is,

$$\Gamma = \frac{1}{N_c}\sum_{i=1}^{N_c} \hat{q}_i^{t_n} \qquad 4\text{- }3$$

where N_c is the total number of critical grains selected at each deformation state. The onset of localization is determined by calibrating the critical value of the normalized, averaged incremental plastic strain, Γ_c, using experimental data obtained from Nakajima tests on ferritic steel samples.

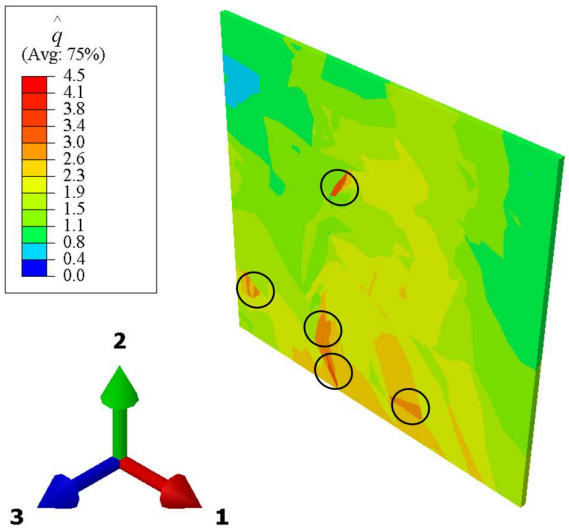


Fig. 4-2: Cross-section of a polycrystal with critical grains accumulating plastic strain relative to the polycrystal indicated by the rings. $\hat{q}$ represents the normalized average plastic strain increment at a particular deformation state (t_n) i.e. $\hat{q}_j^{t_n} = dq_j^{t_n}(d\bar{p}^{t_n})^{-1}$ where $dq_j^{t_n}$ is the plastic strain increment in grain j and $d\bar{p}^{t_n}$ is the increment of average plastic strain for all grains in the polycrystal.

A characteristic response is shown in Fig. 4-3. Γ_c is calibrated by evaluating the value of Γ, at the deformation state in the loading history of the deforming polycrystal model that corresponds to the experimentally determined principal strain limit of a particular experimental reference steel subjected to uniaxial plane strain conditions. Conditions of

uniaxial plane strain are selected because these typically give the lowest strain to failure on a forming limit diagram. For the experimental reference steel employed here, this corresponds to strains of $\varepsilon_1, \varepsilon_2 = (0,0.32)$. This is indicated along the loading history in Fig. 4-3 at 0.53s. The value of Γ is extracted at that particular instance and adopted as the critical value, $\Gamma = 2.8$, below which homogenous deformation is assumed and above it, localization. In other words, the onset of localization is specified as the deformation state when Γ exceeds the critical value indicated in Fig. 4-3.

The choice of the critical grain set size (N_c) has also been investigated by choosing different sizes in order to evaluate its effect on the predicted onset of localization. This is undertaken by evaluating different sizes of critical grain sets for the polycrystal model (Fig. 4-1a) subjected to uniaxial plane strain loading and measuring the response of Γ along the loading history. Three critical grain set sizes (N_c= 3, 5 and 10) have been investigated and the response to each set size is shown in Fig. 4-4. Fig. 4-4 indicates that the size of the critical grain set chosen does not strongly affect the evolution of Γ, the normalized, average incremental plastic strain and for this reason, for all subsequent analyses in this chapter, a critical grain set size of five is adopted. In the polycrystal model used, this corresponds to a subset of 2.5% of all grains which undergo localization. This failure criterion is now used to predict limit strains under proportional and non-proportional strain paths.

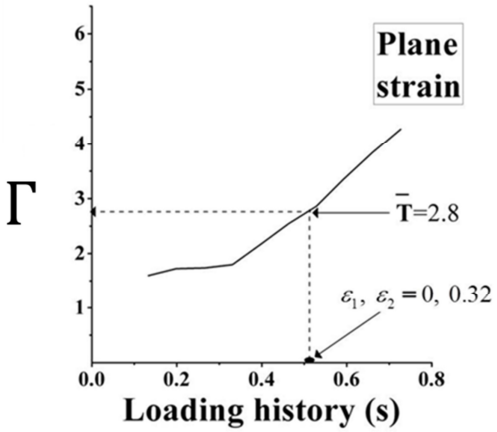


Fig. 4-3: Characteristic response of the normalized plastic strain in a deforming polycrystal. $\Gamma = \frac{1}{N_c}\sum_{i=1}^{N_c} \hat{q}_i^{t_n}$ is the average normalized incremental plastic strain of the set of critical grains selected numerically from results such as those shown in Fig. 4-2.

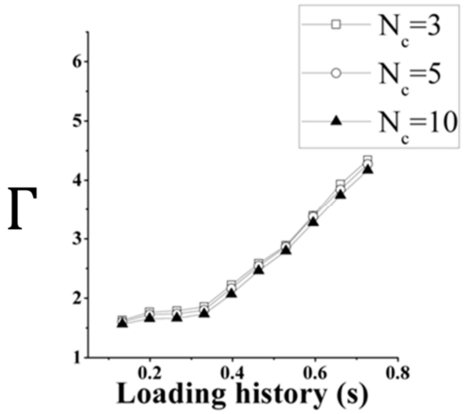


Fig. 4-4: Sensitivity of the normalized, average incremental plastic strain to the critical grain set size for an initially random polycrystal subjected to plane strain conditions up to arbitrary strains. $\Gamma = \frac{1}{N_c}\sum_{i=1}^{N_c} \hat{q}_i^{t_n}$ is the average normalized incremental plastic strain of the set of critical grains selected numerically from results such as those shown in Fig. 4-2.

4.2. Predicted limit diagrams for proportional straining

The forming limit curve under proportional strain paths has been predicted by subjecting the polycrystal in Fig. 4-1a to a range of strain paths shown in Fig. 4-5. These proportional strain paths (A-E) were applied to the positive 1- and 2- surfaces up to arbitrary strain levels and the onset of localization along each path based on the normalized, incremental average plastic strain is predicted.

The response of the two polycrystal models described in section 4.1 has been evaluated. The first model comprises 216 grains with $3 \times 3 \times 3$ C3D8R elements and has been assigned an approximately random texture (R-1) shown in Fig. 4-12a. The second model is similar to the first but with a central imperfection comprising a group of eight grains ($2 \times 2 \times 2$) at the centre of the model, all assigned the reference crystallographic orientation as described previously. The predicted limit strain curves corresponding to the two models are shown in Fig. 4-6a and 4-6b respectively for the proportional strain paths shown in Fig. 4-5a. By comparing the results from the models, it is apparent that only small differences exist in the predicted forming limits. Whilst the differences may be more pronounced with a larger imperfection, that will immediately lead to a discussion on the assigned material properties of the incorporated imperfection. Also, the predicted limit strains without the imperfection are in close agreement with experimental data by Volk and Hora [29] shown in Fig. 4-5b. Therefore, for all subsequent analyses in this chapter, the model without an initial imperfection is adopted in the prediction of localization. However, the primary intent in this chapter is in non-proportional straining effects and these are introduced in the following section.

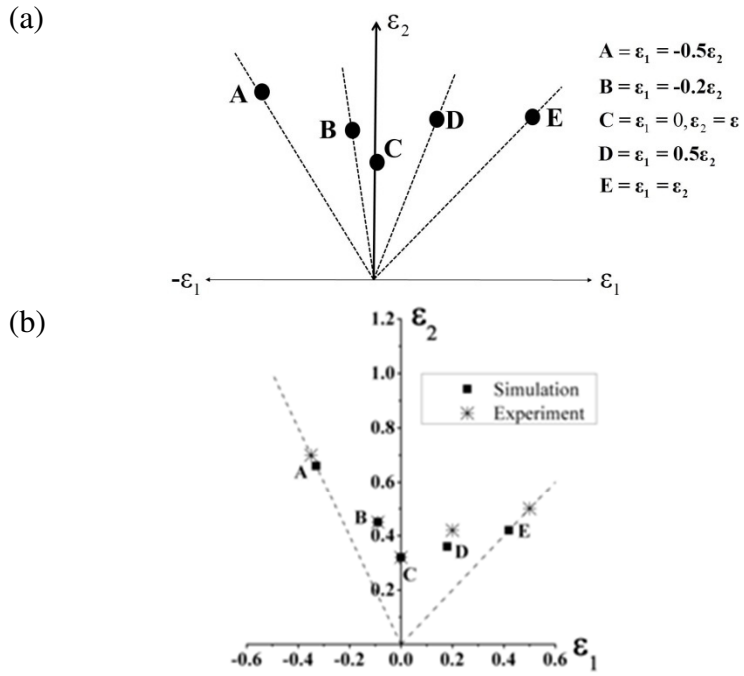


Fig. 4-5: Proportional strain paths followed (a) for the prediction of limit strain (b) based on the polycrystal in Fig. 4-1.

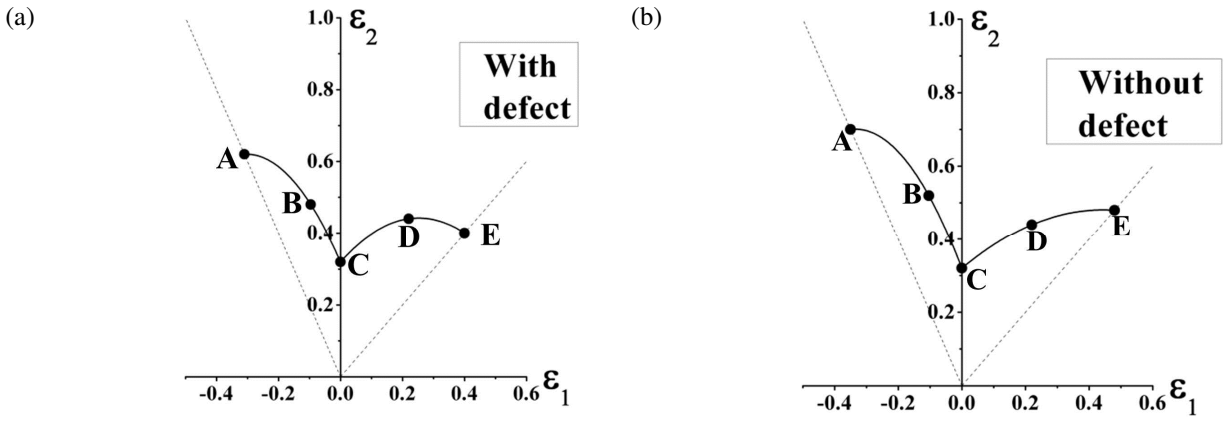


Fig. 4- 6: Predicted limit strains under proportional strains (a) with defect in model (b) without imperfection in model. A, B, C, D and E indicate the proportional strain paths illustrated in Fig. 4-5.

4.3. Measure of non-proportionality

Non-proportional strain paths comprising two phases such as that shown in Fig. 4-7 are applied to the oligocrystal in Fig. 4-1a to a final biaxial (A) and uniaxial (B) state. The limit strain for each combined strain path is to be determined but first a methodology for defining the level of non-proportionality is developed in order to be able to relate the limit strains obtained for degrees of non-proportionality relative to those for proportional straining. Consider the two non-proportional straining paths B-3a; B-3b and B-5a; B-5b terminating at the end state A, also achievable by the proportional path B-1. In a polycrystal with an initially random texture, it could be argued that the two non-proportional paths would lead to similar material states (in terms of dislocation distributions and textures due to symmetry at least for the case of isotropic latent-hardening) at point A. However, in an initially textured polycrystal, the two non-proportional paths are immediately asymmetric and likely to lead to very different material states at A. Hence, any measure of non-proportionality must differentiate between these (and other) non-proportional strain paths.

The measure of non-proportionality defined here is based on the angle between the two strain paths for a particular non-proportional strain path as illustrated in Fig. 4-7. This measure ($\mathrm{np} = \sin(\varphi)$), unlike that proposed by Schmitt [57], is able to account for directionality in initially textured polycrystals for which asymmetric response (with respect to the path of proportionality) is expected. The Schmitt [57] non-proportionality measure is valid in a random polycrystal in which symmetry in material states under non-proportional strain paths exist about the proportional paths.

Consider the proportional strain path in Fig. 4-7 denoted as B-1, the non-proportional angle (φ_1) is 180 degrees, hence, np = 0. However, for a strain path such as B-3 comprising orthogonal (plane) strain paths (B-3a and B-3b), the non-proportional angle is φ_3=+90^0 degrees. To ensure consistency, angular deviations of strain paths below the proportional path are considered positive angles while the deviations above the proportional case are considered negative. Therefore, np=+1 for strain path B-3 while np=-1 for strain path B-5. This methodology can be applied similarly to non-proportional paths which produce a final uniaxial strain state.

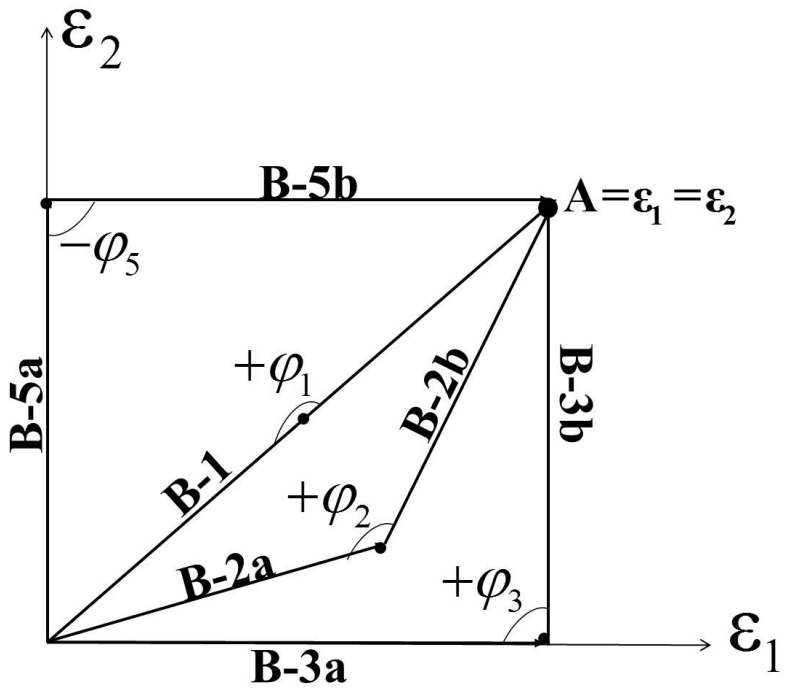


Fig. 4-7: Description of the measure of non-proportionality showing the measurement of deviation angles from the proportional case.

4.4. Effects of texture, hardening and non-proportionality on limit strain in BCC polycrystals

The effects of non-proportionality on limit strains are investigated in this section by adopting non-proportional strain paths to an identical final state and evaluating the onset of localization along the corresponding loading history. Empirical evidence has shown that following non-proportional paths to an identical strain state results in the formation of varying dislocation distributions. Here, the dislocation distributions corresponding to non-proportional paths to final biaxial (A) and uniaxial (B) states shown in Fig. 4-1 are presented in Fig. 4-8 for an initially random textured polycrystal. Consider the structures formed during non-proportional paths to a final biaxial state under self-hardening rules shown in Fig. 4-8a. Clearly defined dislocation distributions are observed however, the differences in the structures formed as a result of the differing non-proportional straining paths applied are mild. In fact, only subtle differences are observed at an identical final biaxial state. However, consider the dislocation distributions formed for the differing non-proportional paths to an identical uniaxial state under self- and isotropic latent-hardening shown in Fig. 4-8c & 4-8d respectively. Clearer differences in the dislocation distributions are observed due to the loss of symmetry associated with uniaxial strains. As a result of these differences in the dislocation distributions, it is hypothesized that non-proportionality effects are likely to be more apparent during non-proportional uniaxial strains. The dislocation structures shown in Fig. 4-8 are on the basis of the primary 12 {110}<111> BCC slip systems which results in lesser accuracy than adopting the 12 {112}<111> slip systems in addition to the primary systems**.** In Fig. 4-8e, the primary slip systems are incorporated in addition to the {112}<111> slip systems to predict dislocation distributions at a final uniaxial state under

isotropic latent-hardening. In comparison to the response from similar strain paths based on the primary systems alone shown in Fig. 4-8d, differences in predicted dislocation distributions are observed especially for modest deviations from strain proportionality (path U-3I). However, the behavioral trends remain the same and for this reason, only the primary slip systems are used for predictions henceforth in this chapter for simplicity and computational efficiency.

Fig. 4-9 shows predicted failure states under non-proportional paths for the initially random texture (R-1) and the ferritic steel texture (FS-1) under isotropic latent- and anisotropic self-hardening. In Fig. 4-9, the various proportional and non-proportional strain paths investigated are shown by the light, solid lines. Along each path, the point in the straining history at which the localization or strain limit is achieved, as predicted by the model, is shown by a symbol, differentiating between the initially (nominally) random polycrystal and the textured polycrystal, whose pole figures are shown in Fig. 4-12.

Consider the biaxial part of Fig. 4-9a (right side), for texture R-1. The failures along the non-proportional paths are approximately symmetric about the proportional case. The mild loss of symmetry results from the fact that the nominally random initial texture is not, in fact perfectly random. However, much greater asymmetry results from the initially textured polycrystal, as shown in Fig. 4-9a. The asymmetry is even greater in the uniaxial case in Fig. 4-9a (left side), and it is clear that non-proportionality affects the onset of localization. Similarly, under anisotropic self-hardening, the onset of localization is affected by non-proportionality, but, generally, lower failure strains are predicted.

Figs. 4-10 and 4-11 provide a better understanding of the effects of non-proportional strain paths on limit strain. The measure of non-proportionality outlined in the previous section is here utilized and the figures show the dependence of the final accumulated plastic strain at the onset of localization on the level of non-proportionality, thus providing a quantitative measure of the ductility achievable by following non-proportional strain paths. Consider Fig. 4-10 which shows the average accumulated plastic strain normalized by the biaxial strain response for a range of non-proportional paths denoted by np. For clarity, np=$\pm$1 represents consecutive plane strain paths to a final biaxial state while -1 < np < 1 gives a range of non-proportional strain paths towards an identical final biaxial state. np=0 represents the proportional strain path. Note that positive values of np correspond to strain paths that fall below the proportional path (B-1 or U-1 in Fig. 4-8) and vice versa.

In Fig. 4-10a, approximate symmetry about the proportional strain path (np = 0) is observed in texture R-1 (initially random). However, a small deviation from symmetry resulting from the incomplete randomness of texture R-1 is observed. As a result, the predicted average plastic strain at the onset of localization for np=1 deviates marginally from np= -1. Overall, the proportional strain path is seen to show the highest ductility. For the case of the ferritic steel texture, FS-1, a more pronounced skew is seen by examining the ductility levels for values of np ranging from -1 to +1. It can be seen that the ferritic steel texture FS-1 shows much higher ductility compared to texture R-1 at np = 0.43, thus indicating that particular strain paths combined with a favorable texture can lead to high levels of ductility. This is further elaborated in Fig. 4-10b for anisotropic self-hardening behavior. Here, the incomplete randomness of texture R-1 is more visible as a non-proportional path shows higher ductility

(np=-0.43) as compared to the behavior seen under isotropic latent-hardening in Fig. 4-10a. However, perfectly random texture is expected to show the highest ductility under proportional strains.

The effects of non-proportionality are hypothesized to be more evident under non-proportional uniaxial strain paths based on the predicted dislocation distributions for an initially random polycrystal shown in Figs. 4-8c and 4-8d. The results shown in Fig. 4-11 indicate a higher ductility is achievable under non-proportional paths especially at np = 1 in both textures and under both hardening rules. In Figs. 4-11a and 4-11b, the highest level of ductility is observed by following the extreme non-proportional path comprising compression followed by tension to achieve a final uniaxial strain state.

Further, considering Fig. 4-11a, two important points arise. Firstly, an interesting peak is observed in the initially random texture (R-1) at np = -0.4 denoting that a particular non-proportional path results in higher ductility. This response emphasizes the strong coupling between texture and the applied strain path. Thus, texture evolution greatly affects the localization behaviour observed. Secondly, relatively high ductility is achieved for positive values of np (compression followed by tension). This behaviour is evident in both textures and further illustrates the strong links between texture and predicted limit strains.

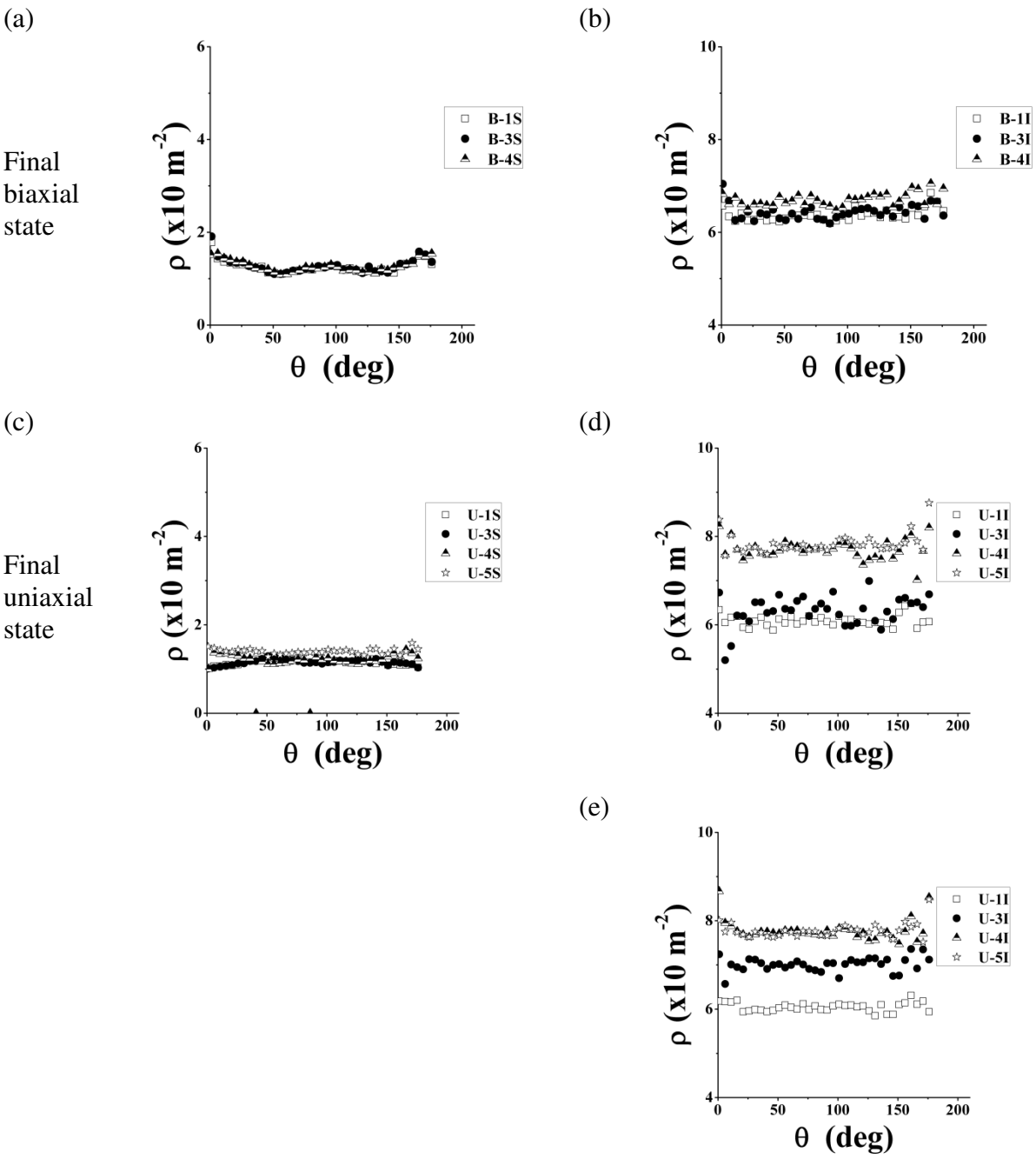


Fig. 4-8: Dislocation distributions for random polycrystal R-1 under self- and isotropic latent-hardening at an identical strain state (a) dislocation distribution at final biaxial state under self-hardening (b) dislocation distribution at final biaxial state under isotropic latent-hardening (c) dislocation distribution at final uniaxial state under self-hardening (d) dislocation distribution at final uniaxial state under isotropic latent-hardening rules (e) dislocation distribution at final uniaxial state under isotropic latent-hardening rules using 24 slip systems i.e. 12 {110}<111> + 12 {112}<111>. Note that $\varepsilon_1 = \varepsilon_2 = 0.25$ for the biaxial cases and $\varepsilon_1 = -0.5\varepsilon_2 = -0.125$ for the uniaxial case.

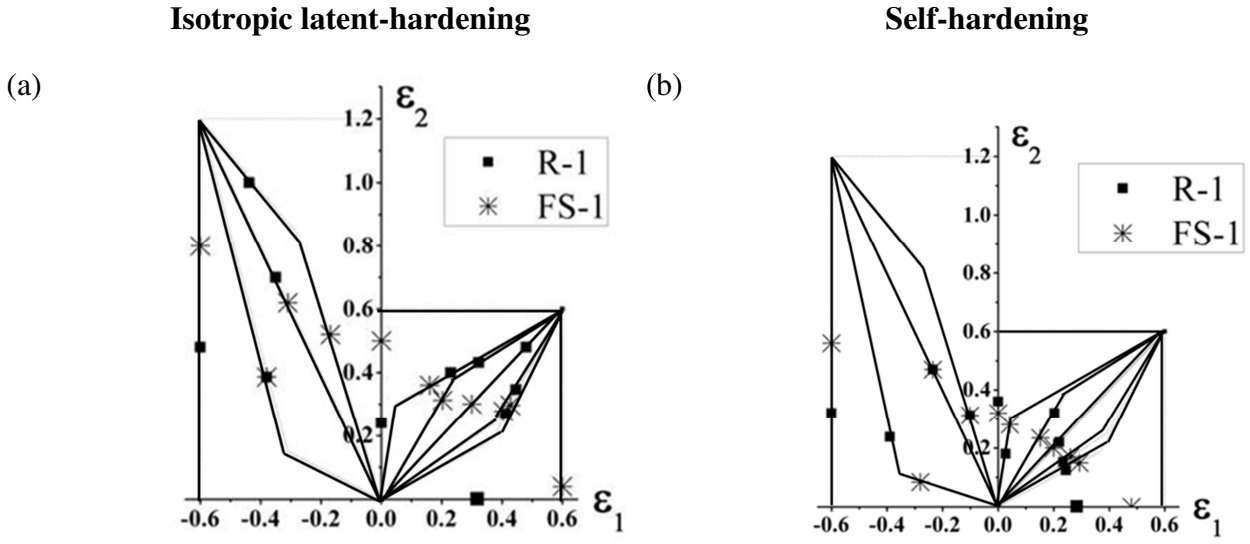


Fig. 4-9: Non-proportional paths indicating onset of localization (a) Isotropic latent-hardening (b) anisotropic self-hardening Note that R-1 indicates the response of an initially random polycrystal texture and FS-1 is an initially textured polycrystal. The pole figures of both textures are shown in Fig. 4-12.

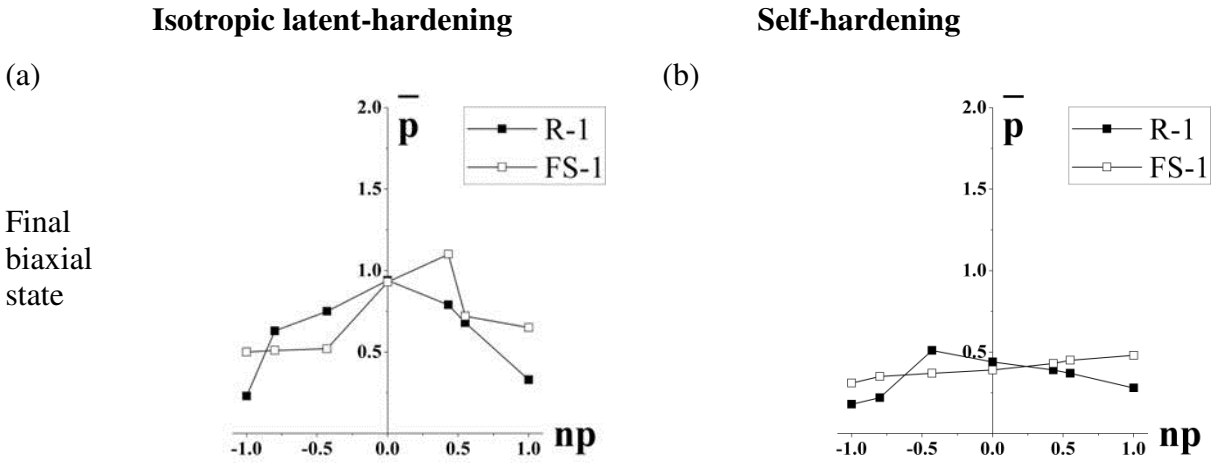


Fig. 4-10: Average plastic strains in the model at failure as a function of non-proportionality for varied strain paths to a final biaxial state (a) isotropic latent-hardening (b) self-hardening. Note that R-1 indicates the response of an initially random polycrystal texture and FS-1 is an initially textured polycrystal. The pole figures of both textures are shown in Fig. 4-12.

Isotropic latent-hardening **Self-hardening**

(a) (b)

Final uniaxial state

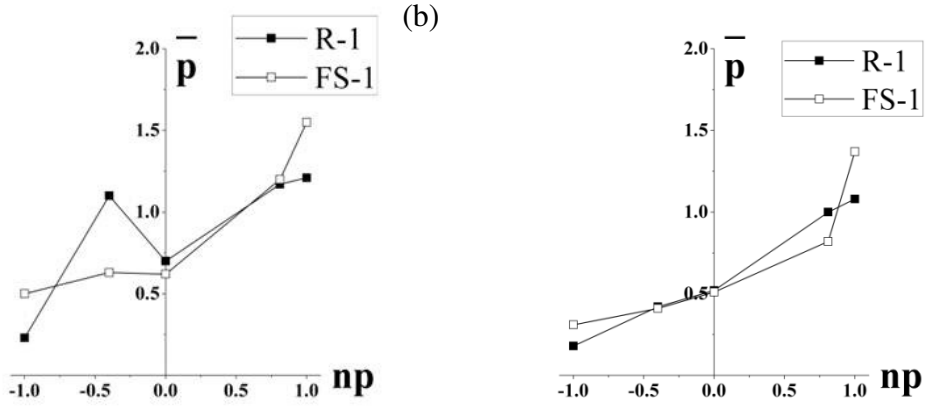


Fig. 4-11: Average plastic strains in the model at failure as a function of non-proportionality for varied strain paths to a final uniaxial state (a) isotropic latent-hardening (b) self-hardening. Note that R-1 indicates the response of an initially random polycrystal texture and FS-1 is an initially textured polycrystal. The pole figures of both textures are shown in Fig. 4-12.

4.5. Conclusions

The coupled effects of texture, hardening and non-proportionality on limit strains in BCC polycrystals have been investigated. The effects of two extremes of hardening (isotropic latent- and anisotropic self-hardening) are evaluated and their effects on localization of BCC polycrystals subjected to non-proportional strain paths, presented. The limit strains along non-proportional strain paths to identical final uniaxial and biaxial states are predicted and further illustrated using a measure of non-proportionality.

The analyses show that texture and non-proportionality strongly affect predicted limit strain. In particular, it has been shown that for both biaxial and uniaxial straining, following paths which are non-proportional can lead to both increases and decreases in strains to the onset of localization. There is the potential, therefore, for the careful selection of pre-forming texture combined with non-proportionality path in order to maximize the strains achievable in forming. The differences in strain to failure resulting from differing initial textures and non-proportionality path occur because of the establishment of dislocation distributions which are texture and path dependent.

Further to developing an understanding of non-proportionality and the role of texture on dislocation distribution presented so far, it is further imperative to evaluate the role of strain distributions under differing deformation pathways. The effects of strain distributions can be evaluated in two fold; elastic strains and the plastic strain gradients (GNDs). Both measures of strain are accommodated during deformation and are important to further understanding non-proportionality effects. This is addressed in the next chapter.

Chapter V

5. Lattice strain distributions due to elastic distortions and GND development in polycrystals

This chapter addresses lattice strain distributions due to both elastic distortions and the development of geometrically necessary dislocations (GNDs) in polycrystals. Considering the range of ideal hardening rules used to investigate the effects of non-proportionality, it is important to properly calibrate the hardening rules such that more representative effects of non-proportionality are seen. A proposed method involves comparing lattice distortion obtained from experiment with that calculated from finite element simulations in order to calibrate the hardening rule. Here, a methodology is developed to calculate the total lattice distortion developed in a polycrystal due to the contributions from elastic strains and plastic strain gradients (GNDs).

5.1. Lattice spacing changes due to deformation

The thrust of this chapter is focused on investigating lattice spacing distributions in polycrystals due to elastic distortions and GND development (with the meanings discussed earlier). So far, classical crystal plasticity studies on this subject in the literature have focused on local elastic distortions only, as opposed to those from long range strain fields resulting from GNDs [58-60]. However, GNDs arising from plastic strain gradients are expected to affect lattice spacing. Thus, a systematic study investigating the contribution of GNDs is presented. The methodology is discussed first for contributions of elastic distortions to lattice spacing changes, followed by GND development and then, for both mechanisms combined.

This chapter focuses on cubic crystals shown in Fig. 5-1. An undeformed cubic crystal in which $a = b = c;\ \alpha = \beta = \gamma = 90^0$ is shown in Fig. 5-1a, and a deformed triclinic crystal is shown in Fig. 5-1b in which $a' \neq b' \neq c';\ \alpha' \neq \beta' \neq \gamma'$. However, consider Fig. 5-1c, in which the lattice spacing d_{hkl} for an *hkl* plane such as (100) in the undeformed state is denoted by d^0. Following uniaxial deformation, the lattice spacing for the (100) plane is denoted by d^f. The undeformed lattice spacing for any plane in the cubic crystal is obtainable using Eq. 5-1

$$d_{hkl} = \frac{a}{\sqrt{h^2+k^2+l^2}} \qquad 5\text{- }1$$

where a is the lattice parameter and h, k and l are the intersections of the plane with the crystal axes.

The lattice spacing formula for triclinic crystals where $a' \neq b' \neq c';\ \alpha' \neq \beta' \neq \gamma'$ provides the most general method of calculating the lattice spacing in a deformed cubic crystal. Thus, the lattice spacing (d_{hkl}) obtained from Cullity and Stock [61] is

$$d_{hkl} = \sqrt{\frac{V^2}{S_{11}h^2+S_{22}k^2+S_{33}l^2+2S_{12}hk+2S_{23}kl+2S_{13}hl}} \qquad 5\text{- }2$$

where the parameters in Eq. (5-2) are defined in Appendix A and assumes that all deformed planes remain planar.

Fig. 5-2 shows a flow chart describing the process adopted to bin lattice spacing variations associated with a particular *hkl* plane. Consider a deformed heterogeneous polycrystal. The variations in grain orientation result in a distribution of lattice spacing for each *hkl* plane. Now consider favorably oriented {111} planes in the polycrystal, for which a distribution of lattice spacing is expected about the ideal. The ideal position is that for an unstrained single crystal in the local configuration and from Eq. 5-2, d^0_{111} for example is 1.657Å assuming

2.87Å. A tolerance range (Δd^0_{hkl}) can then be set to bin the distribution of lattice spacing about the ideal position by frequency using a step size of 0.0001Å. This tolerance range is selected based on experimental neutron diffraction data for a ferritic steel polycrystal subjected to 50% equibiaxial strains [62]. By assuming a representative constant wavelength ($\lambda^* = 1.7$Å) and applying Eq. 2-2, the lattice spacing corresponding to a 1^0 deviation for that plane in an unstrained cubic crystal is calculated. For example, $2\theta^0_{100} = 34.455^0$ corresponds to a lattice spacing $d^0_{111} = 2.87$Å. Assuming a 1^0 deviation, the tolerance region for the $\{100\}$ plane is calculated such that $2.7916 \leq d_{100} \leq 2.9532$ where $d_{2\theta_{100}+1} = 2.7916$Å and $d_{2\theta_{100}-1} = 2.9532$Å respectively. The frequency of occurrence of a given lattice spacing may then be plotted against the lattice spacing itself in order to generate the peak distribution of lattice spacing. The width at half maximum (FWHM) is then obtained for the distribution of lattice spacing deviations from the ideal. Note that the FWHM determined in this way is different to that obtained from x-ray diffraction. However, it is anticipated that the lattice spacing peaks determined as outlined are likely to be indicative of those observed in x-ray diffraction experiments.

Now, in order to obtain the lattice spacing in the deformed crystal, the post deformation lattice parameters (a, b and c in Fig. 5-1) are required. In this study, the post deformation lattice parameters are calculated due to elastic distortions, GND development and for both mechanisms combined. This is presented in the next section.

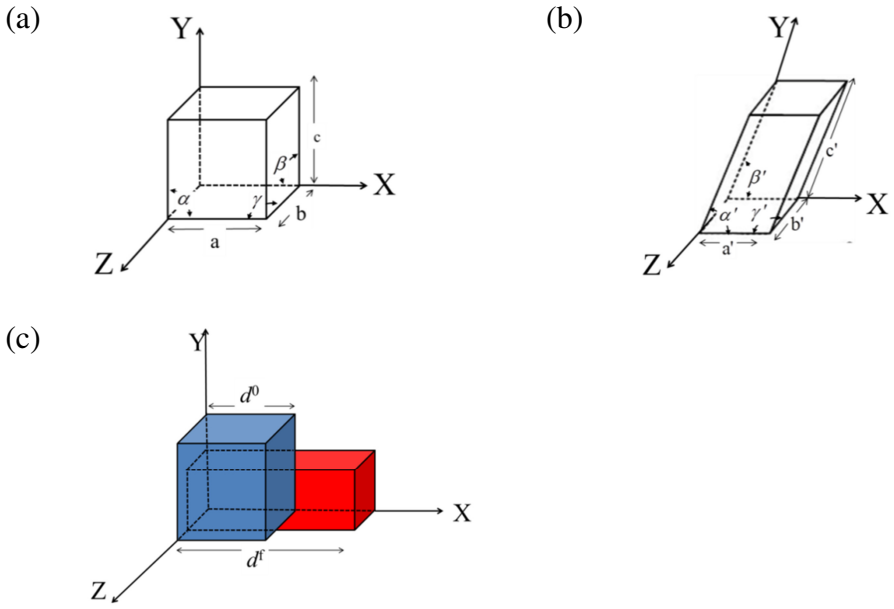


Fig. 5-1: Schematic of crystal structures showing (a) cubic with $a = b = c$; $\alpha = \beta = \gamma = 90^0$, (b) triclinic with $a' \neq b' \neq c'$; $\alpha' \neq \beta' \neq \gamma'$ and (c) a cubic crystal undergoing uniaxial elongation showing the undeformed (100) plane spacing, d^0, and then after elastic distortion, d^f.

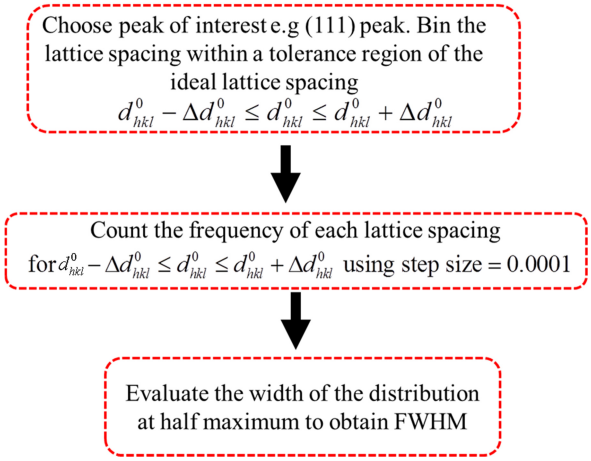


Fig. 5-2: Flow diagram showing the binning process of lattice spacing, d, the further refinement of the binned lattice spacing by frequency of occurrence and calculation of the width of the distribution at half maximum (FWHM).

5.1.1.Lattice spacing changes due to elastic distortions

The lattice spacing between corresponding successive planes changes with increasing elastic strains. The post deformation lattice parameters are required and calculated here within a crystal plasticity framework.

Consider Fig. 5-3 which shows a single crystal in its reference configuration with orthogonal direction vectors $\boldsymbol{e}_1$, $\boldsymbol{e}_2$, and $\boldsymbol{e}_3$ along the $\boldsymbol{X}$, $\boldsymbol{Y}$ and $\boldsymbol{Z}$ global directions respectively. The reference crystal can be rotated into its undeformed local crystallographic configuration by $\boldsymbol{R}_0^c$. The deformed state can then be achieved via two pathways: from the deformation gradient, $\boldsymbol{F}$ or by its multiplicative decomposition into the plastic, $\boldsymbol{F}^{\mathrm{p}}$, and elastic $\boldsymbol{F}^e$ components. The plastic component generates slip in the relaxed or stress-free state while the elastic deformation leads to distortion and rotation. The deformation stages are described since they establish the configuration against which changes in lattice spacing are to be measured.

The crystal deformation is measured with respect to the deformed x', y' and z' configuration which differs in general from the deformed crystallographic frame, x_c', y_c' and z_c' shown in Fig. 5-3. In x-ray diffraction for example, changes in lattice spacing are local measurements with respect to the crystallographic frame. Therefore, lattice spacing calculations need to be carried out with respect to the local lattice orientation labeled x_c', y_c' and z_c', within the deformed configuration, shown in Fig. 5-3.

First, consider the elastic deformation gradient $\boldsymbol{F}^{e}$ due to elastic strains and continuum rigid body rotations. From Fig. 5-3, $\boldsymbol{F}^{e}$ maps the relaxed configuration into the deformed configuration and as a result, is already in the desired configuration.

The unit orthogonal vectors shown in Fig. 5-3 are rotated into the deformed crystallographic configuration using

$$\boldsymbol{e}_i^{\mathrm{c}} = \boldsymbol{\Delta R}^{\mathrm{c}} \boldsymbol{R}_0^{\mathrm{c}} \boldsymbol{e}_i \qquad 5\text{- }3$$

where i =1, 2 and 3 corresponds to the $\boldsymbol{x}$, $\boldsymbol{y}$, and $\boldsymbol{z}$ directions respectively and $\boldsymbol{\Delta R}^{\mathrm{c}}$ maps the undeformed crystal orientation into the deformed state shown in Fig. 5-3. Using the elastic deformation gradient $\boldsymbol{F}^{\mathrm{e}}$, the post-deformation lattice lengths due to elastic distortions are determined from

$$\frac{a'_{\mathrm{e}}}{a_0} = |\boldsymbol{F}^{\mathrm{e}} \boldsymbol{e}_1^{\mathrm{c}}|, \frac{b'_{\mathrm{e}}}{b_0} = |\boldsymbol{F}^{\mathrm{e}} \boldsymbol{e}_2^{\mathrm{c}}|, \frac{c'_{\mathrm{e}}}{c_0} = |\boldsymbol{F}^{\mathrm{e}} \boldsymbol{e}_3^{\mathrm{c}}| \qquad 5\text{- }4$$

where a_0 , b_0 and c_0 are the undeformed lattice lengths. With knowledge of the deformed lattice lengths, the lattice spacing for all possible *hkl* planes can be obtained using Eq. 5-2.

5.1.2.Lattice spacing changes due to GND development

Consider Fig. 5-4 which shows a schematic diagram of deformation in a beam classified into three regions (A, B and C). In regions A and C, the statistically stored dislocation dipoles cancel resulting in a zero net Burger's discontinuity about the enclosed region. Hence, the lattice spacing changes in this region can be described by elastic distortions only. However, region B is shown to have a finite vector discontinuity $\boldsymbol{B}$ which contributes to lattice curvature and therefore to lattice spacings. Naturally, the size of the beam considered is important, since at the length scale of discrete dislocations, all dislocations generate lattice

curvature and may be considered geometrically necessary. Length scales such as these have been investigated by Benzerga [63]. They reported the effects of varying length scales and their results show that at very small length scale (typically 0.1μm), the effects of GNDs are very large. However, as length scale increases, the effect of an increase (e.g. from 1 μm to 2 μm) becomes smaller. The smallest typical length scale considered here is 1 μm which we argue is sufficiently large enough to be able to ignore the discreteness of dislocations. The methodology adopted to determine $\boldsymbol{B}$ is presented, within the context of the crystal plasticity finite element method. With knowledge of the Burger discontinuity vector, $\boldsymbol{B}$, on three orthogonal planes to be defined, it becomes possible to determine the additional lattice distortions which result from the discontinuity.

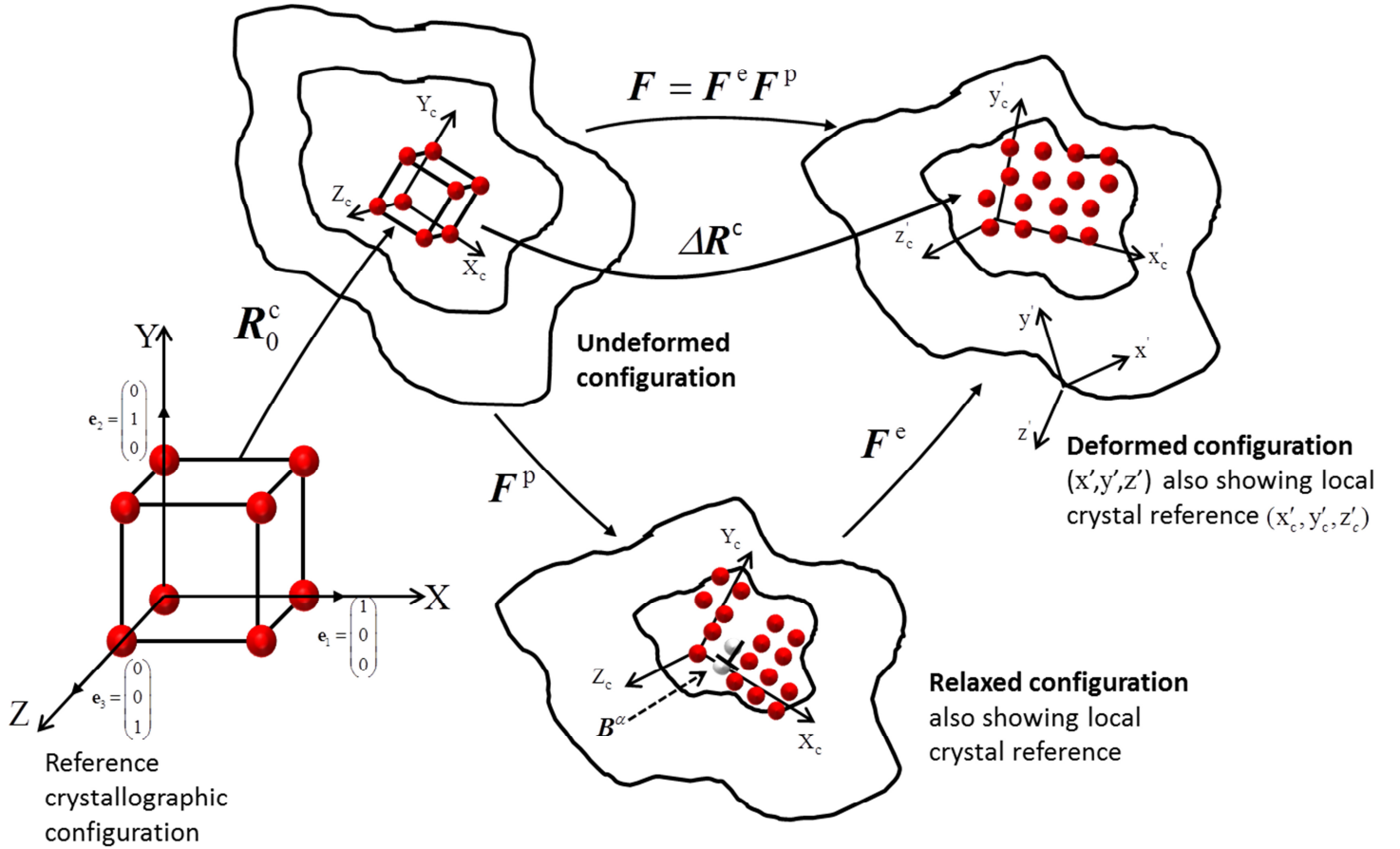


Fig. 5-3: Schematic diagram showing the relationship between the undeformed, deformed and relaxed configurations and the corresponding crystallographic orientations in relation to the reference crystallographic configuration.

The discontinuity $\boldsymbol{B}$ in Fig. 5-4 on completion of a Burger's circuit around the path Γ on an infinitesimal surface, S, with normal $\boldsymbol{n}$, is obtainable from Eq. 5-5 with knowledge of the local plastic deformation gradient. Fig. 5-5a shows a body containing a representative volume element (RVE) which itself contains many grains of known crystallographic orientation. An example grain (i) is shown within the RVE in Fig. 5-5b. The grain is discretized with many finite elements shown schematically in Fig. 5-5b and a typical element (j) is shown in Fig. 5-5c with surfaces S_1, S_2 and S_3 having outward normals $\boldsymbol{n}_1$, $\boldsymbol{n}_2$ and $\boldsymbol{n}_3$. The Burger's vector discontinuity on the three orthogonal surfaces S_1, S_2 and S_3 can then be determined from Eq. 5-5 as

$$\boldsymbol{B}_k = \int \mathrm{curl}(\boldsymbol{F}^{\mathrm{p}})\boldsymbol{n}_k \boldsymbol{dS}_k \qquad 5\text{-}5$$

where k=1, 2 and 3 corresponding to each surface. Within the finite element discretization, the length normalized Burger's vector discontinuity may be approximated at the element level by

$$\boldsymbol{B}^l{}_k \cong \mathrm{curl}(\boldsymbol{F}^{\mathrm{P}})\boldsymbol{n}_k \frac{\Delta A_k}{L_k} \qquad 5\text{-}6$$

in which ΔA_k is the appropriate finite element-level surface area on each of the orthogonal surfaces S_k with normal $\boldsymbol{n}_k$ and L_k is the associated length scale of the surface with normal $\boldsymbol{n}_k$ of the finite element. Note that $\boldsymbol{B}^l{}_k$ is now a normalized and dimensionless quantity. The methodology for the calculation of the strain gradient terms ($\mathrm{curl}(\boldsymbol{F}^{\mathrm{p}})$) is detailed in Appendix B, and a validation of the technique is presented later.

The lattice stretch ratio components $\frac{\Delta a}{a}$, $\frac{\Delta b}{b}$ and $\frac{\Delta c}{c}$ resulting from the presence of the Burger discontinuity may then be determined with respect to each of the orthogonal planes, and in the XY plane,

$$\frac{\Delta a}{a_0} = \boldsymbol{B}^l{}_3 \cdot \boldsymbol{e}'_1 \,, \frac{\Delta \mathrm{b}}{b_0} = \boldsymbol{B}^l{}_3 \cdot \boldsymbol{e}'_2 \text{ and } \frac{\Delta c}{c_0} = \boldsymbol{B}^l{}_3 \cdot \boldsymbol{e}'_3 \qquad \text{5- 7a}$$

and, for the YZ plane,

$$\frac{\Delta a}{a_0} = \boldsymbol{B}^l{}_1 \cdot \boldsymbol{e}'_1 \,, \frac{\Delta \mathrm{b}}{b_0} = \boldsymbol{B}^l{}_1 \cdot \boldsymbol{e}'_2 \text{ and } \frac{\Delta c}{c_0} = \boldsymbol{B}^l{}_1 \cdot \boldsymbol{e}'_3 \qquad \text{5-7b}$$

and finally, in the XZ plane,

$$\frac{\Delta a}{a_0} = \boldsymbol{B}^l{}_2 \cdot \boldsymbol{e}'_1 \,, \frac{\Delta \mathrm{b}}{b_0} = \boldsymbol{B}^l{}_2 \cdot \boldsymbol{e}'_2 \text{ and } \frac{\Delta c}{c_0} = \boldsymbol{B}^l{}_2 \cdot \boldsymbol{e}'_3 \qquad \text{5-7c}$$

where $\boldsymbol{e}'_i = \boldsymbol{R}^c_0 \boldsymbol{e}_i$ are the local crystallographic orthogonal unit direction vectors rotated into the undeformed lattice orientation shown in Fig. 5-3. Note that $a_0 = b_0 = c_0$ are the undeformed cubic crystal lattice parameters.

From Eqs. 5-7, the lattice stretches taking account of the contribution from each plane are given by

$$\begin{aligned} \Delta a &= (\boldsymbol{B}^l{}_3 \cdot \boldsymbol{e}'_1 + \boldsymbol{B}^l{}_1 \cdot \boldsymbol{e}'_1 + \boldsymbol{B}^l{}_2 \cdot \boldsymbol{e}'_1) a_0 \\ \Delta b &= (\boldsymbol{B}^l{}_3 \cdot \boldsymbol{e}'_2 + \boldsymbol{B}^l{}_1 \cdot \boldsymbol{e}'_2 + \boldsymbol{B}^l{}_2 \cdot \boldsymbol{e}'_2) a_0 \\ \Delta c &= (\boldsymbol{B}^l{}_3 \cdot \boldsymbol{e}'_3 + \boldsymbol{B}^l{}_1 \cdot \boldsymbol{e}'_3 + \boldsymbol{B}^l{}_2 \cdot \boldsymbol{e}'_3) a_0 \end{aligned} \qquad \text{5- 8}$$

which can be written

$$\boldsymbol{d}^{\mathrm{gnd}} = \begin{pmatrix} \boldsymbol{B}^l{}_1 \cdot \boldsymbol{e}'_1 & \boldsymbol{B}^l{}_2 \cdot \boldsymbol{e}'_1 & \boldsymbol{B}^l{}_3 \cdot \boldsymbol{e}'_1 \\ \boldsymbol{B}^l{}_1 \cdot \boldsymbol{e}'_2 & \boldsymbol{B}^l{}_2 \cdot \boldsymbol{e}'_2 & \boldsymbol{B}^l{}_3 \cdot \boldsymbol{e}'_2 \\ \boldsymbol{B}^l{}_1 \cdot \boldsymbol{e}'_3 & \boldsymbol{B}^l{}_2 \cdot \boldsymbol{e}'_3 & \boldsymbol{B}^l{}_3 \cdot \boldsymbol{e}'_3 \end{pmatrix}. \qquad \text{5- 9}$$

An analysis of a mixed edge and screw dislocation segment is presented in Appendix C in order to show the physical explanation for this tensor. In fact, this can be shown to be the Burger's tensor in the undeformed configuration but rotated in to the local undeformed crystallographic configuration, designated (X_c, Y_c, Z_c) shown in Fig. 5-3. Details may be

found in Appendix D. The lattice distortions due to the Burger discontinuity, or equivalently, the development of densities of GNDs become

$$\begin{pmatrix} \Delta a^{\mathrm{gnd}} \\ \Delta b^{\mathrm{gnd}} \\ \Delta c^{\mathrm{gnd}} \end{pmatrix} = \boldsymbol{d}^{\mathrm{gnd}} \begin{pmatrix} a_0 \\ b_0 \\ c_0 \end{pmatrix}. \qquad 5\text{- }10$$

We introduce a lattice distortion gradient, $\boldsymbol{F}^{\mathrm{gnd}}$, such that

$$\boldsymbol{F}^{\mathrm{gnd}} = \boldsymbol{I} + \boldsymbol{d}^{\mathrm{gnd}} = \begin{pmatrix} 1 + \boldsymbol{B}^{l}{}_{1} \cdot \boldsymbol{e}'_1 & \boldsymbol{B}^{l}{}_{2} \cdot \boldsymbol{e}'_1 & \boldsymbol{B}^{l}{}_{3} \cdot \boldsymbol{e}'_1 \\ \boldsymbol{B}^{l}{}_{1} \cdot \boldsymbol{e}'_2 & 1 + \boldsymbol{B}^{l}{}_{2} \cdot \boldsymbol{e}'_2 & \boldsymbol{B}^{l}{}_{3} \cdot \boldsymbol{e}'_2 \\ \boldsymbol{B}^{l}{}_{1} \cdot \boldsymbol{e}'_3 & \boldsymbol{B}^{l}{}_{2} \cdot \boldsymbol{e}'_3 & 1 + \boldsymbol{B}^{l}{}_{3} \cdot \boldsymbol{e}'_3 \end{pmatrix}. \qquad 5\text{- }11$$

Finally, the lattice distortion gradient resulting from the Burger discontinuity with respect to the deformed crystallographic configuration is

$$\boldsymbol{F}^{\mathrm{gnd}\prime} = \Delta \boldsymbol{R}^{\mathrm{c}} \boldsymbol{F}^{\mathrm{gnd}}. \qquad 5\text{- }12$$

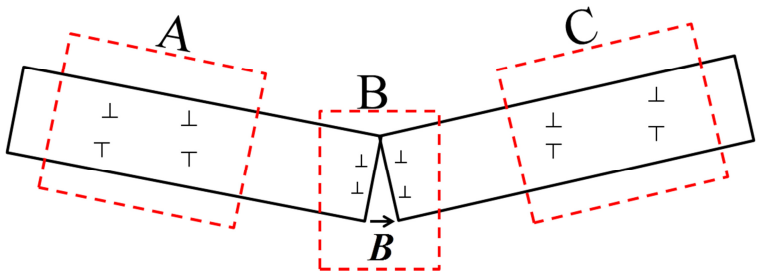


Fig. 5-4: Schematic diagram indicating regions of homogenous lattice deformation (without plastic strain gradients) in A and C, containing statistically stored dislocations and region B in which the plastic strain gradient requires geometrically necessary dislocation content leading to open Burger's circuit ***B***.

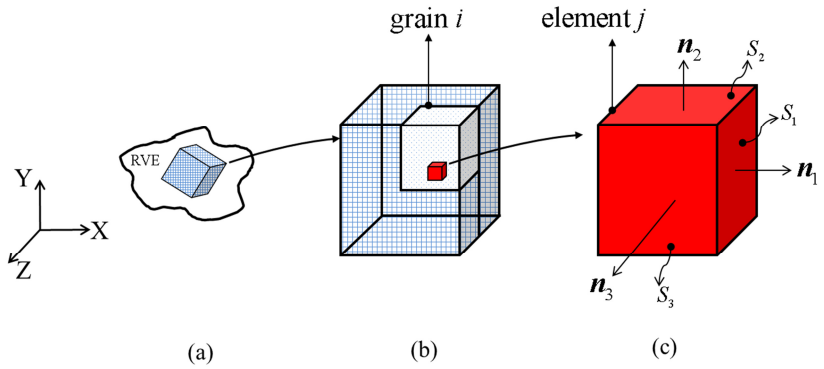


Fig. 5-5: Schematic of RVE discretization to calculate lattice spacing due to GNDs in crystals from crystal plasticity simulations. (a) Representative volume element (RVE) shown schematically within the material, (b) a particular grain (*i*) with given crystallographic orientation within the RVE and (c) for a particular element *j* within grain *i*, the open Burger's circuit is calculated on the orthogonal surfaces S_1, S_2 and S_3 with normal n_1, n_2 and n_3 shown.

5.1.3.Lattice spacing changes due to elastic distortions and GNDs

The deformation tensors resulting from elastic distortions and the Burger discontinuity are calculated in the same reference frame i.e. the deformed crystallographic configuration, so that the total distortional deformation tensor due to elastic distortions and GNDs is calculated according to

$$\boldsymbol{d}^{\mathrm{tot}'} = (\boldsymbol{d}^{e'} + \boldsymbol{d}^{\mathrm{gnd}'}) \qquad 5\text{- }13$$

where $\boldsymbol{d}^{e'} = \boldsymbol{F}^{\mathrm{e}'} - \boldsymbol{I}$ and the total deformation gradient is obtained such that

$$\boldsymbol{F}^{\mathrm{tot}'} = (\boldsymbol{I} + \boldsymbol{d}^{\mathrm{tot}'}) \qquad 5\text{- }14$$

Note that the quantity $\boldsymbol{F}^{\mathrm{tot}'}$ is quite different to the deformation gradient $\boldsymbol{F}$ in Fig. 5-3 since it contains deformation information resulting from elastic straining together with that part of the plastic straining which leads to lattice distortion (ie curvature through the presence of GNDs). Hence, in the absence of plastic strain gradients, $\boldsymbol{F}^{\mathrm{tot}'}$ reduces simply to the (rotated) elastic deformation gradient. Finally, the post deformation lattice lengths due to elastic distortions and GNDs in the deformed crystallographic configuration are given by

$$\frac{a'_{\mathrm{tot}}}{a_0} = \left|\boldsymbol{F}^{\mathrm{tot}'}\boldsymbol{e}_1^{\mathrm{c}}\right|, \frac{b'_{tot}}{b_0} = \left|\boldsymbol{F}^{\mathrm{tot}'}\boldsymbol{e}_2^{\mathrm{c}}\right|, \frac{c'_{\mathrm{tot}}}{c_0} = \left|\boldsymbol{F}^{\mathrm{tot}'}\boldsymbol{e}_3^{\mathrm{c}}\right| . \qquad 5\text{- }15$$

5.2. Validation of methodology

A series of validations for the methodologies described in the previous sections are presented, firstly for the elastic distortions and subsequently for the lattice spacing changes resulting from the Burger discontinuity (or equivalently the development of GND densities).

5.2.1.Elastic distortions

Lattice spacing distributions in a single crystal subject to uniaxial straining

Consider a single crystal in the reference configuration shown in Fig. 5-6a subjected to uniaxial stretch. The boundary conditions are such that the negative X-, Y- and Z- surfaces are constrained not to move in their respective directions whilst the positive X- and Z- surfaces are unconstrained. Displacement U_y is applied in the positive Y- direction and isotropic elasticity is assumed. The 3-D finite element model is shown in Fig. 5-6b and Fig. 5-6c shows a schematic of the lattice spacing between consecutive (100) and (010) planes in the undeformed state represented by d^0_{100} and d^0_{010} respectively. By applying displacement U_y in the [010] direction, the lattice spacing between successive (010) planes increases, however, due to isotropic elasticity, the spacing between consecutive (100) and (001) planes reduces as illustrated schematically in Fig. 5-6d.

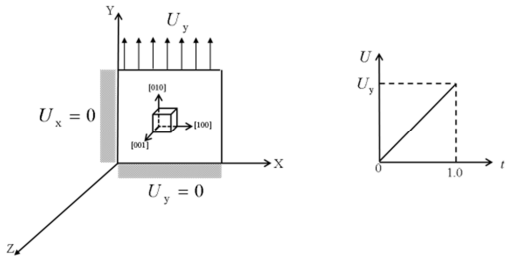
The discussion on the {100} family of planes can be similarly applied to the {110} set of planes as shown in Fig. 5-7b. In this case, by subjecting the crystal in Fig. 5-6di to uniaxial stretch in the [010] direction, the spacing between consecutive (101) planes reduces whilst the spacing between consecutive (011) and (110) planes increase as seen in Fig. 5-7b. Also, the deviation of the (101) plane from the ideal lattice spacing d^0_{110} is proportional to the deviation of the (011) and (110) planes given by Poisson's ratio.

Lattice spacing distributions due to 2-D spatial dislocation field

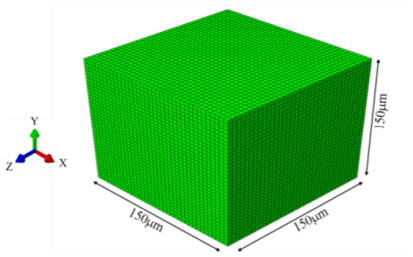
Fig. 5-8 shows the σ_{xx} component of a 2-D spatial field comprising edge dislocations each of a constant total density. Figs. 5-8a-c shows the three configurations examined. In the cases considered, the local distribution of edge dislocations varies; however, the same total density of edge dislocations $\boldsymbol{\rho}_T$ within the spatial field is maintained (see Appendix E for details).

With knowledge of the 2D displacement fields generated by the differing dislocation contents, the lattice distortions have been determined using the model presented above. The resulting calculated distributions of lattice spacings for the (100), (111) and (110) planes are shown in Fig. 5-9. The width of distribution of lattice strains in the {100} family of planes is greater than that seen in the {111} and {110} planes, and the resultant lattice spacing distribution is independent of the distribution of dislocations in the crystal since the net dislocation content is the same for all cases (a), (b) and (c) in Fig. 5-8. The small differences seen in the lattice spacing distributions are due to edge effects associated with the 2-D spatial field. Thus, if the dislocations were to be modelled in an infinitely large field, the small differences would vanish.

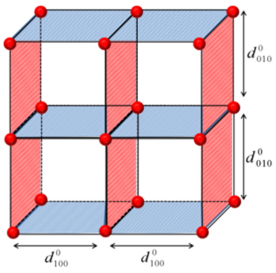
(a)



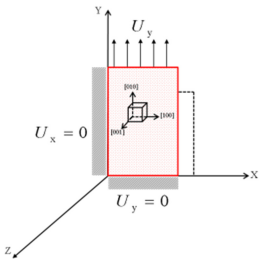
(b)



(c)



(di)



(dii)

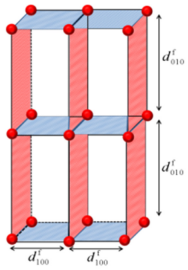


Fig. 5-6: Schematic diagram of a single crystal (a) whose [100], [010] and [001] direction coincide with the XYZ system shown subject to uniaxial straining in the Y-direction, modelled using crystal plasticity with computational finite element mesh shown in (b). An undeformed lattice is shown in (c) with the undeformed lattice spacing indicated for the (100) and (010) planes denoted by $d^0_{100}$and d^0_{010} respectively. The lattice is subject to uniaxiual straining as shown in (di) and the post deformation lattice spacing for the (100) and (010) planes are shown in (dii) denoted by d^{f}_{100} and d^{f}_{010} respectively.

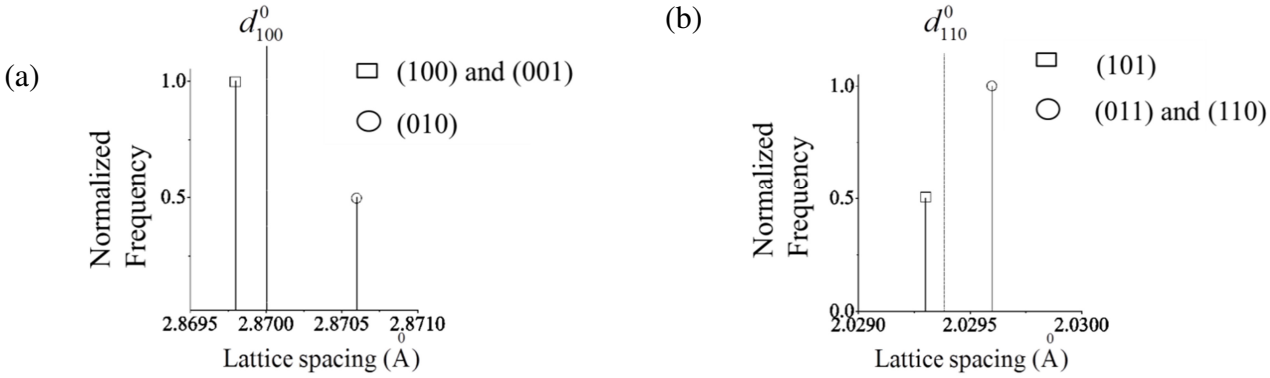


Fig. 5-7: Lattice spacing for the single cubic crystal shown in Fig. 8 (c) and (d) subject to uniaxial Y-direction straining indicating the initial spacing (d^0) and spacing after deformation for (a) the {100} and (b) {110} planes.

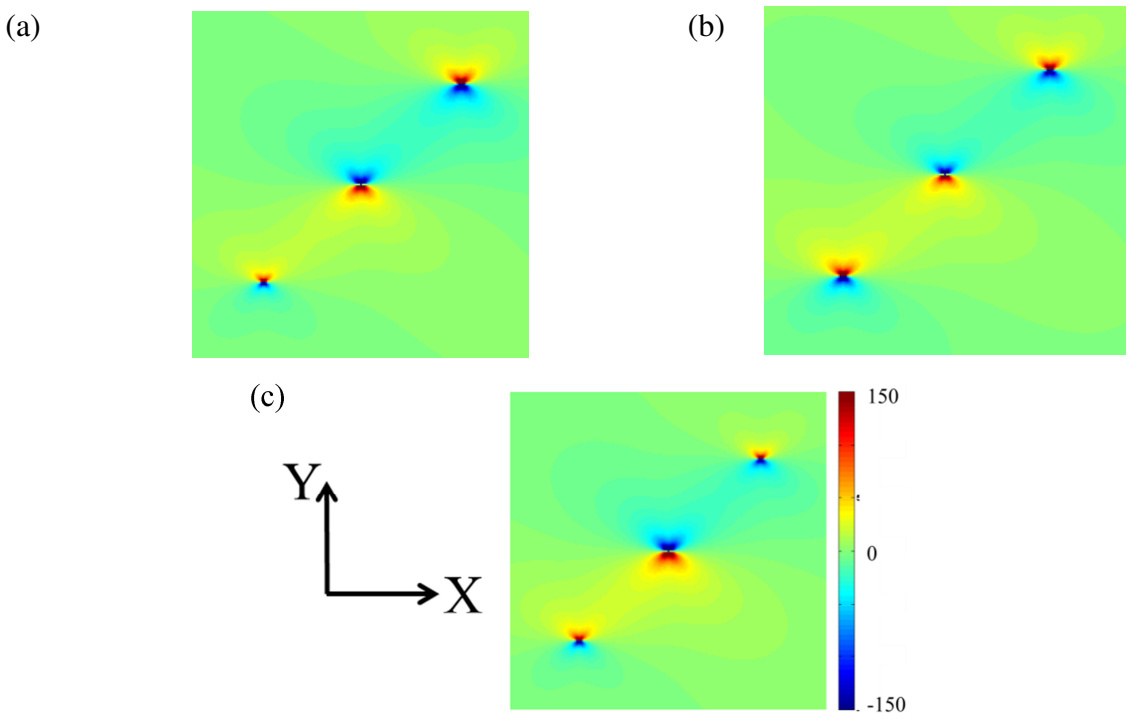


Fig. 5-8: Stress fields (σ_{xx} component) for edge dislocations in a 2-D spatial field. In each configuration, a varying local distribution of edge dislocation exists however, the total density of edge dislocations ρ_{T} remains constant. (a) $\rho_{\mathrm{T_A}}$(b) $\rho_{\mathrm{T_B}}$ and (c) $\rho_{\mathrm{T_C}}$.

5.2.2.Burger discontinuity and GND density

Determination of Burger discontinuity and GND density and comparison with electron back-scattered diffraction (EBSD) data

The Burger discontinuity and hence GND density are determined from knowledge of measured elastic strain fields using the L^1 minimization scheme and compared against an independent calculation [64] in order to validate the finite element methodology presented for determination of the Burger discontinuity described in Appendix B. The method was applied to determine the GND density from experimentally obtained EBSD data for a hexagonal close packed (HCP) tri-crystal. The GND density of the tri-grain titanium sample with twinning formed at the intersection of grains was measured by Britton, T.B. [64] using EBSD. They predict a high concentration of GNDs especially at the intersection of the twins in Fig. 5-10a.

Using the same EBSD data, the GND density map was determined and is shown in Fig. 5-10b. The observed differences are attributed to the improved (higher-order) strain gradient approach adopted here and described in Appendix B. Britton, T.B [64] used a linear fit to a plane of nine neighboring elements, whereas the approximation technique here adopts a piecewise higher order polynomial representation.

Burger discontinuity and GND density in a single crystal beam subjected to four-point bending

Four-point beam bending generates a state of pure bending within a section of the beam, thereby developing a simple strain gradient with which the Burger discontinuity and GND density calculations may be verified. In addition, by progressively applying displacement-controlled loading, elastic and elastic-plastic deformation may be developed thus enabling the

progressive interpretation of the lattice spacing distributions prior to yield, and at larger plastic strains for which the elastic straining becomes relatively small.

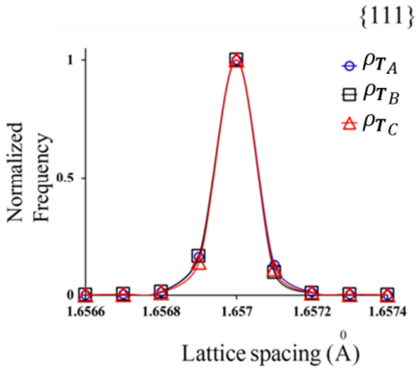
In Fig. 5-11a, an FCC single crystal beam of dimensions $20 \times 20 \times 200\mu m$ was subjected to four point bending as shown schematically. The beam, made up of 80,000 ABAQUS explicit C3D8R linear elements with reduced integration, was displaced downwards by U_y under displacement control at $l/3$ and $2l/3$ and fixed at $l=0$ and l where l is the length of the beam. The beam was constrained in the Z- direction to ensure plane strain conditions, and isotropic hardening was assumed on all slip systems. The crystal plasticity formulation is described in chapter 2 and material properties are shown in Table 3-1. Note that τ_0 in this example is 30MPa. All elements in the beam are assigned the crystallographic reference configuration such that the [100], [010] and [001] directions coincide with the XYZ frame shown in Fig. 5-11a. The peak plastic strain developed in the bending region is about 1.0% and varies linearly along the section of the beam as seen in Fig. 5-11b. The consequence is a constant density of GNDs expected in this region as shown in Fig. 5-11c. Lattice spacing distributions are addressed in the next section.

5.3. Lattice spacing distributions due to elastic distortions and development of GNDs

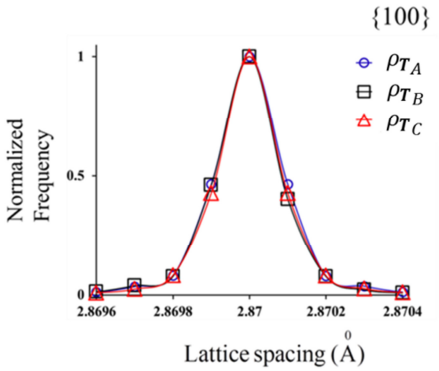
Lattice spacing distribution is investigated for the single crystal beam subjected to four-point bending described in section 5.2 and for a polycrystal subjected to uniaxial strain. The aim is to quantify and compare the development of the distributions resulting from elastic distortions, GND density evolution and the two combined. The distributions of lattice spacings obtained due to elastic distortions (denoted ED) are obtained by calculating the

deformation gradient due to the elastic strains developed. GND density development, as a consequence of Burger discontinuity, affect lattice curvatures and hence, also affect lattice spacing changes which are obtained by determining the deformation gradient developed due to plastic strain gradients (denoted GND). Finally, the net effect of the contributions to lattice spacing distributions from the two mechanisms combined (denoted ED+GND) is obtained by evaluating the total deformation gradient resulting from both elastic distortions and Burger discontinuities. The peak width at half maximum (FWHM) for each distribution, ED, GND and ED+GND respectively, is calculated from the lattice spacing distributions. As stated before, the FWHM determined in this way differs from that obtained from experimental x-ray diffraction measurements, though it is anticipated to be indicative of experimentally determined diffraction peak broadening.

(a)



(b)



(c)

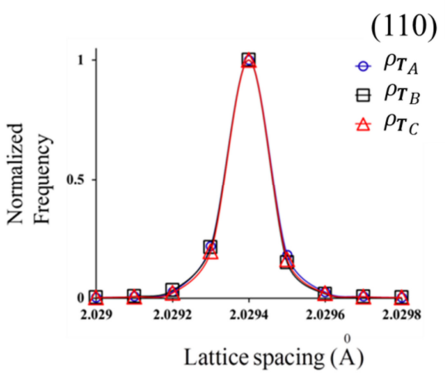


Fig. 5-9: Lattice spacing peaks determined from the strain field corresponding to the dislocation distributions shown in Fig. 10 for the (a) (111) (b) (100) and (c) (110) planes respectively, showing independence from the dislocation distribution.

5.3.1. Analysis of single crystal FCC beam subject to four-point bending

The FCC single crystal beam subjected to four-point bending is further analyzed in this section. A systematic study on the lattice spacing distributions due to elastic distortions and GND development is presented and an assessment made of the relative contribution to the total lattice spacing, and the width of the peaks formed (FWHM).

The current study lies within the context of previous studies on lattice strain distributions such as Kanjarla et al. [65], Neil et al. [66], Dawson et. al [67]. Whilst [67] adopts a finite element framework, [66] and [65] employs a self-consistent model. They argue that diffraction in materials is an average ensemble making their approach adequate in capturing the evolution of lattice strains. Of particular interest is the study on the evolution of internal lattice strain distributions and their effect on peak broadening by Kanjarla et al. [65]. They concluded that peak broadening is underestimated by considering elastic distortions only. This was emphasized in their investigations on a polycrystal subjected to uniaxial straining wherein peak broadening predictions using only lattice strains provided a significant underestimation in comparison to experiments and the difference was anticipated to result from missing strain gradient contributions. In the light of their work, lattice strain distributions due to elastic distortions and GND development are discussed for increasing deformation levels in a single crystal FCC beam subjected to four-point bending.

Fig. 5-12 shows the lattice spacing distribution for a single crystal beam subjected to four-point bending described in section 5.2.2. Three levels of deformation are shown for the (111), (100) and (110) planes and the lattice spacing distributions due to elastic distortions (ED),

GNDs (GND) and the two combined (ED+GND) are compared in all cases. The three levels of applied deformation are chosen such that at 0.04% strain, the beam is fully elastic whilst at 1% and 3% strain, significant plasticity is occurring. Note that the strains specified are the peak strain values in the pure bending region at the top and bottom of the beam shown in Fig. 5-11(a). Also, note that in the single crystal beam, the mesh dependent length, $L = 1\mu m$ is used to calculate the normalized Burger's vector discontinuity.

Fig. 5-12a shows the response of the (111) plane to elastic distortions, GND development and the two combined, respectively. Fig. 5-12ai shows that whilst the lattice strain distribution due to elastic distortions (ED) is finite at 0.04%, it remains largely unchanged for higher strains since once yield has been achieved, the strain increase is largely plasticity driven. For a strain of 0.04%, for which the deformation mode is solely elastic, Fig. 5-12aii shows that there is no contribution to the peak from GND development since there is no plasticity. For higher strains, however, for which plasticity is occurring, peak broadening is seen to occur with increasing plastic strain. The total lattice spacing distribution due to elastic distortions and GND development is shown in Fig. 5-12aiii and the overall distribution is broader at all strain levels shown in comparison to individual elastic or GND components i.e. ED or GND. The symmetry associated with the lattice spacing distributions results from the beam symmetry about the neutral axes of the single crystal such that no peak shift occurs in this configuration.

Figs. 5-12b and 5-12c represent the response of the (110) and (100) planes respectively in the beam subjected to four-point bending. The peaks resulting from consideration of elastic distortions only for both planes show little change after a strain of 0.04% because of the onset

of plasticity. Also, the widths of the lattice spacing distributions due to GND development alone increases systematically with strain for both planes and hence contributes to broadening when both mechanisms are combined in Figs. 5-12biii and 5-12ciii. Of particular note is the significant broadening seen due to elastic distortions on the (100) plane in Fig. 5-12ai.

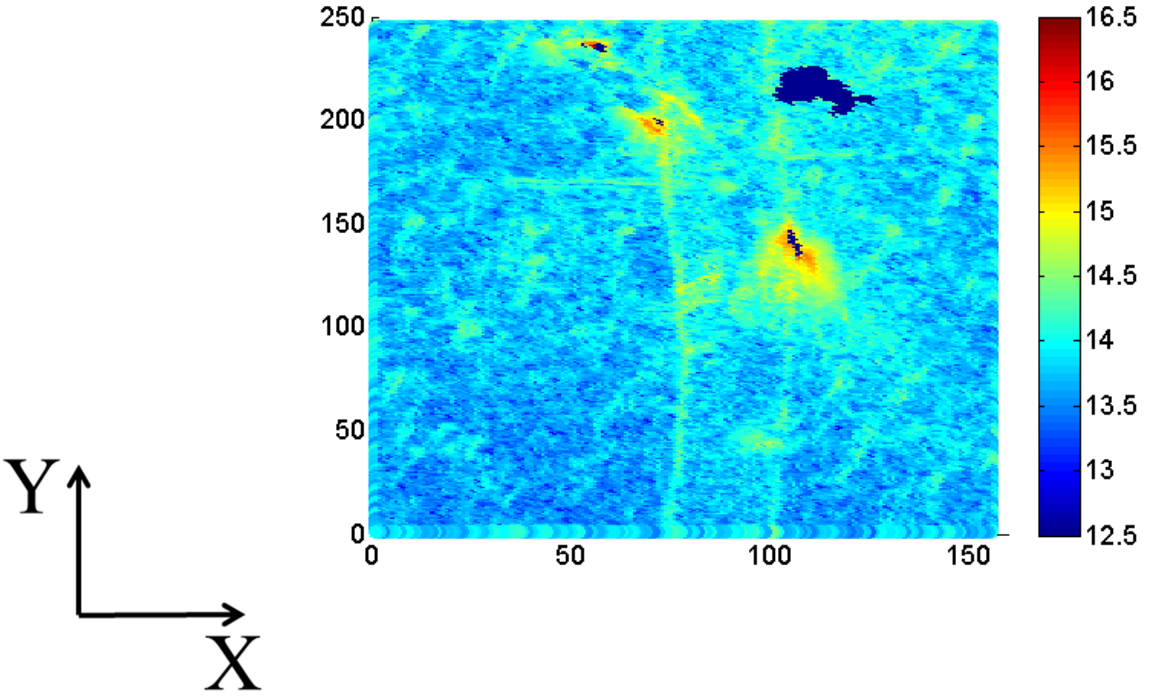
Fig. 5-13 shows a schematic diagram illustrating the lattice spacing changes on the (100) plane in the single crystal FCC beam subjected to four-point bending. Consider the pure bending region further expanded to show the line of symmetry about which bending occurs on the (100) plane, denoted as d_{100}^{0}. By displacing the beam downwards, the region above the neutral axis is in compression whilst the region below it is in tension. Considering a small deviation from neutral axis, the lattice spacing for the region in tension increases to $d_{100}^{0}+\Delta d_1$ and conversely, the lattice spacing for the equivalent region in compression decreases to $d_{100}^{0}-\Delta d_1$. Because of the symmetry about the neutral axis, the lattice spacing frequency is expected to take the form illustrated in Fig. 5-13b where the deviations from the ideal spacing, denoted by d_{100}^{0}, is indicated. Since the frequency is equal in all cases, the observed responses seen in Figs. 5-12bi and 5-12ci are compatible with this interpretation. The variation of the peak FWHM is shown in Fig. 5-14 for the single crystal beam subjected to four-point bending and provides a better indication of the peak width due to elastic distortions, GND development and the two combined. Here, a systematic increase in strain level from 0.01% up to 5.0% is shown resulting in purely elastic deformation for small strain through to the onset of slip and bulk plasticity at the higher strains. Fig. 5-14a shows the width of the lattice spacing distributions shown previously in Fig. 5-13 for the (100) plane and it is seen that the width of the distribution due to elastic strains increases until the onset of

yield, and thereafter remains largely constant. However, at the yield point, the contribution of GND development becomes finite due to the establishment of plastic strain gradients within the single crystal beam, and increases progressively. A similar trend is observed in the (110) and the (111) planes, with the (100) plane showing the highest levels of broadening compared to the (110) and (111) planes.

Length scale effects were also investigated in the single crystal beam shown in Fig. 5-11a using the crystal plasticity approach adopted in this chapter. The gradient formulation presented for GNDs enables the effect of length scale to be captured in the analysis such that smaller beams are expected to give higher GND densities for given straining and hence greater distortional lattice spacings. Three beam sizes are considered ($10 \times 10 \times 100$; $20 \times 20 \times 200$; and $30 \times 30 \times 300 \mu m^3$ respectively) and are subjected to 3% peak strains. Fig. 5-15 shows the lattice strain distributions due to the development of GNDs for the three beam sizes.

Consider the (100) plane shown in Fig. 5-15a. Increased peak broadening is observed with decreasing beam size as expected. Typically, higher strain gradients are formed with decreasing size and this results in larger lattice spacing in the example considered. Similar behaviour is seen in the (110) and (111) planes.

(a)



(b)

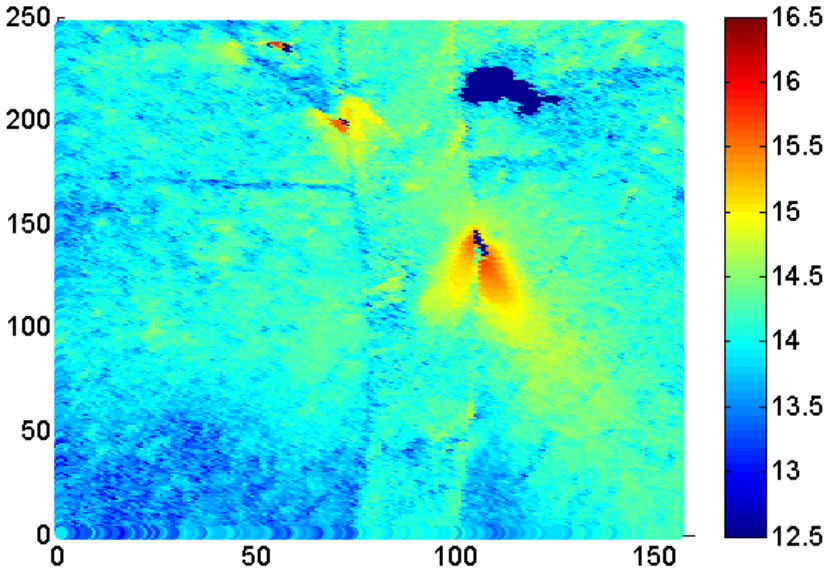


Fig. 5-10: (a) GND density distribution in a Ti- tri-crystal determined by Britton, T.B. [64] and (b) that calculated using the technique used in this chapter from knowledge of the corresponding experimentally measured displacements. GND density is shown in Log_{10} (m^{-2}).

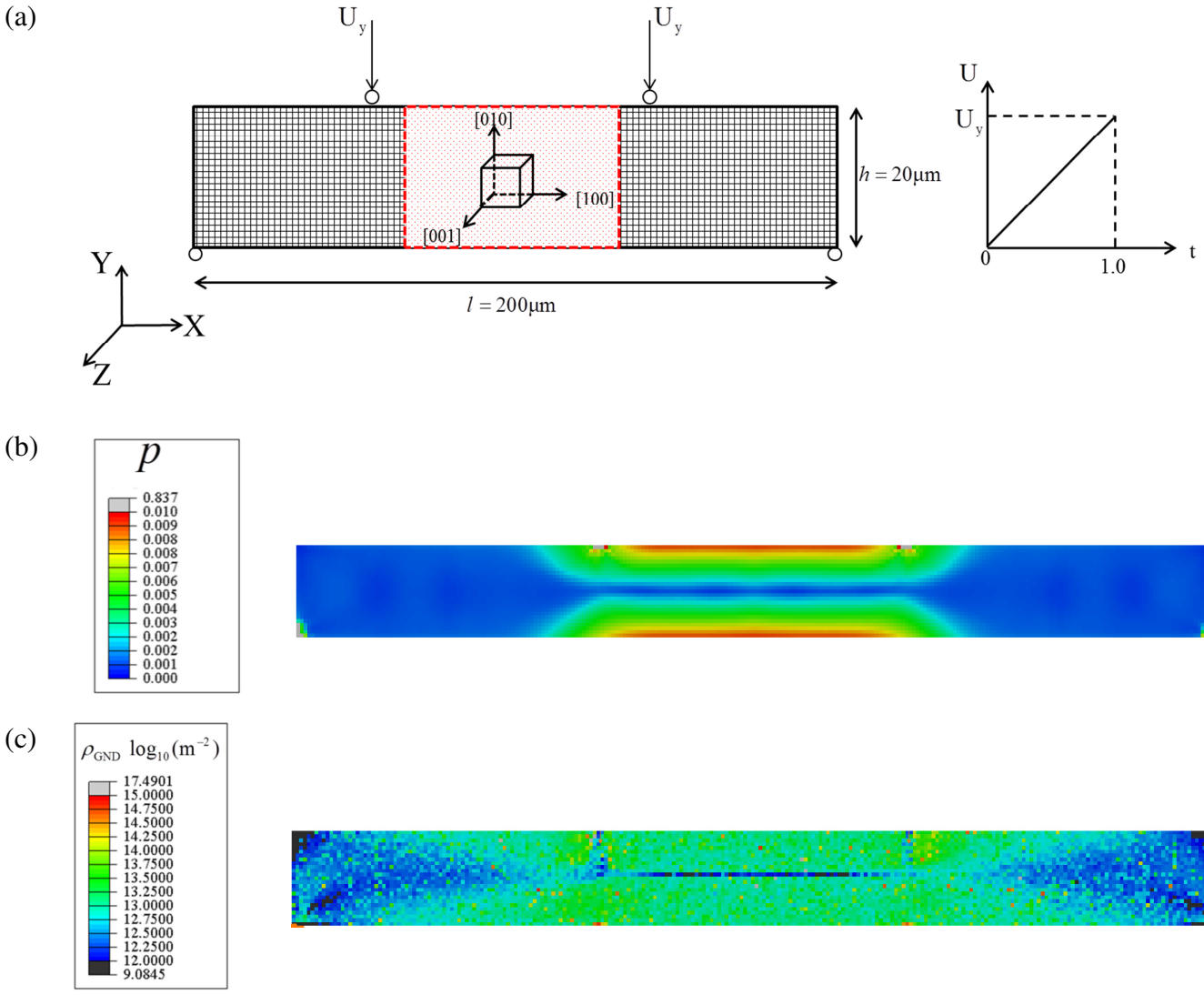


Fig. 5-11: Schematic diagram (a) of a single crystal beam ($10 \times 10 \times 100$; $20 \times 20 \times 2000 \times 30 \times 300 \mu m^3$) subjected to four-point displacement loading leading to (b) the progressive development of a linearly varying (Y-direction) plastic strain and (c) a representative distribution of GND density.

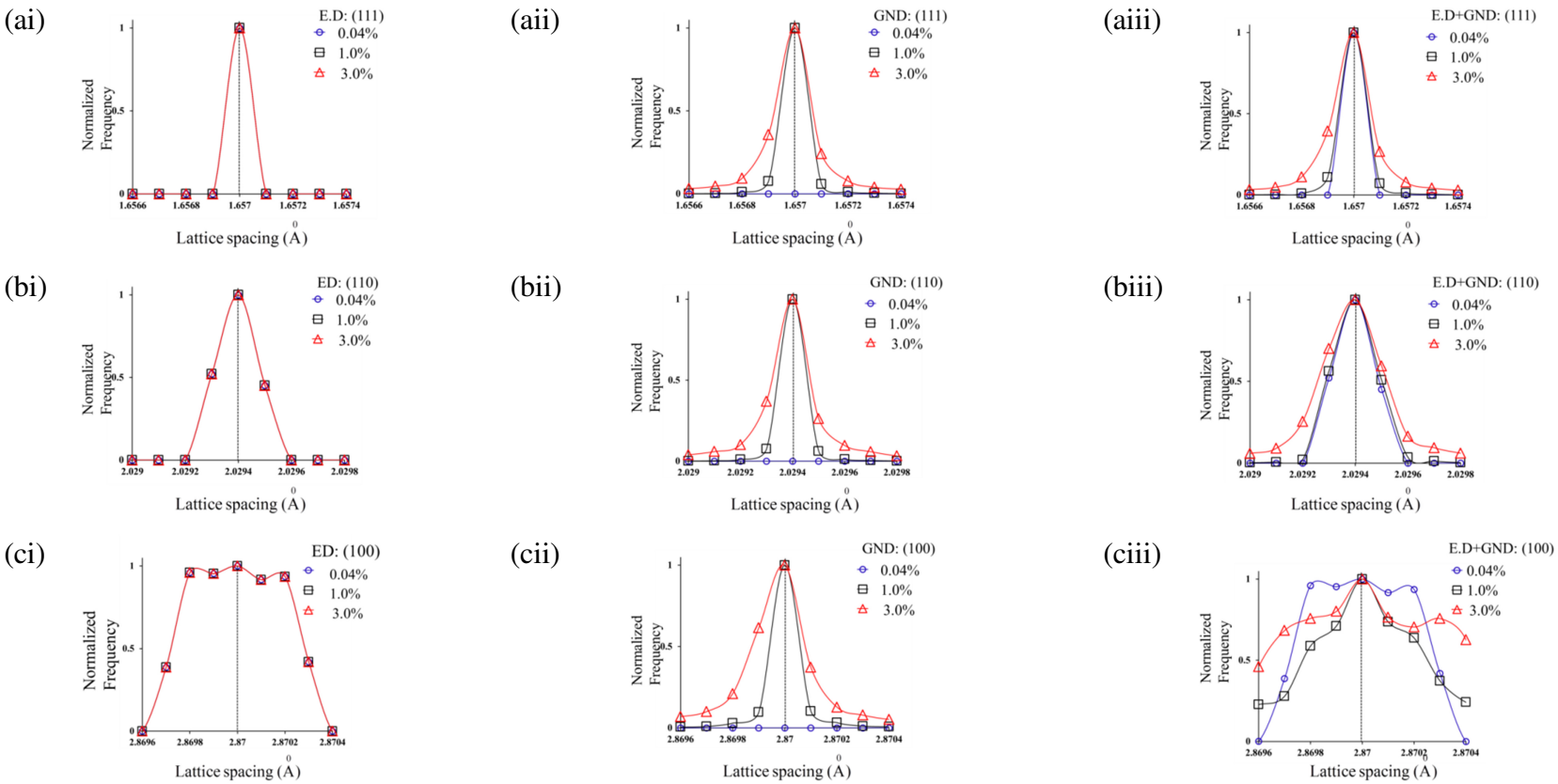


Fig. 5-12: Lattice spacing distributions due to (i) elastic distortions (ED), (ii) the development of GNDs (GND) and (iii) the two combined (ED+GND) in the single crystal beam shown in Fig. 5-12a subject to four-point bending for the (a) (111), (b) (110), and (c) (100) planes respectively for the applied (peak) strains shown.

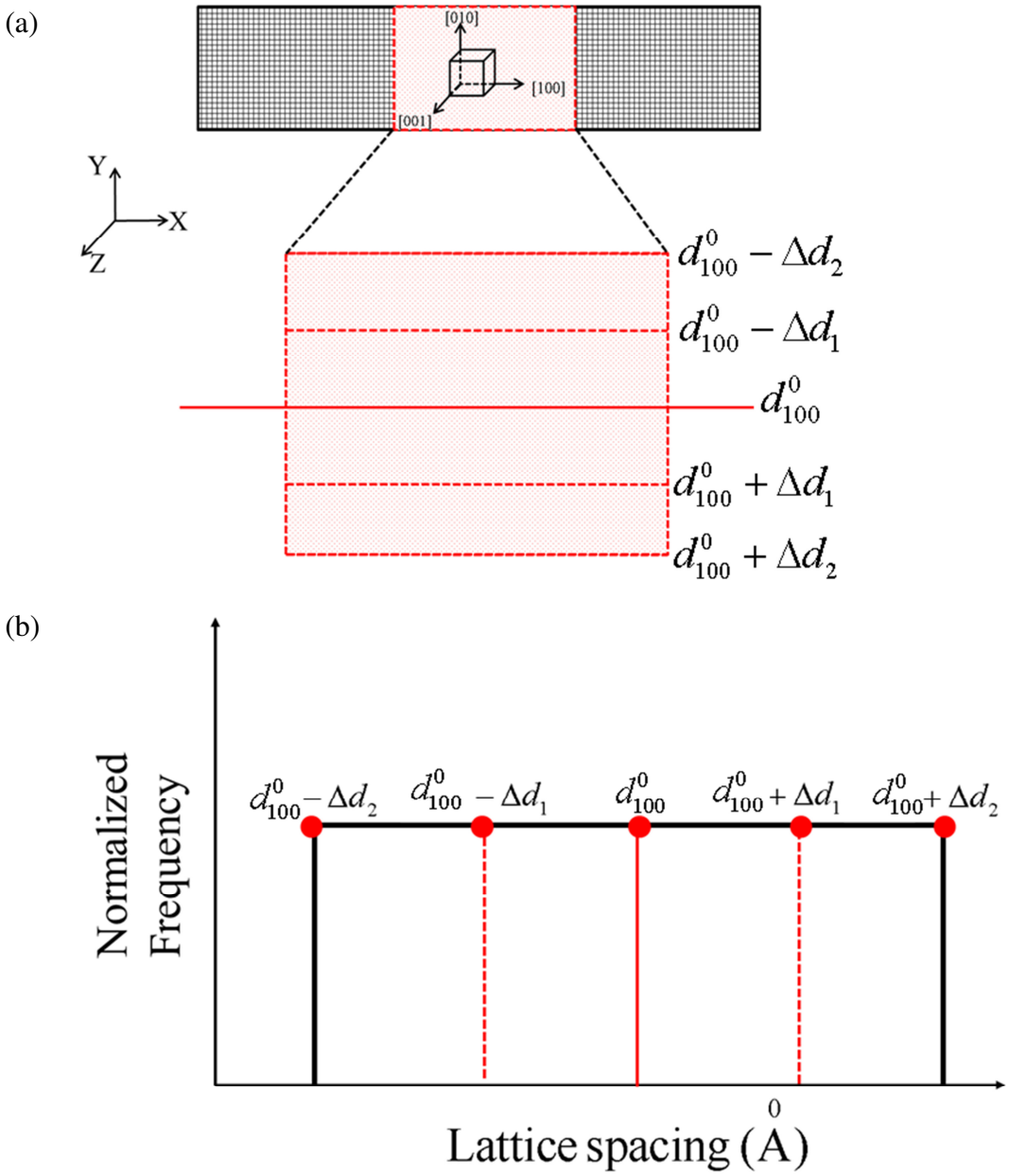


Fig. 5-13: Schematic diagram illustrating the lattice spacing response of the (100) plane in a beam subject to four-point bending as a function of frequency. The region of pure bending is illustrated in (a) and the response of the (100) plane is illustrated in (b).

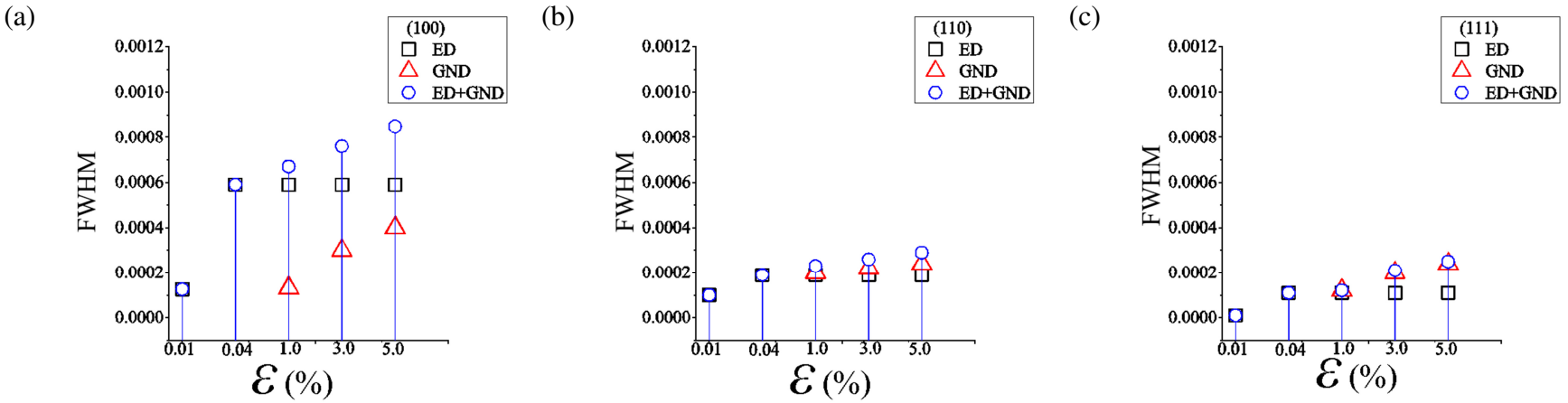
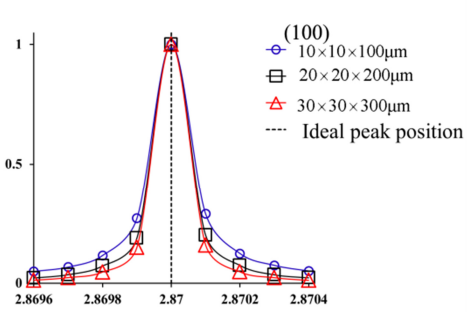
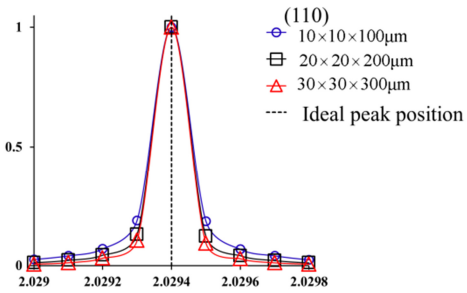


Fig. 5-14: Lattice spacing peak width (FWHM) due to elastic distortions (ED), the development of GNDs (GND), and the two combined (ED+GND) in the single crystal beam show in in Fig. 5-12 subject to four-point bending for the (100), (110) and (111) planes respectively for applied (peak) strains up to 5%.

(a)



(b)



(c)

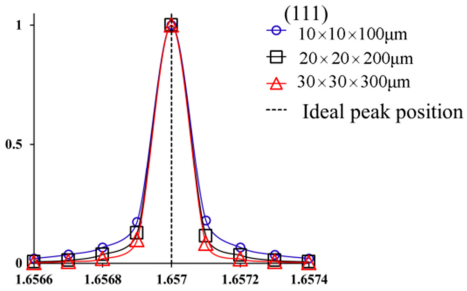


Fig. 5-15: Lattice spacing distributions due to the development of GNDs for three single crystal beams of varying sizes, (see Fig. 5-12a). The (a) (100), (b) (110), and (c) (111) planes respectively for a peak strain of 3%. The broken line indicates the ideal peak position of that particular plane in an unstrained crystal.

5.3.2. Analysis of random and textured FCC polycrystals subject to uniaxial straining

A systematic study of the lattice spacing distributions due to elastic distortions and GND development is presented for a polycrystal subjected to uniaxial straining. A polycrystal with no texture (ie nominally random) and a representative textured polycrystal are both addressed, and comparisons are drawn with previous studies by Kanjarla et. al [65] and Dawson et. al [67] who have assessed the elastic distortion contributions to peak broadening in their models.

The polycrystal analysed has 216 grains denoted by the shaded regions in Fig. 5-16a and has macro texture represented by the orientation distribution functions shown in Figs. 5-16b and 5-16c adopted to give a representative behavior of initially random and textured polycrystals.

The polycrystal was subjected to 5% uniaxial straining in the positive Y- direction, and the negative X-, Y- and Z- surfaces are constrained not to move in their respective directions and the positive Y- and Z- surfaces are constrained to remain planar. The simulation was carried out using C3D8R ABAQUS explicit linear elements and each grain denoted by the shaded regions in Fig. 5-16a consists of 6×6×6 elements.

As a result, the mesh dependent Burger's vector normalization length, $L = 4.167\mu m$ is employed in the analyses. This discretization was chosen based on a mesh sensitivity study carried out and shown in Fig. 5-17. The macro-level average stress versus strain given as a function of mesh size in Fig. 5-17a shows limited mesh sensitivity, but the plastic strain gradient at a single point in the polycrystal shows a considerable change resulting from the

change in discretization (Fig. 5-18b). For this reason, the mesh discretization of 6×6×6 elements per grain is chosen.

Four levels of uniaxial strain are investigated for both the initially random and textured polycrystals. Consider first the lattice spacing distribution for favourably oriented {100}, {110} and {111} planes for the initially random polycrystal, denoted T-1, shown in Fig. 5-18a. It is apparent in all planes considered that the peak width due to elastic distortions remains largely constant after yield and at a strain of about 0.04%, whilst the lattice spacing distribution due to contributions from GND development increases with strain. Also, the {100} plane shows significant increases in peak width consistent with that reported by Kanjarla et. al [65]. However, in their work, this was attributed to the elastic compliance associated with the {100} plane in comparison to the {110} and {111} planes.

The textured polycrystal subject to the same strain controlled loading is considered next and the peak widths of the calculated lattice spacing distributions for this case, denoted T-2, are shown in Fig. 5-18b. Similarly to the initially random polycrystal, the peak width due to elastic distortions remains largely constant as plasticity proceeds, whereas the contribution from GND development increases progressively for all planes considered. The increase is most significant on the {100} plane similar to the initially random polycrystal. By comparing corresponding planes in both the random and textured polycrystals, the peak width in the initially textured polycrystal T-2 is generally smaller than that for the randomly orientated polycrystal. This is likely because the initially random texture, T-1 generates more heterogeneity than the textured polycrystal T-2. The analyses for both polycrystals indicate that the development of GNDs contributes significantly to peak broadening and that in fact,

that due to the elastic distortions becomes rather small at strains for which there is significant plasticity. It is therefore expected that experimentally measured peak broadening using x-ray diffraction would similarly contain strong influence from the establishment of lattice curvature due to GND development.

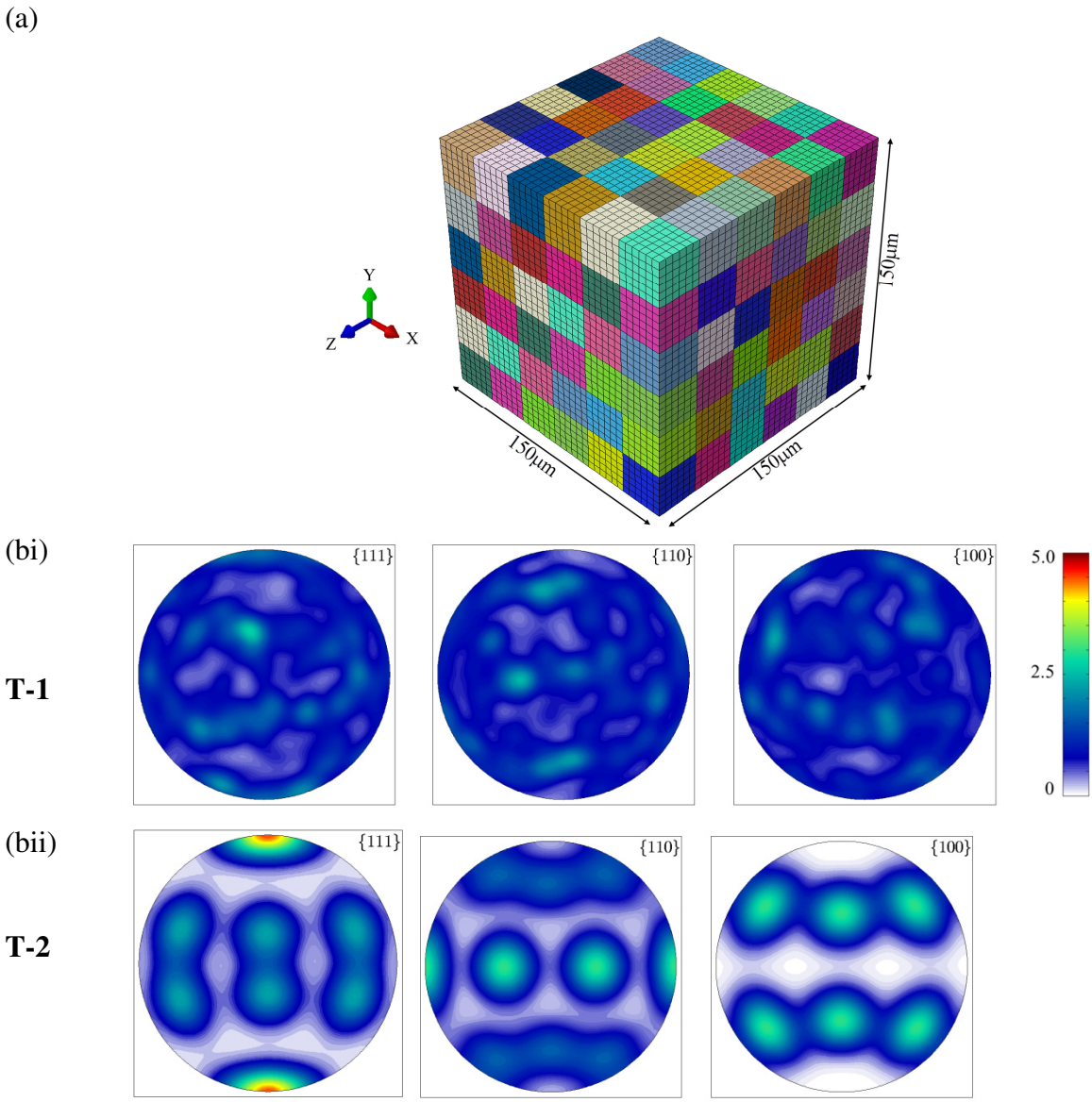
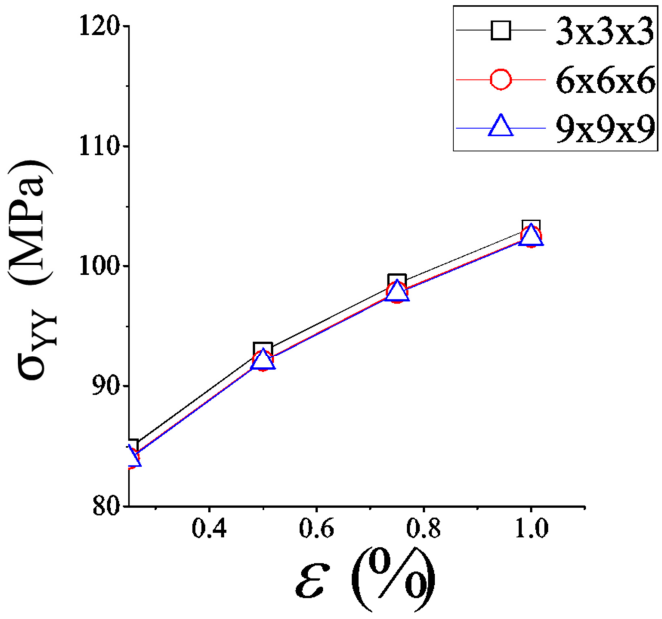


Fig. 5-16: (a) Example 216 grain polycrystal, each grain discretized using 216 elements with crystallographic orientations assigned in order to represent (bi) random and (bii) textured polycrystals.

(a)



(b)

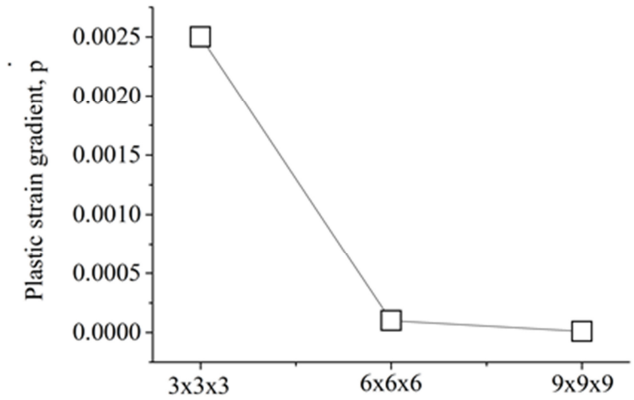
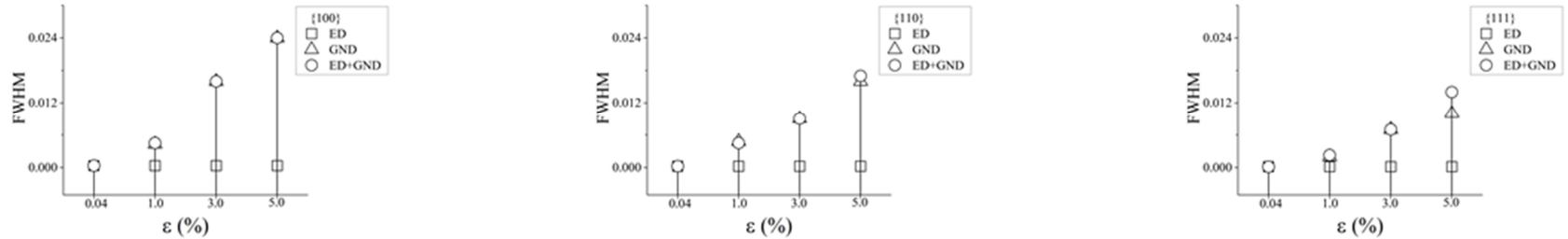
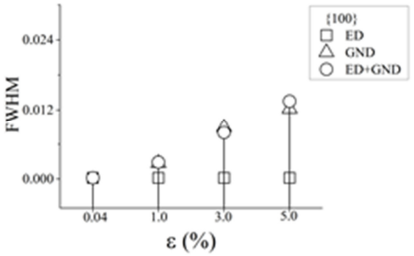


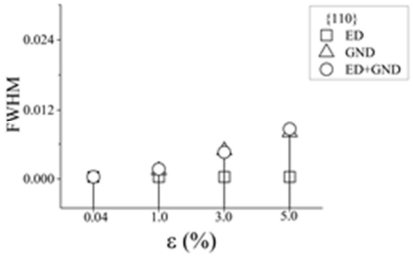
Fig. 5-17: Mesh sensitivity study carried out on the model polycrystal shown in Fig. 5-16 showing (a) the Y direction macroscopic uniaxial stress-strain response for the number of elements per grain shown, and (b) Change in plastic strain at an identical point in the mesh calculated using the non-local approach presented in appendix B for different mesh configurations.

(ai) (aii) (aiii)



(bi) (bii) (ciii)





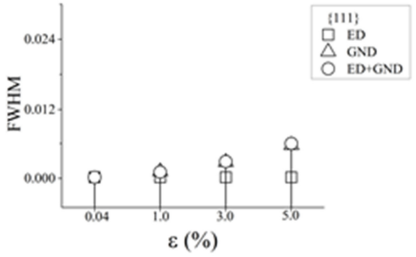


Fig. 5-18: Lattice spacing peak widths for the polycrystal shown in Fig. 5-16 subject to uniaxial Y-direction straining for the {100}, {110}and {111} planes for increasing strains for (a) the random textured polycrystal and (b) the textured polycrystal (for which the pole figures are shown in Fig. 5-16).

5.4. Conclusions

Lattice spacing distributions due to elastic distortions and GND development have been investigated within a crystal plasticity finite element framework. The deformation gradients at the crystal level due to elastic distortions and the distortions resulting from the Burger discontinuity and hence GND development has been addressed. A number of validations for the technique are presented and evaluated. Knowledge of the relevant deformation gradients and their spatial variations has provided a methodology to determine lattice spacing distributions, and their corresponding peak widths, resulting from the contributions of elastic distortions and lattice curvatures giving rise to GND density development. Hence an assessment of the relative contributions to peak broadening of the two independent mechanisms has been presented.

Studies of an FCC single crystal beam subjected to four-point bending show that once slip has been initiated and where plastic strain gradients exist, the Burger discontinuity giving rise to the development of GND densities contributes to peak broadening and that the contribution from elastic distortions then remains largely unchanged with increasing applied straining. For moderate strains (~1%), the GND contribution to peak widths is relatively small but increases significantly with larger strains (~5%) such that the overall peak width is then dominated by the GND contribution.

Studies of random and textured polycrystals subjected to uniaxial (100) straining, however, showed that the peak widths became dominated by GND contributions at lower strains (~1%) which it is argued results from the much great heterogeneity present in both random and textured polycrystals in comparison to single crystal deformation. However, the random polycrystal was found to lead to higher peak broadening relative to the textured polycrystal,

particularly for the (100) planes, similarly because the random crystal orientations lead to increased heterogeneity in strain relative to the textured polycrystal.

It is worth pointing out that the lattice spacing distributions calculated here are not equivalent to that obtained from x-ray diffraction however, the ability to obtain the total lattice deformation due to both elastic distortion and GNDs will feed into the study presented in the next chapter which attempts to directly relate experimental lattice spacing measurements with crystal plasticity calculations.

Chapter VI

6. Role of Texture and Hardening on simulated x-ray diffraction lattice strain measurements under non-proportional strain paths using crystal plasticity

A framework to link x-ray diffraction lattice strain measurements with crystal plasticity finite element analyses is presented. The goal is to understand the evolution of lattice strains for differing deformation histories which is potentially useful in material manufacturing design processes. Further, lattice spacing developed under differing strain paths will provide understanding of why particular strain paths are beneficial in comparison with others. The X-ray modelling technique is described next. Subsequently, an understanding of the method is presented for a single crystal followed by a range of polycrystal textures under both proportional and non-proportional strain paths. Finally, the lattice spacing distributions for the range of strain paths are then evaluated to determine the consequence on ductility.

6.1. X-ray diffraction modelling

This section provides a description of the x-ray diffraction methodology. First, a summary of the experimental x-ray diffraction process is presented followed by the computational methodology used to calculate equivalent diffraction patterns within a crystal plasticity framework.

Fig. 2-8 provided a schematic of the experimental x-ray diffraction set-up used in this study. It shows an x-ray incident on a deforming sample. The x-ray beams interact with the sample within a diffraction volume and are diffracted by planes that satisfy Bragg's condition leading to the Debye Scherrer rings recorded as intensities at the detector shown in Fig. 2-8. In any diffraction experiment, a reference sample which has zero deformation state is required. Hence an undeformed sample of ferritic steel was used to obtain the reference image. Next,

the deformed samples are then subjected to the same process in order to obtain the Debye Scherrer ring corresponding to that macroscopically deformed state. The result for each deformed state is a series of rings corresponding to each diffracting plane family i.e. {110}, {200}, {310} etc as illustrated in Fig. 6-1a. For simplicity, consider the {310} family shown in Fig. 6-1b. In the undeformed state, the resulting Debye Scherrer ring has a uniform radius; however, upon (eg) uniaxial deformation, the radius of this ring changes, becoming more ellipsoidal in a particular direction depending on the crystallographic orientation (texture) of the sample relative to the loading direction. Further, the intensity of the diffracted beam varies about the Debye Scherrer ring.

The measured strains are elastic and very small and the changes in radius are calculated using image processing. Consecutive diffraction rings are compared to evaluate differences in radius as well as intensity for azimuthal sectors (illustrated in Fig. 6-1b) about the ring and then mapped to the overall macroscopic applied strain in order to obtain the evolution of elastic strains over the whole deformation history. Fig. 6-1b shows a schematic of azimuthal sectors such that all diffracting beam intensities which fall within the highlighted sector in the series of diffraction images are binned. The intensities within this sector are integrated and converted to a 2θ against intensity plot. Note that 2θ represents the Bragg angle denoted in Eq. 2-2 and is measured experimentally. Next, the 2θ-intensity distribution is converted into lattice spacing against intensity using Eq. 2-2 with knowledge of the x-ray wavelength. The peak centre is then calculated in order to obtain the average lattice spacing for that particular azimuthal sector.

This image processing methodology is first carried out about the diffraction ring of the unstrained sample in order to obtain the reference lattice spacing, d_0^j for each azimuthal sector. Subsequently, the process is repeated for the Debye Scherrer rings corresponding to

the deformed sample to obtain d_i where i=1, 2, 3…n represents deformation states 1, 2, 3… n. The normalized lattice spacing change (ϵ_{lat}) is then calculated for each azimuthal sector j at deformation state i using

$$\epsilon_{\text{lat}}^{j} = \frac{d_i^j - d_0^j}{d_0^j}. \qquad 6\text{- }1$$

Note that ϵ_{lat} corresponds to a particular family of planes and can be calculated for the {110}, {200}, {211}, {310} families independently. Further, it is elastic in origin i.e. it is an indication of the elastic strains developed during deformation. It is therefore necessary to obtain a similar elastic strain distribution within the crystal plasticity framework presented next.

The post deformation lattice spacings due to elastic distortions are calculated within the crystal plasticity finite element framework using the methodology presented by Erinosho and Dunne [68]. This technique calculates an element by element lattice spacing corresponding to each family of planes present (i.e. {110}, {200}, {211} etc) by using the elastic deformation tensor $\boldsymbol{F}^{\text{e}}$. Consider Fig. 6-4 which shows an incoming x-ray ([100] direction) which interacts with a crystal of known crystallographic configuration. Each plane that satisfies Bragg's condition will diffract the x-ray to the detector. Note that the detector is parallel to the (010) plane. The position of the diffracted beam on the detector depends on the local crystallographic configuration of the crystal and this technique is detailed by Wong et al.[42]. Each diffracted beam that is recorded on the detector corresponds to a plane within a crystal (or element within the computational framework) and contains information on its crystallographic orientation as well as the lattice spacing. The planes of similar crystallographic orientation will diffract the x-ray to similar regions on the detector as described earlier in the experimental setup. However, unlike the experiment in which

intensities are recorded, the lattice spacing is directly evaluated from the elastic deformation tensor using

$$\frac{a}{a_0} = |\boldsymbol{F}^{\mathrm{e}}\boldsymbol{e}_1^{\mathrm{c}}|, \frac{b}{b_0} = |\boldsymbol{F}^{\mathrm{e}}\boldsymbol{e}_2^{\mathrm{c}}|, \frac{c}{c_0} = |\boldsymbol{F}^{\mathrm{e}}\boldsymbol{e}_3^{\mathrm{c}}| \qquad 6\text{- }2$$

where $a_0 = b_0 = c_0 = 2.88$ Angstroms are the undeformed lattice lengths and $\boldsymbol{e}_1^{\mathrm{c}}$, $\boldsymbol{e}_2^{\mathrm{c}}$ and $\boldsymbol{e}_3^{\mathrm{c}}$ are unit orthogonal vectors rotated into the deformed crystallographic configuration. That is,

$$\boldsymbol{e}_i^{\mathrm{c}} = \Delta\boldsymbol{R}^{\mathrm{c}}\boldsymbol{R}_0^{\mathrm{c}}\boldsymbol{e}_i \qquad 6\text{- }3$$

where i =1, 2 and 3 corresponds to the [100], [010] , and [001] directions respectively, $\boldsymbol{R}_0^{\mathrm{c}}$ is a rotation matrix which maps the undeformed crystal to the local crystallographic configuration and $\Delta\boldsymbol{R}^{\mathrm{c}}$ maps the local crystal orientation into the deformed state. Full details of the crystal orientation mappings can be found in [68]. With knowledge of the deformed lattice lengths, the lattice spacing for all possible *hkl* planes in an BCC crystal can be obtained using [37]

$$d_{hkl} = \left(\sqrt{\frac{h^2}{a^2} + \frac{k^2}{b^2} + \frac{l^2}{c^2}}\right)^{-1}. \qquad 6\text{- }4$$

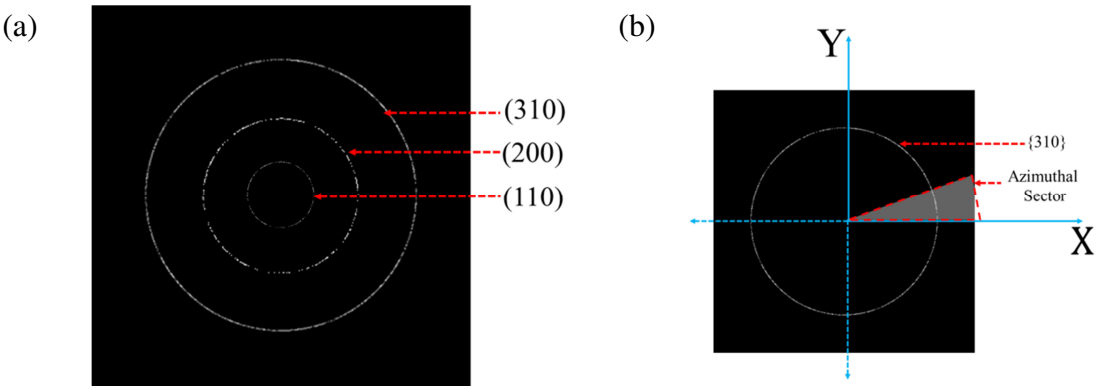


Fig. 6- 1: Schematic of Debye Scherrer rings corresponding to a particular deformation state. (a) shows the set of rings of planes that satisfy the Bragg condition in BCC ferritic steel and (b) shows a schematic of the binning of azimuthal sectors

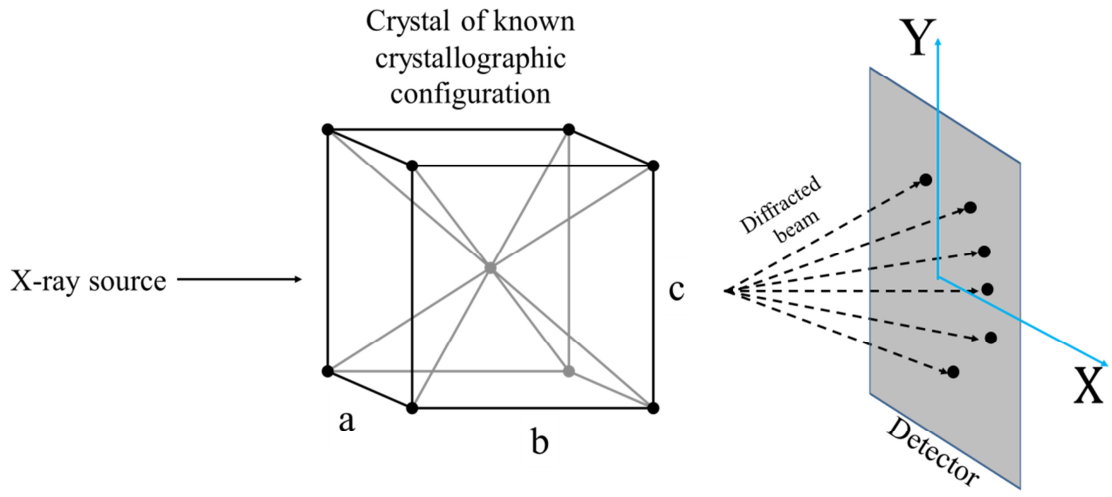


Fig. 6-2: Schematic of the computational approach used to simulate x-ray diffraction using crystal plasticity

Similar to the experiment, the normalized lattice spacing change ($\epsilon^{j}_{\text{lat}}$) for each sector j illustrated in Fig. 6-1b is calculated using

$$\epsilon^{j}_{\text{lat}} = \frac{\frac{\sum_{k=1}^{n_j} d_j^k}{n_j} - d_0}{d_0} \qquad 6\text{- }5$$

where k=1,2,… n_j. n_j is the total number of planes that diffract within a particular sector j. Note that the theoretical d_0 corresponding to a particular family of planes is adopted in the modelling, whereas in the experiments, d_0 depends on the undeformed reference sample. Thus, using Eq. 6-4, d_0=2.0364657 Angstroms for the {110} family of planes and similarly, d_0= 1.44 Angstroms for the {200} family.

6.2. X-ray diffraction lattice strain measurements

This section provides a systematic study of simulated x-ray diffraction measurements calculated using crystal plasticity. By using the methodology presented in previous section, single crystal behaviour is first analysed followed by a description of polycrystal response for a range of textures. The aim is to provide a coupling between crystal plasticity finite element calculations and simulated x-ray diffractions whilst capturing the statistics of the

experimental interaction volume. A range of validatory examples are presented and include analysis of single crystal response, the number of reflections in polycrystal systems, and the satisfaction of Bragg's law for conditions for diffraction. Subsequently, the polycrystal textures are then subjected to both uniaxial and biaxial straining to evaluate the lattice strain distribution evolution during the loading history. Further, comparisons are made with experimental measurements and discussed.

6.2.1.Single crystal simulations

This section provides a basic understanding of the simulated diffraction method using a single crystal. It provides a useful insight into the contribution to the Debye Scherrer ring of individual planes (usually termed reflections) as a function of crystallographic orientation. The single crystal shown in Fig. 6-3 is modelled using ABAQUS C3D8R elements and the material properties detailed in section 2 are used. For simplicity, only the 12 {110} family of planes are considered and for each example, the normalized lattice spacing change described in the previous section is shown as a function of the azimuthal angle (sector position) on the Debye Scherrer ring measured from the X-direction shown in Fig. 6-1. Note that satisfaction of Bragg's condition is not enforced in this example as the aim is to show in simple terms the effects of plane orientation on the location of the diffracted spot seen on the virtual detector. Note that all azimuthal angle measurements are with respect to the X-direction in Fig. 6-1. Also, due to symmetry about the X-direction in Fig. 6-1, half of the ring only is considered. That is, a point on the Debye Scherer ring that falls 90^0 from the X-direction in the clockwise and anticlockwise directions are considered equivalent and assumed to have the same crystallographic orientations.

Consider first the case of zero strain in the reference configuration shown in Fig. 6-3. The reference configuration refers to the case when the local crystallographic axes of the single

crystal coincide with the global 1, 2 and 3-directions. Zero normalized lattice spacing change is expected and the peak positions are defined at 0^0, 45^0, 90^0 and 135^0 denoted as A, B, C and D respectively. Note that the corresponding associated planes for each peak are detailed in Fig 6-3. Next, consider the non-reference configuration for the zero macroscopic strain example such that the local principal axes of the reference crystal have been rotated relative to the global 1-, 2- and 3 axes. Here, the reference crystal axes have been rotated using the rotation matrix formed by $\boldsymbol{R}_3\boldsymbol{R}_2\boldsymbol{R}_1$ where $\boldsymbol{R}_3$=283^0, $\boldsymbol{R}_2$=222^0 and $\boldsymbol{R}_1$=358^0 represent rotations about the 3-, 2- and 1- axes respectively. Note that in all cases, the incoming x-ray beam direction remains fixed and for this reason, the rotation creates the response seen. As expected, for no applied strain, zero lattice spacing change is seen. However, rather than the four distinct modes (A, B, C and D) observed in the reference configuration, there is a spread of the diffracted peaks in the rotated crystal.

Now consider the example under 2-direction uniaxial straining in the reference configuration. It is seen that the distinct peaks defined as A, B and D are in tension while the <101> family of planes (Peak C) are in compression. This is expected by visualizing the schematic of lattice planes presented such that planes with components in the loading direction experience tension and the <101> family which is influenced by the lateral compression is in compression. By considering the non-reference configuration under uniaxial straining, the variation in behaviour of each individual plane becomes more apparent. There is a spread in the peak position coupled with an associated lattice spacing change either in tension or compression. Next, consider the biaxial case (loading in the 1- and 2- direction) which shows even more variations in behaviour evident in the two crystallographic configurations considered. In the reference configuration, one distinct peak (A) with an associated lattice strain is seen and peaks B, C and D with approximately zero strain are observed. The <110> family of planes corresponding to Peak A are all in tension resulting in the associated lattice

strain seen. However, the constituent planes of peaks B, C and D have counter effects of balanced tension and compression leading to zero average normalized lattice spacing change. Finally, the non-reference configuration shows a spread in the peak positions due to the crystallographic orientation relative to the incoming x-ray beam.

The single crystal example shown provides the basis from which the diffraction responses and the effect of crystallographic rotations on the peak positions in polycrystals may be interpreted. It has also provided a basic understanding of the planes that contribute to a particular peak position and will be utilised to aid understanding of the polycrystal responses introduced in the next section.

6.2.2.Lattice strains in polycrystals

In considering polycrystal lattice strains, each orientation in the polycrystal model is assumed potentially to contribute to the Debye Scherrer ring depending on whether Bragg's law is satisfied, or otherwise. In what follows, the textures considered are shown and a sensitivity study is presented to determine an appropriate number of grains to be adopted in the polycrystal analysis. Subsequently, a study is presented to evaluate the consequence of the angular tolerance applied in satisfying the Bragg condition. The predicted polycrystal lattice spacings are also evaluated against experimental measurements and comparisons made.

The textures adopted in this study are presented in Fig. 6-4. T-1 is a nominally random texture with a slight bias in the [100] direction as seen by the pole figures shown, and the consequence of this is discussed later when compared to a strictly random texture (T-2). T-3 (Exp) is an experimentally measured ferritic steel texture obtained using Electron Back Scattered Diffraction (EBSD) and T-3 (Sim) is a computational polycrystal representation of T-3 (Exp) showing small differences, but with qualitative agreement apparent for all poles considered.

Four polycrystal grain set sizes are adopted with $3 \times 3 \times 3$, $5 \times 5 \times 5$, $6 \times 6 \times 6$ and $8 \times 8 \times 8$ grains as illustrated in Fig. 6-5. Grains are shown as regions of similar colour and a uniform mesh refinement ($6 \times 6 \times 6$ elements per grain) is adopted in all oligocrystal models. The models are assigned the nominally random texture (T-1) shown in Fig. 6-6 and subjected to 10 percent biaxial straining in the 1- and 2-directions shown. Note that the boundary conditions are such that all faces are constrained to remain planar. Using the methodology described above, the normalized lattice spacing change is calculated for the {110} family of planes and presented against the azimuthal angle about the Debye Scherrer ring. Further, unless otherwise stated, an angular range of 10^0 is adopted per azimuthal sector, giving rise to 18 sectors about the Debye Scherrer ring. In the simulations, isotropic hardening is adopted.

Consider Fig. 6-6 which shows the number of reflections/planes contributing to each azimuthal sector in the four oligocrystal shown in Fig. 6-5. Three examples are shown for differing constraints on the satisfaction of Bragg's condition. Fig. 6-6a shows the number of reflections when Bragg's condition is strictly satisfied (0.01^0 tolerance) whilst Figs. 6-6b and 6-6c show examples of more relaxed constraints on Bragg's condition (1^0 and unbounded tolerances respectively). It is clear from Fig. 6-6 that increasing the number of grains clearly increases the number of reflections potentially contributing to the Debye Scherrer ring. Also, it is immediately clear that a significant loss of statistical points contributing to the Debye Scherrer ring is apparent by satisfying Bragg's condition with tighter tolerance as seen in Figs. 6-6a-c, for a given number of grains. Strictly, only planes which satisfy Bragg's condition should contribute to the Debye Scherrer ring, but this generally leads to the need for the inclusion of many grains in the polycrystal model in order to generate a representative Debye Sherrer ring, with consequent long computer analysis times. Consequently, the $8 \times 8 \times 8$ grain model in Fig. 6-5 is henceforth utilised. Two azimuthal sector binning ranges are also investigated. An azimuthal sector, shown in Fig. 6-1 represents a region on the

Debye Scherrer ring in which planes of similar orientation diffract the incident beam. In the previous section, 10^0 was adopted as sufficient to bin similarly oriented lattice planes. In order to investigate the sensitivity, 5^0 bins are also evaluated for the three tolerances of Bragg satisfaction (0.01^o, 1.0^o and unbounded) and the results are shown in Fig. 6-9.

In Fig. 6-7a, 5^o bins have been used for each azimuthal sector and in Fig. 6-7b, 10^o bins are chosen. Fig. 6-7a indicates that deviation from statistical representation is apparent by strictly obeying the Bragg condition seen in the 0.01^0 case due to the resulting small number of reflections included. However, upon relaxing the diffraction conditions, a smoother distribution is obtained. A similar response is obtained by using 10^o bins shown in Fig. 6-7b for the three diffraction tolerances but with less fluctuation due to increased averaging. In both cases, however, the sector binning size has only small effect on the observed distribution especially for the unbounded Bragg case.

It is worth commenting on the nature of the lattice spacing change distribution seen in Fig. 6-7 for the unbounded case. Due to the biaxial nature of applied loading, a relatively uniform distribution of lattice spacing change is expected irrespective of direction about the Debye Scherrer ring. Whilst this is the case in a fully random texture, that for texture T-1 is preferentially oriented in the [100] direction and for this reason the small variation in spacing is seen. This is highlighted by considering the more strictly random texture, T-2 given in Fig. 6-4, which has also been subjected to the same biaxial straining, for which the results obtained, and compared to texture T-1, are shown in Fig. 6-8. It is clear from Fig. 6-8 that the more strictly random texture T-2 results in a more uniform lattice spacing response irrespective of orientation (rotation from X) as expected, thus, providing some insight into the role of texture on the observed orientation dependent lattice spacing response.

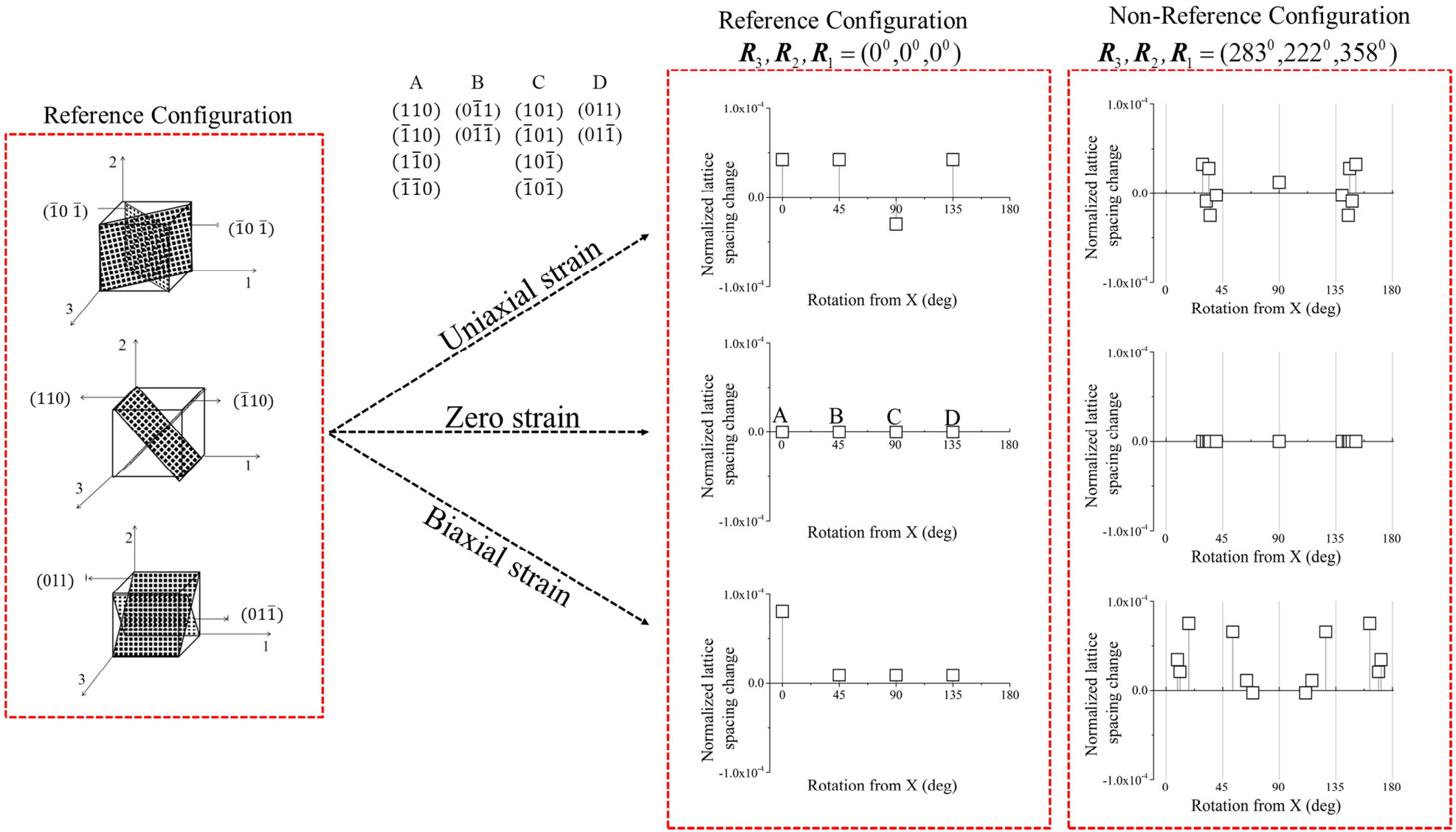


Fig. 6-3: Systematic study of diffraction by {110} family of planes in single crystal ferritic steel.

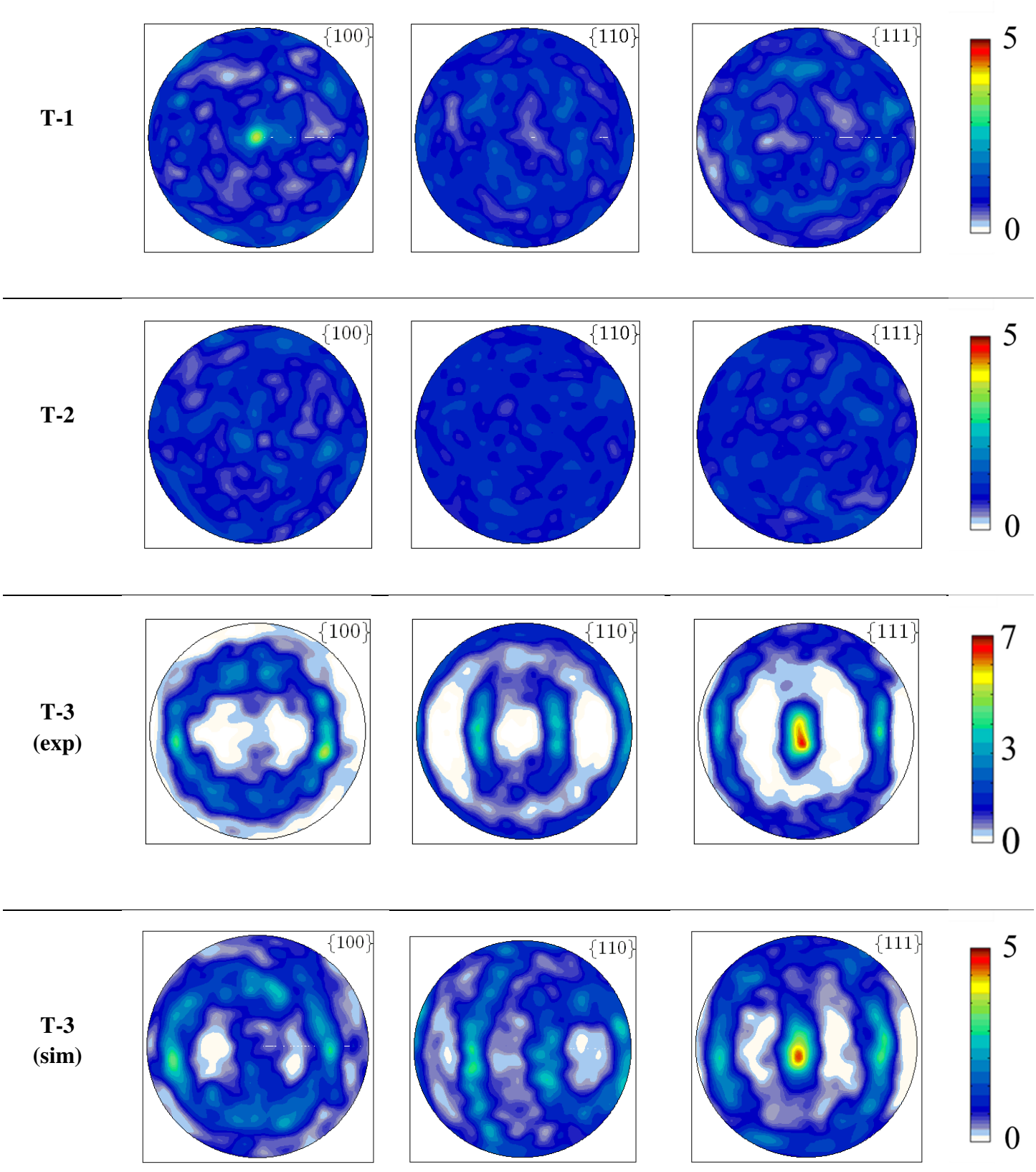


Fig. 6-4: Initial textures used in the simulations showing [T-1] a nominally random texture, [T-2] a fully random texture, [T-2(Exp)] an experimentally obtained ferritic steel texture and [T-2 (Sim)] a computational polycrystal representation of the texture [T-2 (Exp)].

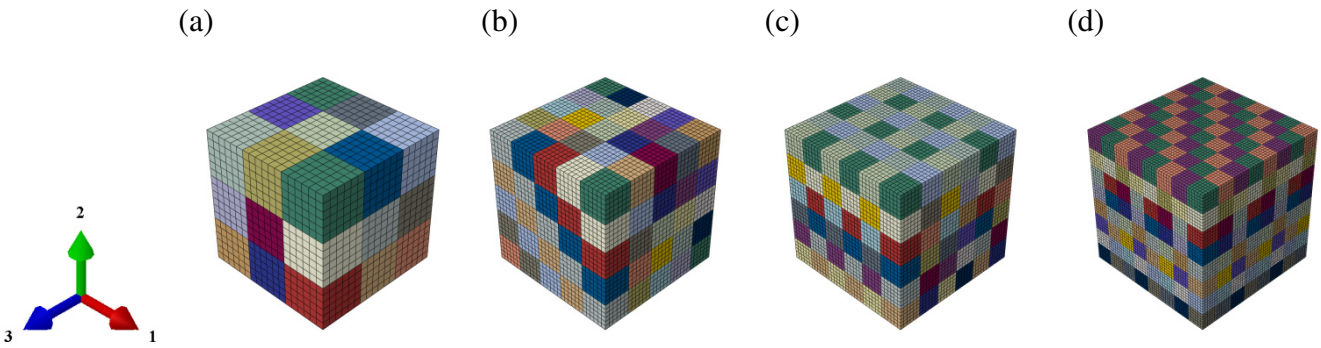


Fig. 6-5: The range of polycrystal models with differing number of grains (a) $3 \times 3 \times 3$, (b) $5 \times 5 \times 5$ (c) $6 \times 6 \times 6$ and (d) $8 \times 8 \times 8$ grains which are used to calibrate the simulated diffraction responses. Note that the same mesh refinement ($6 \times 6 \times 6$ elements per grain) was adopted per grain in all oligocrystal models and each grain had dimensions of $25 \times 25 \times 25 \mu m^3$

Finally, in this section, we note that the imposition of satisfaction of the Bragg condition to within a prescribed tolerance is carried out in order to replicate the selection of reflections contributing to the lattice strains obtained from experimental x-ray diffraction. However, no such constraint applies in the model and all lattice planes may be included in order to give the full distribution of lattice strains. Hence, subsequently in this paper, the unbounded Bragg condition is adopted in order to capture a statistical representation of the lattice spacing changes within the polycrystal, and 10^o azimuthal sector sizes are deemed appropriate. The effects of texture and hardening on lattice spacing distributions and their evolutions are presented next.

6.3. Effects of texture and hardening on lattice spacing distributions in ferritic steel polycrystals

This section addresses the lattice spacing distribution changes obtained under differing deformation conditions. A description of the experimentally obtained results is presented first followed by detailed comparisons with the predicted lattice spacing changes obtained from crystal plasticity technique presented above.

Fig. 6-9 shows the measured normalized lattice spacing changes under biaxial (Fig. 6-9a) and uniaxial (Fig. 6-9b) deformation for the experimental texture T-3 shown in Fig. 6-4. Consider first Fig. 6-9a which shows the lattice spacing changes at 10% biaxial strain i.e. $\varepsilon_2 = \varepsilon_1 = 0.1$. The x-axis shows the *macroscopic strain* (ε_2), where $\varepsilon_2 = \varepsilon_1$, while the y-axis shows the *rotation from X-direction* illustrated in Fig. 6-1b. The colour indicates the measured normalized lattice spacing change calculated from Eq. 6-6 and the methodology for its determination is described in section 6.1. Note that 10^o azimuthal sector bin sizes have been adopted for this analysis.

It is apparent from Fig. 6-9a that biaxial straining results in a relatively uniform lattice spacing change distribution irrespective of the azimuthal sector (rotation from X illustrated in Fig. 6-1b). This uniform response is reasonable since $\varepsilon_2 = \varepsilon_1$ and the lattice planes are subjected to similar levels of strain irrespective of orientation thereby resulting in the response seen. Different behaviour is, however, seen under uniaxial straining shown in Fig. 6-9b whereby the planes that diffract at 90^0 from X-direction are noticeably in tension while those oriented away progressively show compressive behaviour. This can be explained by evaluating the experimental texture T-3 (exp) whose pole figure is shown in Fig. 6-4 relative to the loading direction. It can be seen that the experimental texture T-3 has a preference in the [111] direction as seen in the pole figure shown in Fig. 6-4 and the crystallographic orientation is such that the normals to the (111) planes are oriented in the 3- direction of the crystal shown in Fig. 6-4. Hence, to illustrate, a single crystal with initial configuration chosen such that the (111) normal is oriented in the 3- direction is subjected to uniaxial straining in the 2- direction and the resulting normalized lattice spacing change is shown in Fig. 6-10. For this crystallographic configuration, it is clear that the planes that diffract at 0^0 and 180^0 are in compression and the planes that diffract towards 90^0 are in tension similar to the textured polycrystal measurements seen under uniaxial straining in Fig. 6-9b.

Simulated x-ray diffraction results, calculated from the crystal plasticity approach, are also assessed. Two forms of hardening are considered and the resulting lattice spacing deformation maps are discussed.

The model polycrystal textures shown in Fig. 6-4 are subjected to biaxial and uniaxial straining under the two forms of hardening (self- and isotropic). For all cases, the unbounded Bragg condition described previously is adopted such that all planes within the polycrystal are assumed to contribute to the Debye Scherrer ring. Also, the evolutions of lattice spacing change under uniaxial and biaxial straining are presented for the {110} family of planes in the plastic region (ε_2>0.03) in order to capture subtle changes in lattice spacing variations.

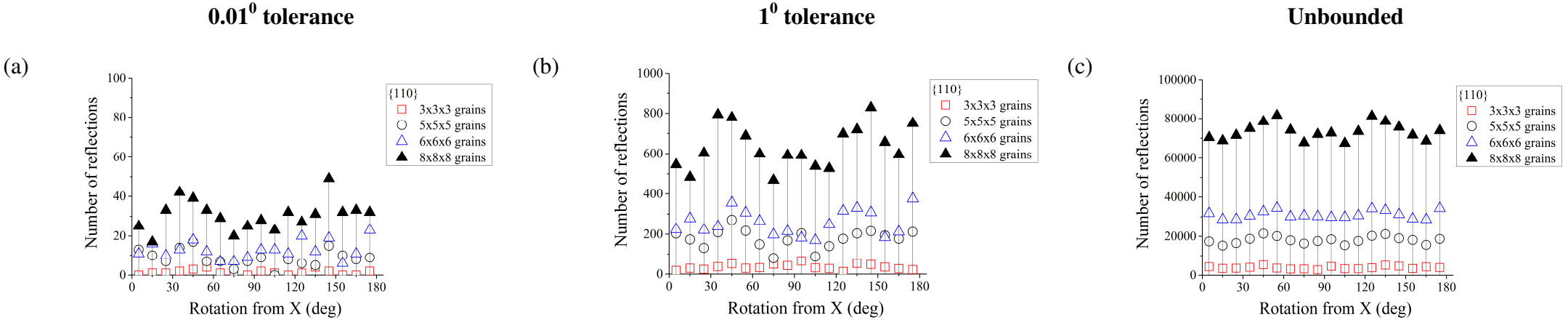
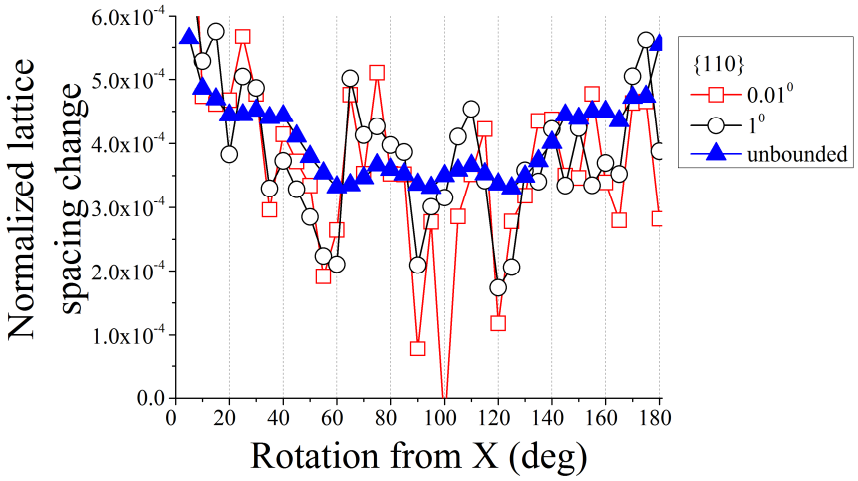


Fig. 6-6: The number of reflections (diffracted points) per orientation (rotation from X-direction shown in Fig. 6-3) for the range of oligocrystal models shown in Fig. 6-7. (a) shows 0.01^0 tolerance on Bragg's condition, (b) 1^0 tolerance and (c) unbounded in which all planes contribute to the Debye Scherrer ring

5 degrees binning



10 degrees binning

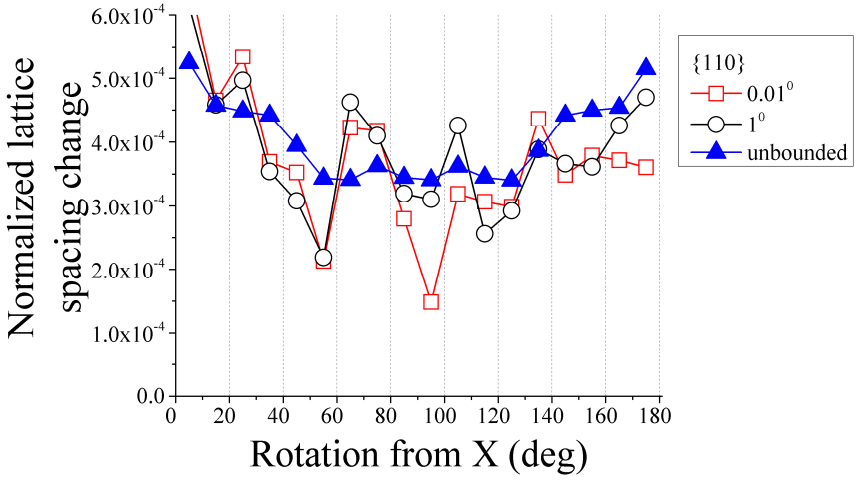


Fig. 6-7: Calculated {110} normalized lattice spacing change for nominally random texture (T-1) subjected to 10 percent biaxial straining in the 1- and 2-directions of the polycrystal shown in Fig. 6-7d for differing levels of satisfaction of Bragg's condition (0.01^0, 1^0 and unbounded). The azimuthal sector binning sizes employed are (a) 5^0 azimuthal sector size and (b) 10^0 azimuthal sector binning size

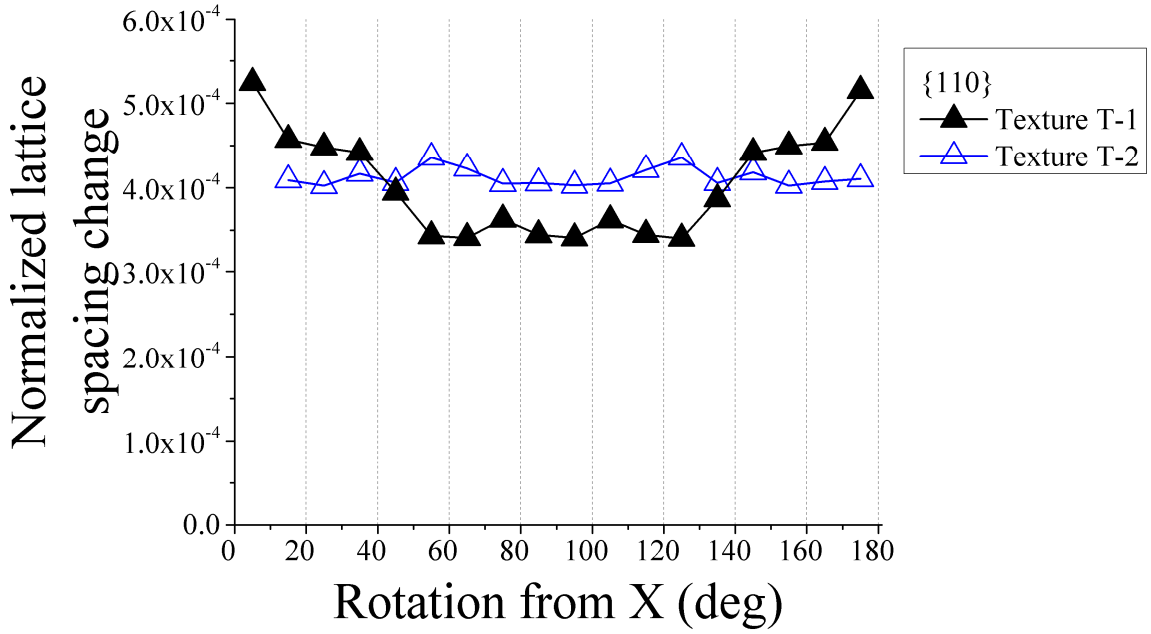


Fig. 6-8: Comparison of normalized lattice spacing change for the nominally random texture T-1 and the strictly random texture, T-2

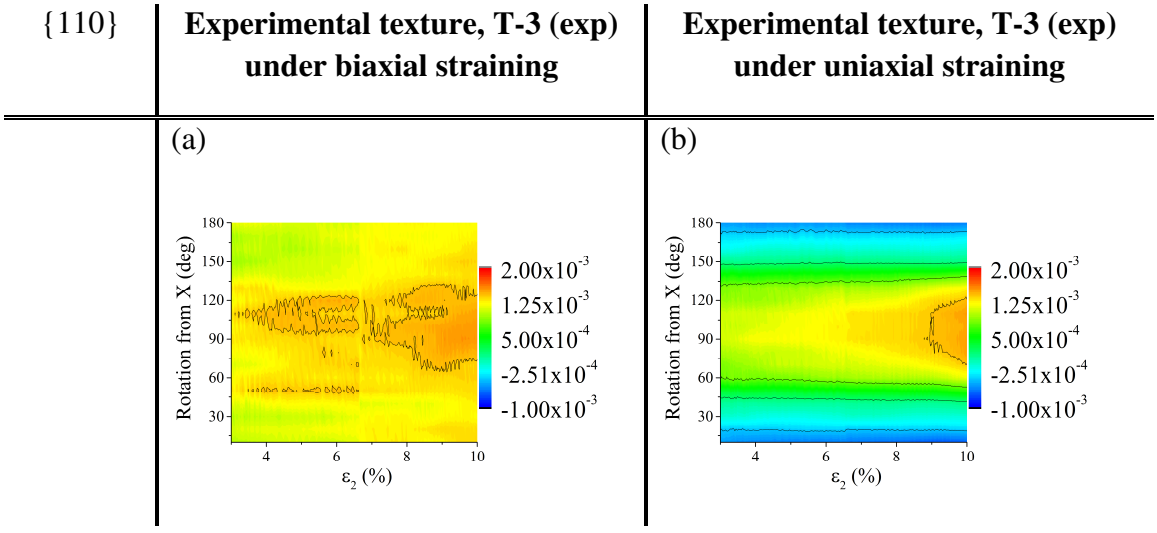


Fig. 6-9: Experimental evolution of {110} normalized lattice spacing change for texture T-3 subjected to **uniaxial and biaxial straining**

Crystallographic configuration **Normalized lattice spacing change**

(a) (b)

$[(\boldsymbol{R}_3 = 0^0)(\boldsymbol{R}_2 = 306^0)(\boldsymbol{R}_1 = 180^0)]$

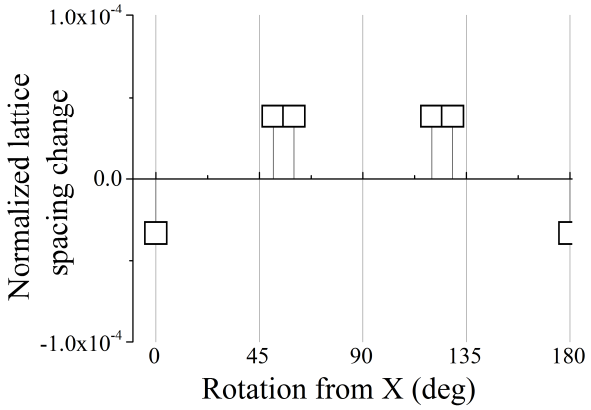


Fig. 6-10: Calculated {110} normalized lattice spacing change for single crystal with the initial configuration specified in (a) and the normalized lattice spacing change shown in (b). Note that $\boldsymbol{R}_3$, $\boldsymbol{R}_2$ and $\boldsymbol{R}_1$ are crystallographic rotation matrices with respect to the global 3- 2- and 1- axis shown in Fig. 6-3

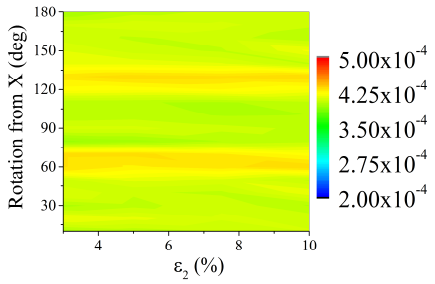
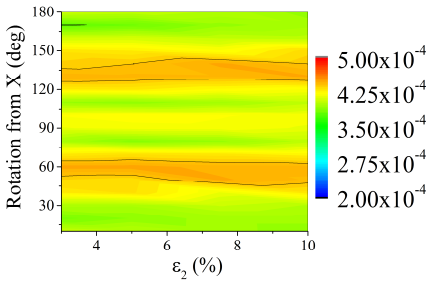
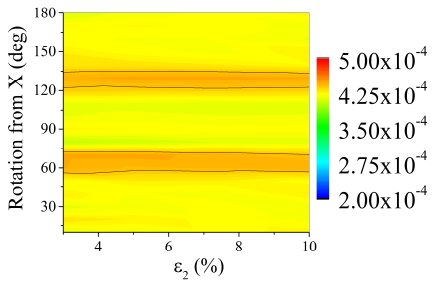
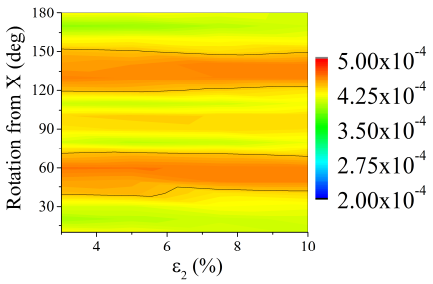
{110}	**Random Texture, T-2**	**Experimental Texture, T-3 (sim)**
Isotropic Hardening	(ai) 	(bi) 
Self-hardening	(aii) 	(bii) 

Fig. 6-11: Evolution of {110} normalized lattice spacing change for random texture T-2 and experimental texture T-3 (sim) subjected to **biaxial straining** calculated under isotropic and self-hardening

Fig. 6-11 shows the predicted lattice spacing change distribution for the {110} family of planes in random texture T-2 and experimental texture T-3 (sim) subjected to 10% biaxial straining under isotropic and self-hardening. Considering isotropic hardening for both textures considered, it is seen that the two textures show similar lattice spacing distribution evolution which is approximately uniform irrespective of orientation (Rotation from X-). However texture T-3 (exp) shows stronger variation evident from the bands at 60^0 and 130^0. These features are more pronounced under self- hardening for both textures considered. An earlier section on single crystal behaviour (Fig. 6-3) showed the effect of straining and rotation on the diffraction response. It was shown that planes generate diffraction patterns depending on crystallographic orientation and that planes associated with the distinct modes shown in Fig. 6-5 (A, B, C and D) diffract to a particular region of the Debye Scherrer ring and also spread into a band within this region. As a result, it is possible to specify tolerance regions local to each distinct mode (A, B, C and D) to which a family of planes with a particular crystallographic orientation will diffract. For example, the <101> family of planes shown in Fig. 6-3 can diffract in a band local to peak C and the same applies to peaks A, B and D. On this basis, it is easier to interpret the variations in lattice spacing change seen in Fig. 6-11.

It becomes evident from the deformation maps for the approximately random texture, T-2, that a particular family of planes diffracting at $\sim 60^0$ and $\sim 120^0$ are experiencing comparatively more tensile strains indicating that the texture is in fact not fully random. This is further seen by comparing the random T-2, with the experimental T-3 (exp) textures for which more pronounced bands under both hardening types develop. Due to the texture, the family of planes diffracting within the tensile bands seen are favourably oriented leading to the larger lattice strains seen. This also accounts for the more pronounced influence of hardening on the lattice spacing changes in the textured polycrystal (T-3). Whilst the bands

developed in both textures are more pronounced under self-hardening, it requires significant deformation to develop a preferred orientation in the random texture compared to the initially textured polycrystal thereby accounting for the differences in the nature of the bands in both textures.

Fig. 6-12 shows the {110} lattice spacing changes for random texture T-2 and experimental texture T-3 (sim) subjected to 10% uniaxial straining. Similar to the biaxial case shown above, the normalized lattice spacing change is shown along the deformation history for each azimuthal sector (Rotation from X- illustrated in Fig. 6-3b). Consider first Figs. 6-12ai and 6-12aii which shows the lattice spacing change for the initially random polycrystal texture under isotropic and self- hardening respectively.

Two bands are seen similar to Figs. 6-11a and 6-11b, however with lower magnitudes in this case due to the fact that more planes are in compression under uniaxial straining compared to biaxial. Also, the two bands seen between 30^0-80^0 and 110^0-150^0 can be explained similarly to the biaxial case by evaluating the planes that contribute to each diffraction region. Here, the family of planes in this region (<011>) are experiencing higher net tensile strains with respect to the other families i.e. <110> and <101>, thereby leading to the differences seen. Next, consider Fig. 6-12b which shows the lattice spacing change in the initially textured polycrystal subjected to uniaxial straining. It is apparent that due to texture, the <101> planes at $\sim 90^0$ are favourably oriented in the loading direction leading to the larger lattice spacing changes observed. Other families of planes are also in tension but to a lesser extent and are more influenced by planes in compression leading to the relatively smaller lattice spacings seen.

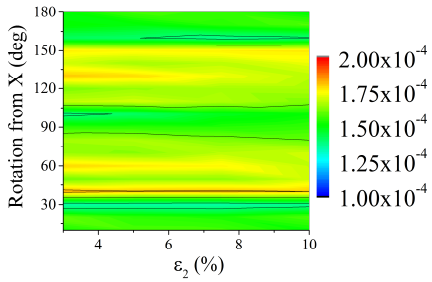
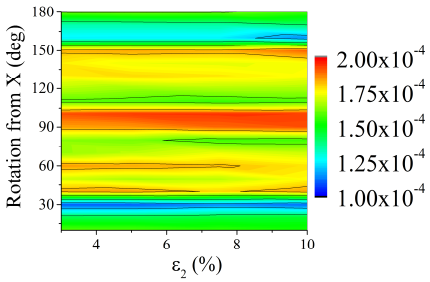
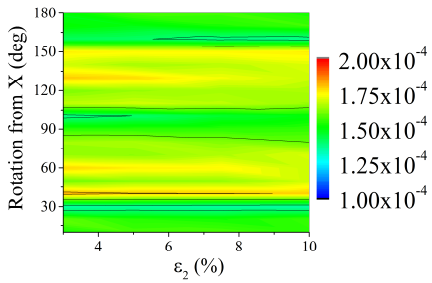
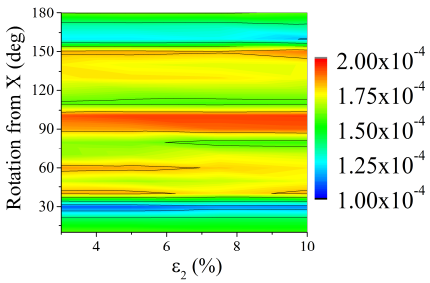
{110}	Random texture, T-2	Experimental texture, T-3 (sim)
Isotropic hardening	(ai) 	(bi) 
Self-hardening	(aii) 	(bii) 

Fig. 6-12: Evolution of {110} normalized lattice spacing change for random texture T-2 and experimental texture T-3 (sim) subjected to **uniaxial straining** under isotropic and self-hardening

The angular variations in lattice spacings observed under self- and isotropic hardening are seen to be more pronounced under biaxial straining compared to uniaxial straining. Under isotropic hardening, all slip systems undergo the same levels of hardening based on the maximum level of slip achieved as illustrated in Eq. 2-14. Self- hardening on the other hand is different in that hardening on a slip system depends solely on the level of slip on that system alone. Hence, isotropic hardening is expected to result in more uniform distributions.

In the deformation maps presented in Figs. 6-11 and 6-12 for biaxial and uniaxial straining respectively, differences are observed by comparing both forms of hardening and these differences are more pronounced under biaxial compared to uniaxial straining. Biaxial deformation by nature is more uniformly distributed irrespective of orientation (Rotation from X) compared to uniaxial straining and this is evident by comparing both deformation

paths under the same form of hardening. However, by comparing isotropic with self-hardening for the same deformation path (biaxial or uniaxial), there are differences seen in the deformation maps. Considering the biaxial case shown in Fig. 6-11, it is clear that the nature of the deformation and form of hardening both influence the behaviour seen. Since isotropic hardening depends on the systems with the maximum achieved slip, it becomes apparent that loading in two principal directions of the polycrystal leads to more systems being activated and the one with the maximum slip determining the local level of hardening. However, under uniaxial straining shown in Fig. 6-12, there is only one primary straining direction resulting in fewer slip system variations since slip depends on the local crystallographic orientation relative to the loading direction. In effect, it is argued that similar slip system orientations are likely to control deformation in both hardening cases under uniaxial straining thereby leading to smaller differences in lattice spacing distributions seen.

The experimentally measured lattice spacings and their comparison with those predicted from crystal plasticity simulations are discussed next with reference to Figs. 6-9, 6-11 and 6-12. Dawson et al. [42, 69-72] have pioneered studies on simulated x-ray diffraction in order to create a link to computational modelling techniques. They have used this technique to study welding, crack initiation etc and the major advantage of simulated diffraction so far as discussed by Dawson and co-workers is the possibility of using it as an auxiliary technique in combination with other characterization tools to inform material design processes. This notion is further highlighted in this study as the simulated results show good qualitative agreement with the experiment. For example, relatively uniform lattice spacing distributions are predicted under biaxial straining but less so under uniaxial strains. However, differences in lattice spacing magnitudes are observed in comparison with experiments and this is attributed to the averaging methodology currently adopted in which the satisfaction of Bragg's condition is neglected. Experimentally, the diffracted beam recorded at the detector

is a superposition of reflected beams from planes within the diffraction volume which is currently not accounted for within this simulated diffraction model. Each element within the crystal plasticity model is regarded as a crystal which interacts individually with the incoming x-ray beam resulting in diffracted points. This is an over-simplification of the diffraction process and results in the differences in lattice spacing changes in comparison with experimental measurements.

The crystal plasticity calculations show approximately one order of magnitude difference in lattice strain from those measured experimentally. The crystal modelling methodology has been to incorporate all planes (reflections) in calculating the distribution of lattice strain distributions, and not just those planes which satisfy the Bragg condition. The latter, of course, is the case for the experimental measurements. Also, depending on the monochromicity of the incoming beam, planes that lie parallel to the beam remain invisible and are unlikely to contribute to the Debye Scherrer ring without secondary diffraction mechanisms. All these subtleties associated with experimental x-ray diffraction, and the constraint imposed by the Bragg condition, make quantitative comparisons between experimental measurements and crystal plasticity computations difficult. Hence, a systematic study is presented in order to further analyse the deformation maps shown in Figs. 6-11 and 6-12 in comparison to experimental measurements. For simplicity, focus is placed on the initially textured polycrystal T-3 under isotropic hardening for biaxial and uniaxial deformation paths.

Figs. 6-13 and 6-14 shows the simulated deformation maps for the initially textured polycrystal under uniaxial and biaxial straining calculated using crystal plasticity which are then compared with the experimental measurements. However, unlike the deformation maps shown in Figs. 6-11 and 6-12, two limits are prescribed - lower bound and upper bounds which are described as follows. So far, the average lattice spacing is calculated for each

azimuthal sector of the Debye Scherrer ring shown in Fig. 6-1b using Eq. 6-5 such that all similarly oriented planes within each sector contribute to the average spacing. However, to examine the bounds, the average is calculated for the ten smallest and largest lattice spacings in each azimuthal sector corresponding to the lower and upper bounds shown in Fig. 6-15. Therefore, for the upper bound,

$$\max \in_{\text{lat}}^{\text{j}} = \frac{\frac{(\Sigma_{k=1}^{10} d_j^k)_{\max}}{10} - d_0}{d_0} \qquad 6\text{-}6$$

and the lower bound is given by

$$\min \in_{\text{lat}}^{\text{j}} = \frac{\frac{(\Sigma_{k=1}^{10} d_j^k)_{\min}}{10} - d_0}{d_0}. \qquad 6\text{-}7$$

Hence, the lower bound is an indication of the compressive lattice spacings per azimuthal sector whilst the upper bound is an indication of the tensile spacings in each azimuthal sector.

Consider Fig. 6-13 which shows the simulated deformation maps under uniaxial straining for the lower (Fig. 6-13a) and upper bound cases (Fig. 6-13b) described above. Fig. 6-13a shows compressive lattice spacings whilst Fig. 6-13b shows tensile lattice spacings as expected. It is seen that the upper bound deformation maps closely capture the tensile spacings measured experimentally (90^0 rotation from X) and the magnitudes are also comparable. This is further seen by evaluating the lattice spacing at *90^0 rotation from X* along the deformation history. It is clear from Fig. 6-13d that a good comparison is seen between simulation (upper bound) and experimental equivalent. This is unlike the example shown in Fig. 6-13e which shows the deformation map under uniaxial straining for the unbounded case. Note that in the unbounded case, the average lattice spacing per azimuthal sector is calculated based on the contributions from all planes within that sector. Hence, by taking a similar path described above (90^0 rotation from X), only qualitative comparisons are achievable with respect to the experiment.

This is further shown in Fig. 6-13f for self- and isotropic hardening which significantly underestimate the experimentally measured lattice spacings for the path evaluated.

Fig. 6-14 shows a similar analysis for biaxial deformation in which a lower (Fig. 6-14a) and upper (Fig. 6-14b) bound are calculated and compared to the experimental (Fig. 6-14c) measurement. As described previously, a relatively uniform distribution of strain is seen under biaxial straining irrespective of orientation (rotation from X) and Fig. 6-14 further shows a good agreement between the upper bound and the experimental measurement. Again, considering the deformation path along 90^0, it is evident from Fig. 6-14d that a good qualitative and quantitative agreement is seen between the experimental and crystal plasticity results which is otherwise lost by considering the unbounded case which takes account of all planes in a particular azimuthal sector. In the unbounded case, only qualitative agreement is seen as shown in Fig. 6-14e and Fig. 6-14f. It is therefore hypothesized that the Bragg condition which controls the selection processes of planes contributing to the experimentally measured lattice spacing accounts for the differences seen.

This hypothesis is further analysed in Fig. 6-15 which shows the orientation-dependent lattice spacing change under uniaxial and biaxial straining at 10% strain. Fig. 6-15a illustrates the lattice spacing change for each azimuthal sector of the Debye Scherer ring under biaxial straining and compares the upper bound, lower bound and unbounded with the experimental measurement. As described previously, the lower bound is a representation of the averaged ten smallest lattice spacings developed within the polycrystal simulation whilst the upper bound represents the largest. The unbounded accounts for the average of all lattice spacings that fall within a particular azimuthal sector assumed to have a common orientation. The results show that the experimental measurement and the upper bound lattice spacings are comparable both qualitatively and quantitatively. As expected, the lower bound lattice

spacings are in compression and the unbounded lies between the upper and lower bound with both showing only qualitative agreement with experimental measurements. Next, consider Fig. 6-15b which shows a similar analysis to that in Fig. 6-15a but for uniaxial straining. The experimental measurement shows that planes that diffract 90^0 *from X* corresponding to the <101> family of planes are in tension whilst the <110> and <011> families are progressively approaching compressive states. Although this is not explicitly seen in the crystal plasticity predicted lattice spacings (upper bound, lower bound and unbounded), it is clear that the upper bound approximately captures the maximum tensile spacing in the experiment and the lower bound also captures the minimum lattice spacings. The unbounded case which accounts for all lattice spacings per azimuthal sector is an average response only with qualitative agreement seen as it captures the higher lattice spacing in the <101> family (90^0 rotation from X) as seen inset in Fig. 6-15b. Due to the averaging method in the unbounded case, the expected compressive strains in the <110> and <011> families of planes are not fully seen; however, an indication is observed as seen by the relatively lower lattice strain in the corresponding regions i.e. 20^0-60^0 and 120^0-160^0 from X (see inset for Fig. 6-15b). Whilst it may prove difficult to capture quantitatively the experimentally measured magnitudes, the good qualitative agreement between experiments and the crystal plasticity predictions ensures that this technique can be a useful analysis tool. On this basis, it is used to further understand lattice spacings developed under non-proportional straining discussed next.

6.4. Non-proportionality of strain and effects on lattice spacing distributions

Following earlier computational studies on non-proportional straining in ferritic steel by Erinosho et al. [73] which showed the potential benefits of non-proportional straining on achievable ductility, it is important to further understand the strain distributions which form

under these deformation paths. Here, the normalized lattice spacing changes developed under non-proportional strain paths are presented and compared to experimental measurements.

Fig. 6-16 shows a schematic of a strain state C which is achievable by following path O-C. However, it is also possible to attain this strain state by following differing strain paths as seen in Fig. 6-16. For example, it is possible to undergo biaxial (A-1) followed by uniaxial deformation (A-2) or conversely, uniaxial (B-1) followed by biaxial (B-2) deformation. These two-phased stages are referred to as non-proportional strain paths and are likeliy to potentially lead to differing levels of achievable ductility.

Considering path A shown in Fig. 6-16, the 1- and 2- surfaces of the polycrystal shown in Fig. 6-5d are subjected to proportional biaxial straining (A-1) followed by proportional uniaxial straining in the 2- direction (A-2). Conversely, strain path B is such that the polycrystal is subjected to proportional uniaxial straining in the 2- direction (B-1) followed by proportional biaxial straining in the 1- and 2- directions respectively. Note that the experimental texture (T-3) shown in Fig. 6-4 is used here and in all simulations, and that all surfaces are constrained to remain planar. The goal here is to evaluate the lattice spacing changes developed for the two non-proportional strain paths under differing forms of hardening and compare the consequence of a uniaxial and biaxial pre-strain. Firstly, however, the experimentally measured normalized lattice spacing distributions for the two strain paths shown in Fig. 6-16 are discussed.

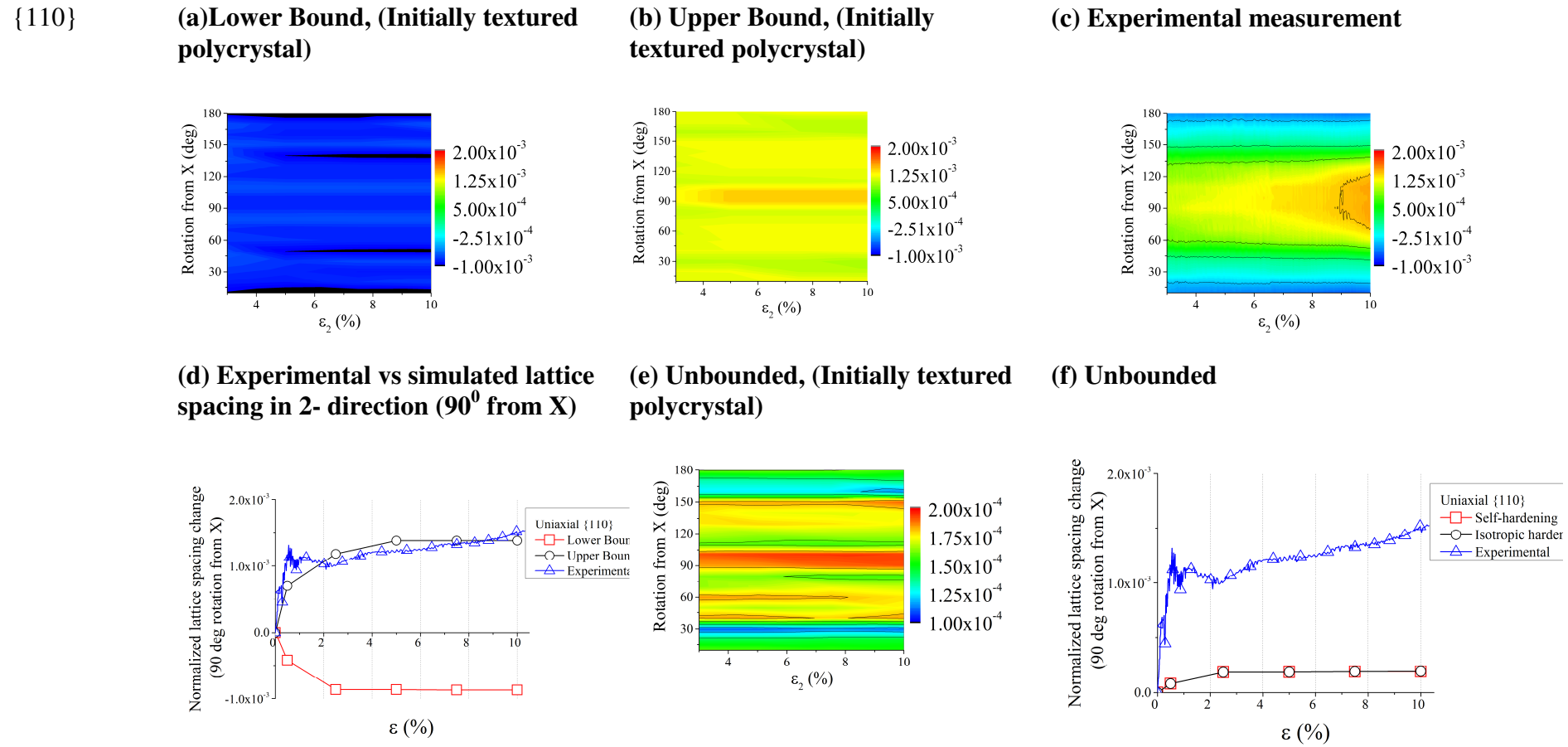
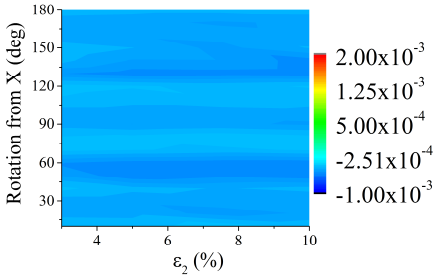


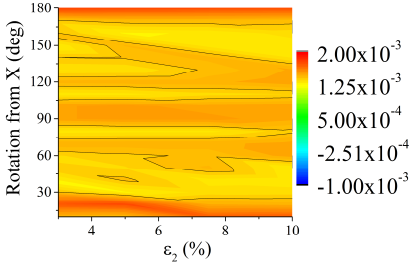
Fig. 6-13: Analysis of lattice spacing distribution under uniaxial straining in the initially textured polycrystal showing the normalized (a) lower bound, (b) upper bound and (c) experimentally measured lattice spacings. The lattice spacing at 90^0 rotation from X corresponding to the loading direction is compared between experiment and simulation in (d) while the unbounded lattice spacings are shown in (e). Finally, the lattice spacing in the unbounded case in the loading direction is compared for self- and isotropic hardening in (f). Note that unless otherwise specified, the calculated lattice spacings are under isotropic hardening

{110}

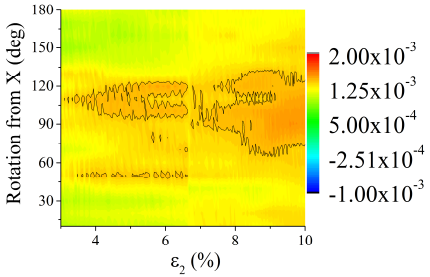
(a) Lower Bound, (Initially textured polycrystal)



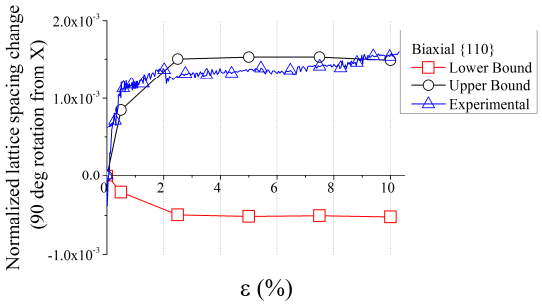
(b) Upper Bound, (Initially textured polycrystal)



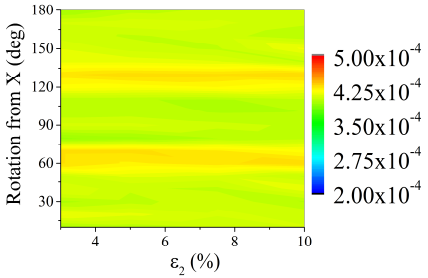
(c) Experimental measurement



(d) Experimental vs simulated lattice spacing in 2- direction (90^0 from X)



(e) Unbounded, (Initially textured polycrystal)



(f) Unbounded

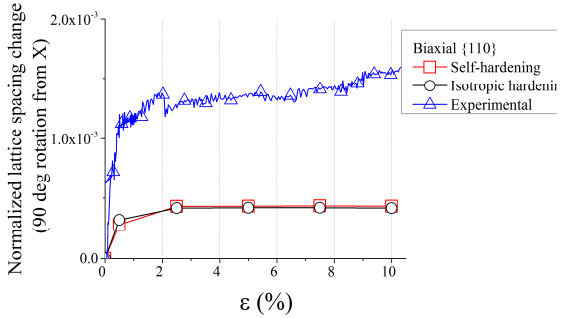
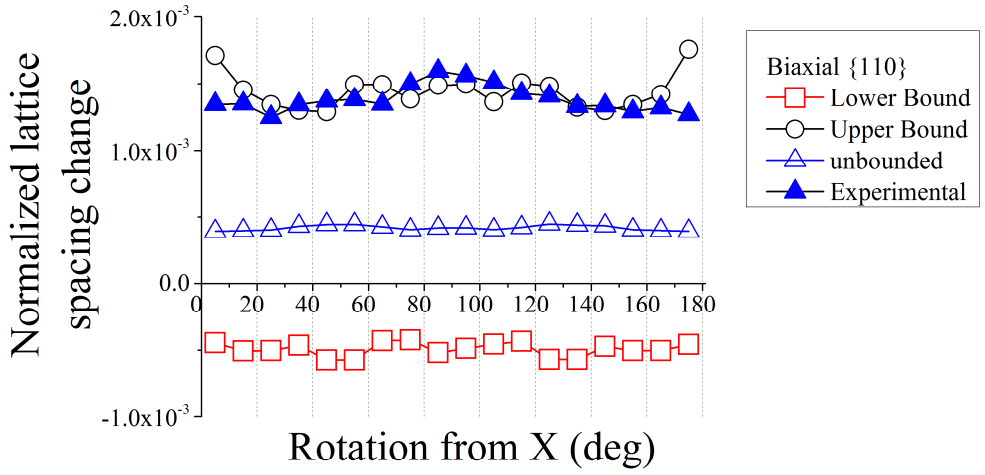


Fig. 6-14: Analysis of lattice spacing distribution underbniaxial straining in the initially textured polycrystal showing the normalized (a) lower bound, (b) upper bound and (c) experimentally measured lattice spacings. The lattice spacing at 90^0 rotation from X corresponding to a loading direction is compared between experiment and simulation in (d) while the unbounded lattice spacings are shown in (e). Finally, the lattice spacing in the unbounded case in a loading direction is compared for self- and isotropic hardening in (f). Note that unless otherwise specified, the calculated lattice spacings are under isotropic hardening.

(a)

Biaxial



(b)

Uniaxial

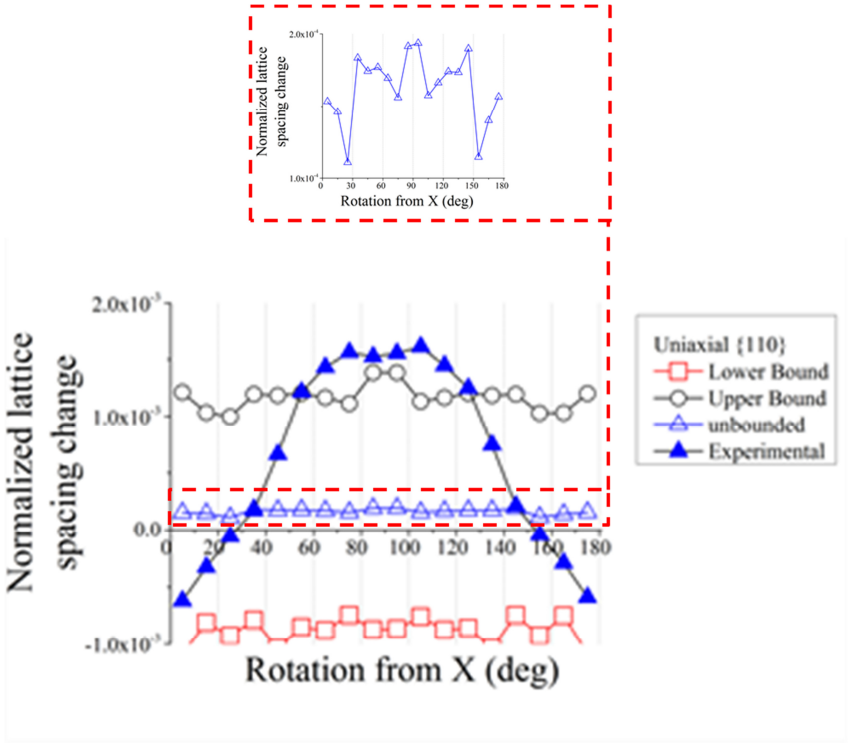


Fig. 6-15: Normalized lattice spacing changes at 10 percent (a) biaxial strain and (b) uniaxial strain

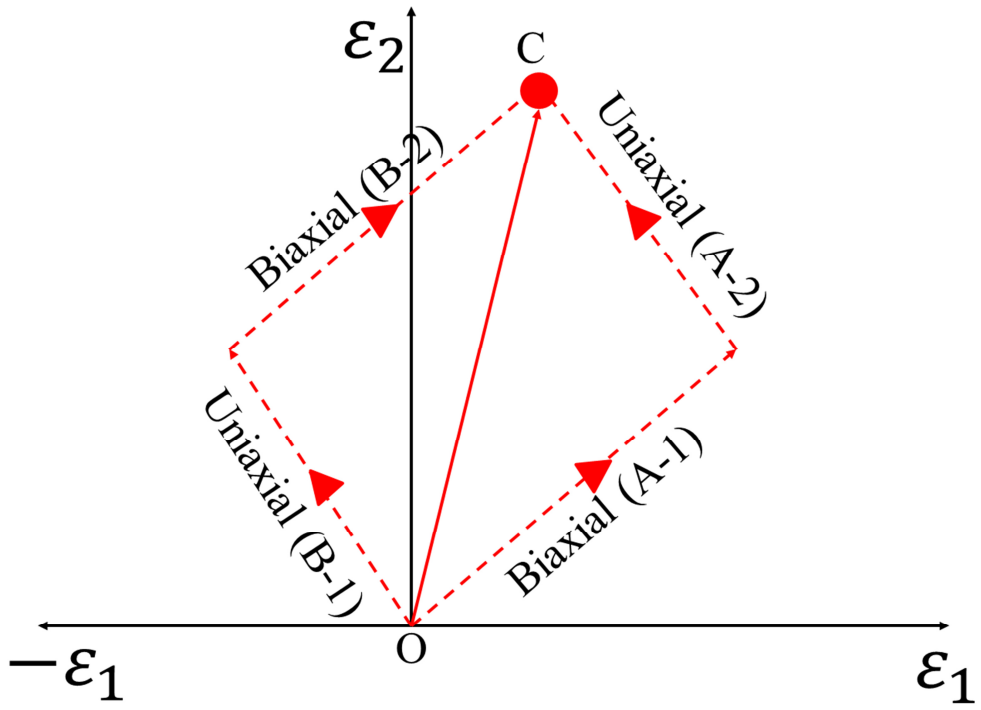


Fig. 6-16: Non-proportional paths adopted to achieve strain state C such that strain path A involves biaxial followed by uniaxial straining and strain path B undergoes uniaxial followed by biaxial deformation

6.4.1. Experimental measurement of lattice spacing changes under non-proportional strain paths

The deformation maps from experimental measurements of lattice spacing changes under the non-proportional strain paths shown in Fig. 6-16 are presented in Fig. 6-17. Fig. 6-17ai and aii are the deformation maps for strain path A-1 and A-2 respectively which are biaxial followed by uniaxial deformation. Similarly, Fig. 6-17bi and 6-17bii represent the deformation maps for paths B-1 and B-2 respectively illustrated in Fig. 6-16 and represent uniaxial followed by biaxial deformation.

Considering first Fig. 6-17ai and 6-17aii which represent the normalized lattice spacing change deformation maps corresponding to biaxial followed by uniaxial straining, a significant change in distribution of lattice spacing change is observed. Fig. 6-17ai is similar to that shown in Fig. 6-10a for proportional biaxial deformation. However, the deformation map in the subsequent uniaxial deformation does not show that typical strain map shown previously in Fig. 6-10b for uniaxial straining. It is therefore suggested that the previous biaxial deformation history contributes significantly to the subsequently applied uniaxial deformation. It is also expected that due to the significantly different deformation map seen by comparing Fig. 6-17ai and 17aii, there are significant strain redistributions which are suggested to account for the lower ductility seen under this strain path compared to path B [74]. It is hypothesized that strain redistribution can be related to the development of local hotspots under plastic deformation which potentially act as localization sites. This is unlike the behaviour seen in strain path B shown in Figs. 6-17bi and 6-17bii which show a comparatively better ductility to strain path A. The deformation maps suggest that the initial uniaxial strain path contributes little to the subsequent deformation evolution. Hence, the biaxial strain map developed after a uniaxial pre-strain closely resembles

the deformation map formed under a typical biaxial strain. Next, a comparative study on proportional straining is presented to evaluate the influence of hardening on the nature of lattice spacing distributions calculated using crystal plasticity.

6.4.2.Normalized lattice spacing changes for non-proportional strain paths calculated using crystal plasticity

The lattice spacing changes developed under non-proportional strain paths are presented for the differing hardening forms adopted. An analysis will further evaluate the ability to capture strain distributions using crystal plasticity and to relate the role of non-proportionality of strain to achievable ductility by drawing on the effects of pre-strains.

Fig. 6-18 shows the lattice spacing change for the range of strain paths shown in Fig. 6-17 under isotropic and self- hardening. As described above, strain path A comprises biaxial strain path A-1 and uniaxial strain path A-2 in order to reach a final strain state C. Fig. 6-18a shows the orientation dependent lattice spacing distribution at the end of each strain path segment (A-1 and A-2) for isotropic and self- hardening. Fig. 6-18b provides a similar analysis for strain path B under isotropic and self- hardening and finally, Fig. 6-18c compares the strain distribution at state C achieved by following path A or B. From Fig. 6-18a, it is seen that the resulting lattice spacing change at state C (path A-2) significantly differs from the distributions after the first deformation path, A-1. However, a different response is seen for path B shown in Fig. 6-18b which comprises uniaxial followed by biaxial deformation. In path B, only small changes are seen in the lattice spacing change by comparing paths A-1 and A-2. The consequence of these differences can be related to ductility experiments which show that increased ductility is achieved under a uniaxial pre-strain (path B) as opposed to a biaxial pre-strain (path A) [74].

Similarly to the experimental measurement which also shows significant lattice spacing redistribution in path A as opposed to B, it is hypothesized that the significant changes in the lattice spacing by following a biaxial pre-strain leads to local hotspots which drive localization/reduced ductility in path A.

Further, by comparing the lattice distributions at state C shown in Fig. 6-18c for the differing strain paths, it is clear that the nature of hardening adopted influences the resulting lattice spacing distribution especially under a uniaxial pre-strain and a subsequent biaxial deformation. This behaviour was also observed under proportional biaxial straining in section 6.3 which showed more pronounced differences depending on the nature of hardening adopted under biaxial compared with uniaxial deformation. This was attributed to the variety of potential slip systems that are activated and can influence local deformation due to a macroscopic biaxial strain. However, under uniaxial straining, slip is dependent on the orientation of favourably oriented slip systems with respect to the loading direction and it is anticipated that the dominant local slip system sets are unlikely to be significantly different irrespective of hardening. As a result, it is expected that differences due to hardening are more likely to be pronounced in path B as opposed to A as seen in Fig. 6-18.

A further analysis of the lattice spacings developed under the non-proportional strain paths considered is presented in Fig. 6-19. Similar to section 6.3, an upper and lower bound is specified for the lattice spacings calculated using crystal plasticity for the two forms of hardening considered. Note that the lattice spacing for the upper and lower bound azimuthal sectors are calculated using Eqs. 6-6 and 6-7. Also, the unbounded case which accounts for the contribution of all planes within a particular azimuthal sector is shown for the two forms of hardening considered. Finally, the crystal plasticity calculations are then compared with the experimentally

measured lattice spacing distribution. It is worth noting that all lattice spacings shown in Fig. 6-19 are obtained at the end of the second deformation phase in Fig. 6-16 i.e. A-2 and B-2.

Consider Fig. 6-19a which compares the lattice spacing changes for strain path A consisting of a biaxial pre-strain followed by uniaxial deformation. It is clear that the experimentally measured lattice spacing lies within the bounds set by the crystal plasticity simulations and closely matches the limits set by self- hardening. A similar behaviour can be seen in Fig. 6-19b in which the experimental measurement agrees closely with the upper bound of the crystal plasticity simulations. Although the exact nature of the response is not fully captured by the simulations due to reasons outlined earlier (and most especially the satisfaction of Bragg's condition), good qualitative agreement has been achieved with experiments. The effects of hardening types are shown and their influence on calculated lattice spacing under differing deformation pathways are shown.

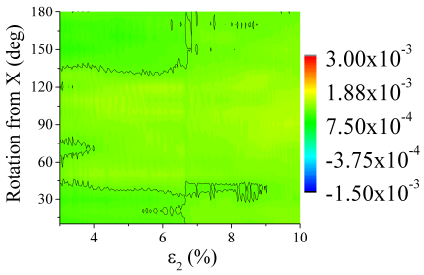
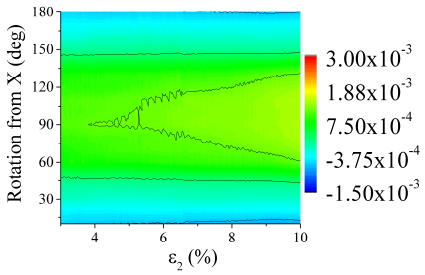
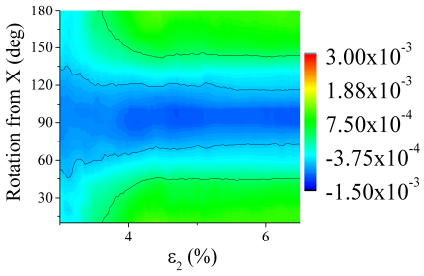
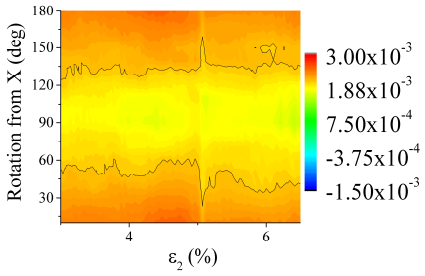
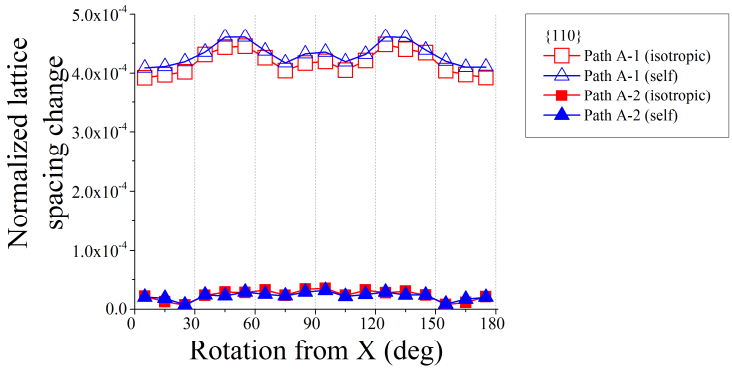
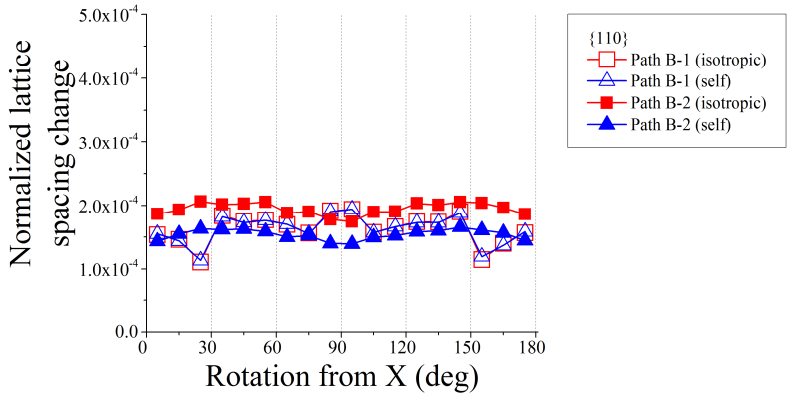
{110}	**Experimental texture, T-3 (exp) under non-proportional strain path A-1**	**Experimental texture, T-3 (exp) under non-proportional strain path B-1**
	(ai) 	(bi) 
	Experimental texture, T-3 (exp) under non-proportional strain path A-2	**Experimental texture, T-3 (exp) under non-proportional strain path B-2**
	(aii) 	(bii) 

Fig. 6-17: Experimentally measure normalized lattice spacing change for the experimental texture subjected to non-proportional straining. (ai) and (aii) represent the deformation map corresponding to strain path A-1 and A-2 shown in Fig. 6-16 and similarly, (bi) and (bii) are the deformation maps that correspond to strain paths B-1 and B-2 respectively.

(a)



(b)



(c)

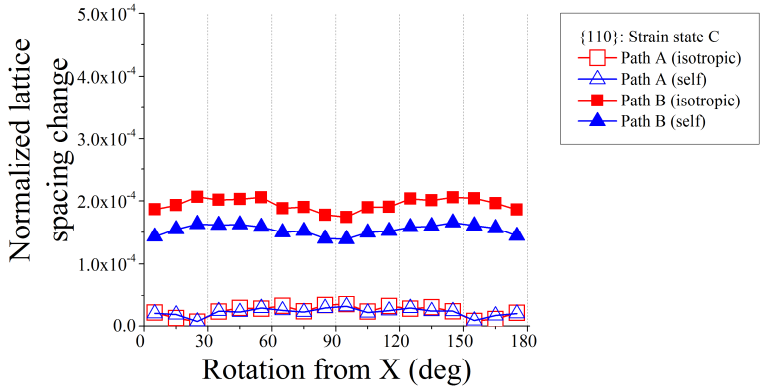
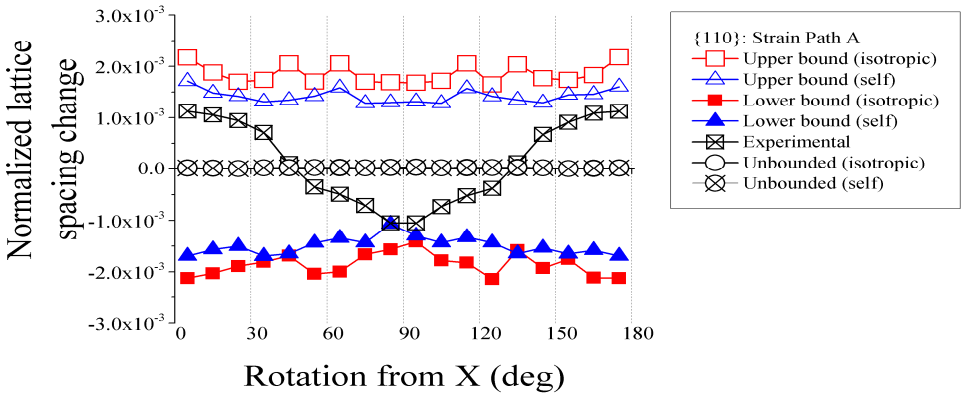


Fig. 6-18: The normalized lattice spacing change for the range of strain paths shown in Fig. 6-16 under isotropic and self-hardening. (a) and (b) show the lattice spacing change distribution under isotropic and self- hardening for strains paths A and B respectively and (c) compares the lattice spacing change distributions for paths A and B at an identical state C detailed in Fig. 6-16

(a)



(b)

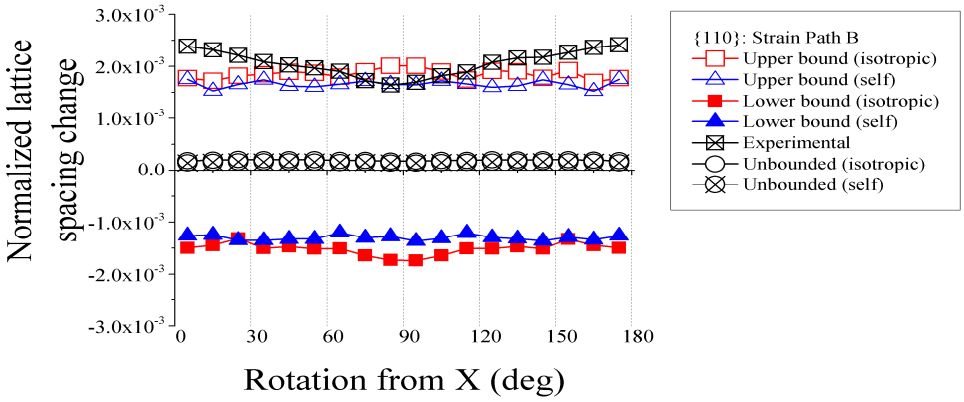


Fig. 6-19: Analysis of the calculated lattice spacing distribution under isotropic and self-hardening in comparison to experimental measurements for strain paths A (a) and B (b) illustrated in Fig. 6-16. Note that the upper bound and lower bound represent the ten largest and smallest lattice spacing for each orientation (rotation from X).

6.5. Conclusions

A methodology to calculate lattice spacing changes using crystal plasticity is presented. A systematic study was carried out to evaluate the influence of grain set size on lattice spacing changes. In addition, the consequence of satisfying Bragg's condition within the limits of crystal plasticity finite element framework was outlined. It was seen that increasing grain set size within the diffraction volume increased the accuracy of the resulting lattice spacing distributions. Also, satisfying Bragg's condition led to a significant reduction in quality of the lattice spacing distributions due to the relatively small number of grains modelled in comparison to experimental measurements. Whilst this is an oversimplification of the experimental method and its inherent assumptions, it was justified to be reasonable within the confines of the crystal plasticity framework adopted. For this reason, an unbounded case which assumed that all planes within the polycrystal contributed to diffraction was adopted.

Two forms of hardening were considered for a range of textures subjected to uniaxial and biaxial deformation. This followed a basic understanding of the response of individual planes to a simulated x-ray in single crystal ferritic steel. The resulting polycrystal deformation maps for both strain paths considered showed qualitative agreements with the experiment however, further analysis showed that the current assumption of allowing all planes contribute to the Debye Scherrer ring led to the quantitative differences. By adopting an upper and lower bound described previously, a closer agreement to experimental measurements was achieved. This further strengthened the notion that the selection processes for planes to diffract (Bragg's condition) plays a key role in the differences seen. Regardless, the reasonable qualitative agreement between experimental measurements and crystal plasticity calculations was sufficient to study lattice spacing changes under non-proportional strain paths.

Two non-proportional strain paths were considered which comprised a biaxial pre-strain followed by uniaxial deformation and uniaxial pre-strain followed by biaxial deformation. Experimentally, these equivalent non-proportional paths showed differing lattice spacing changes also seen in the crystal plasticity simulations. It was seen in both experimental and crystal plasticity simulations that the biaxial pre-strain had a more significant effect on the subsequent deformation history compared to a uniaxial pre-strain. The significant differences in lattice spacing changes seen by following a biaxial pre-strain were then related to earlier studies which showed that lower ductility was seen on this path compared to a uniaxial pre-strain.

It was hypothesized that significant strain re-distribution occurred when the deformation path was changed which potentially leads to nucleation of localization under plastic deformation. Furthermore, the influence of hardening was seen to influence lattice spacing distributions and was also sensitive to texture and the nature of deformation. Biaxial deformation was observed to influence hardening more compared to uniaxial and this was attributed to the variability of slip systems that can be activated under this deformation path compared to uniaxial straining.

Chapter VII

7. Conclusions and Future Work

7.1. Conclusions

This thesis investigated the role of texture, hardening and non-proportionality of strain on lattice spacing distributions in ferritic steel polycrystals. First, it was shown that texture and nature of hardening adopted (self- vs isotropic) affected the resulting dislocation distributions. Texture was shown to be important in the predicted response to non-proportional strain paths especially under uniaxial non-proportional straining and the differences in dislocation distributions were more pronounced under non-proportional paths to a final uniaxial state compared to a final biaxial state.

Subsequently, the consequences of non-proportional straining on ductility were investigated for a range of non-proportional strain paths using the differing hardening types- isotropic vs anisotropic self- hardening. The results showed that depending on the texture, non-proportional straining can improve or conversely lower ductility. The most significant increases in ductility were achievable under non-proportional uniaxial straining as opposed to biaxial strain paths.

In order to further understand non-proportionality effects and to calibrate the hardening rule adopted using experimental data, a methodology was developed to evaluate peak broadening due to lattice spacing distributions in polycrystals by accounting for the contribution of elastic strains and geometrically necessary dislocations (GNDs). This study showed that whilst elastic strains were important, peak broadening is typically dominated by the contribution from GNDs. The study of lattice spacing distributions then provided a basis to simulate x-ray diffraction and

directly compare crystal plasticity lattice spacings to experimentally measured lattice strain distributions.

In the experiments, planes that satisfy Bragg's condition within the metallic sample diffract the incoming x-ray beam to a detector. Planes of a particular orientation diffract to particular regions on the detector enabling the extraction of information on the average lattice spacing changes of a family of planes. This study showed that only qualitative agreements between experimental lattice spacing distributions can be achieved in comparison with crystal plasticity simulations. This was attributed to the fact that Bragg's condition which is crucial to the plane diffraction process was ignored. Experimentally, the outputted diffracted beam is a superposition of reflected waves from the diffracting plane which was unaccounted for in this model and lead to the differences seen.

The qualitative agreements was however sufficient to adopt this methodology to investigate non-proportionality of strain. It was shown that differing lattice spacing distributions were achieved by following differing strain paths to an identical strain state. This also compared well with earlier work in this thesis which showed that differing dislocation distributions are achieved by following differing non-proportional strain paths to an identical strain state. It was also shown in that biaxial pre-strain had more influence on the subsequent deformation history compared to uniaxial pre-strain. Further, it was hypothesized from the lattice spacing distributions that the developed elastic distributions contributed to differences in ductility achieved in these two paths. Experiments show that higher ductility is achievable under a uniaxial pre-strain as opposed to a biaxial pre-strain. This was attributed to the effects of pronounced strain re-distribution seen in the latter compared to the former perhaps leading strain gradients and accelerated localization.

Overall, this thesis has so far provided a useful understanding of the benefits of non-proportionality of strain and has developed useful techniques that can be used to easily assess whether a particular strain path is beneficial or detrimental to forming.

7.2. Future work

The findings from this study have opened more potential research paths for the future. Four potential paths are;

1. To fully understand the basis for differences in ductility achieved by following differing non-proportional paths to an identical strain state. It has been experimentally observed that biaxial pre-strain followed by uniaxial loading showed lower ductility compared to uniaxial pre-strain followed by biaxial straining. Whilst it has been hypothesized in this thesis that strain re-distribution led to the differences seen, it is imperative to evaluate the evolution of geometrically necessary dislocations (GNDs) for the non-proportional strain paths considered. This will enable a detailed micromechanical investigation of the influence of each loading path on the subsequent deformation history and potentially give credence to the strain re-distribution hypothesis presented here.

   Further material characterization using neutron diffraction will enable the measurement of GNDs and its evolution. Using the methodology presented in this thesis, the lattice spacing changes due to GNDs can be calculated and in conjunction with experiment, the crystal plasticity model can be calibrated. In addition, similar to the elastic strain distributions presented in this thesis, the distribution of GNDs on particular planes will give further insight into the effects of strain distributions for differing non-proportional strain paths.

2. To optimize the non-proportional strain paths and evaluate the most beneficial paths. In the industry today, non-proportional strain paths are avoided due to the associated risks and lack of in-depth knowledge of ways of maximizing benefits. The research presented here has ignited this field of study by providing some understanding of the potential benefits that can be achieved by following non-proportional strain paths. On this basis, and with further understanding of the micromechanics of non-proportionality, it is possible to further develop the tools presented in this thesis to speedily simulate whether a particular strain path will be advantageous. Such a tool will couple the role of texture, hardening and lattice strain distributions as well as their evolution to assess ductility and inform the design process about the advantages of adopting that strain path.
3. To improve the modelling tools and capabilities in order to fully capture the micromechanical response of materials. For example, crystal plasticity finite element can only model a small number of grains denoted as a representative volume. It is currently unclear the exact number of grains that satisfies the requirement of a representative volume. Also, grain boundary effects and boundary conditions associated with the modelling can be improved. Grain boundaries are complicated and it unclear how they will influence the mechanical response. Similarly, boundary conditions are important, hence, it is important to understand and account for their effects. The dislocation framework adopted here can also be improved to account for dislocation annihilation and path dependence during deformation. Furthermore, it is currently assumed that grain morphology effects are negligible however, a model that accounts for grain morphology in addition to the range of improvements outlined above will provide a more detailed understanding of non-proportionality effects in ferritic steel.

4. Finally, other forms of steel should be investigated. There is empirical evidence to show that dual phase steels as opposed to the currently adopted single phase steel shows differing mechanical behavior especially under non-proportional straining. It is hypothesized that the different structure of the second phase (typically FCC) will affect the micromechanics of the parent material structure leading to differing lattice strain distributions and potentially different response with respect to achievable ductility.

Whilst some questions remain open, this thesis has contributed significantly to our understanding of improving achievable ductility of high strength steels used in auto industry. The tools developed and range of detailed micromechanical investigations have provided insights into texture and hardening effects under differing strain paths. It is therefore envisaged that the benefits of non-proportionality of strain should be maximized and offers a lot of promise for the materials forming industry.

Appendix A: Lattice spacing parameters for triclinic crystal

The formulae for calculating lattice spacing in a triclinic crystal obtained from Cullity and Stock [61] are given below.

$$d_{hkl} = \sqrt{\frac{V^2}{S_{11}h^2 + S_{22}k^2 + S_{33}l^2 + 2S_{12}hk + 2S_{23}kl + 2S_{13}hl}}$$

$$V = a'b'c'\sqrt{1 - cos^2\alpha' - cos^2\beta' - cos^2\gamma' + 2cos\,\alpha' cos\,\beta' cos\gamma'}$$

$$S_{11} = b'^2 c'^2 sin^2\alpha'$$

$$S_{22} = a'^2 c'^2 sin^2\beta'$$

$$S_{33} = a'^2 b'^2 sin^2\gamma'$$

$$S_{12} = a'b'c'^2 cos\,\alpha' cos\,\beta' - cos\,\gamma'$$

$$S_{23} = a'^2 b'c' cos\,\gamma' cos\,\beta' - cos\,\alpha'$$

$$S_{33} = a'b'^2 c' cos\,\alpha' cos\,\gamma' - cos\,\beta'$$

Appendix B: Strain gradient approximation method

The plastic strain gradient within any element is calculated using a non-local approach such that the deformation gradient is assumed constant within an element and the gradient is obtained by considering neighboring elements as shown schematically in Fig. B1. The gradient for a component of the plastic deformation gradient e.g $\boldsymbol{F}_{11}^{p}$, in an element i shown in Fig. B1 is obtained by fitting a polynomial for plastic strain to its nearest neighbours in the three orthogonal directions. Hence in the X- direction, the elements considered are $i+a$ and $i-a$, in the Y-direction, the elements considered are $i+b$ and $i-b$ and corrspondingly, in the Z-direction, the elements considered are $i+c$ and $i-c$. For the case where the $i \pm a$ or $i \pm b$ or $i \pm c$ does not exist such as at free surfaces of the model, the plastic strain gradient is estimated using, for example, $i-2a$, $i-2b$ and $i-2c$ respectively.

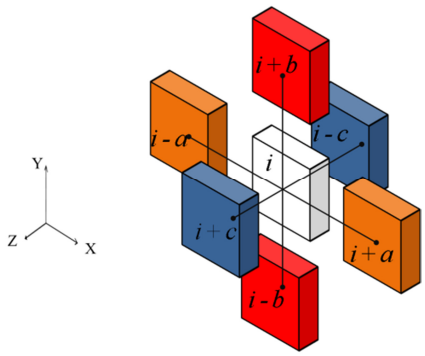


Fig. B 1: Schematic diagram showing the non-local approach adopted to obtain plastic strain gradient approximations.

Further, the gradient in the appropriate direction is obtained by differentiating the fitted piecewise Hermite interpolating polynomial defined by the three point locations, i.e. the centroid coordinates of the selected element and the corresponding state value of interest.

Appendix C: Justification of calculation of the contribution to lattice distortion from the projection of the Burger's vector discontinuity onto a plane

The Burger's vector discontinuity circuit is calculated such that $\boldsymbol{B} = \int \text{curl}(\boldsymbol{F}^{\text{p}})\boldsymbol{n}dS \cong \text{curl}(\boldsymbol{F}^{\text{P}})\boldsymbol{n}\Delta A$. The normalized Burger's vector discontinuity is given by $\boldsymbol{B}^{l} \cong \text{curl}(\boldsymbol{F}^{\text{P}})\boldsymbol{n}\ \frac{\Delta A}{L}$. And for a given plane with normal $\boldsymbol{n}_k$, $\boldsymbol{B}^{l}{}_{k} \cong \text{curl}(\boldsymbol{F}^{\text{P}})\boldsymbol{n}_k \frac{\Delta A_k}{L_k}$. Consider Fig. C1, $\boldsymbol{B}^{l}{}_{1} \cong \text{curl}(\boldsymbol{F}^{\text{P}})\boldsymbol{e}_1 \frac{\Delta A}{L}$ and $\boldsymbol{B}^{l}{}_{2} \cong \text{curl}(\boldsymbol{F}^{\text{P}})\boldsymbol{e}_2 \frac{\Delta A}{L}$. The edge type contribution to the lattice distortion in the 2- direction ($\frac{\Delta a^e}{a_0}$) is given by $\frac{\Delta a^e}{a_0} = \boldsymbol{B}^{l}{}_{1} \cdot \boldsymbol{e}_1$. The screw type contribution in the 2- direction is given by $\frac{\Delta a^s}{a_0} = \boldsymbol{B}^{l}{}_{2} \cdot \boldsymbol{e}_1$, so that for the planar dislocation shown, the net lattice distortion is $\frac{\Delta a}{a_0} = \boldsymbol{B}^{l}{}_{1} \cdot \boldsymbol{e}_1 + \boldsymbol{B}^{l}{}_{2} \cdot \boldsymbol{e}_1$. If out of plane dislocations are permitted, this can be expressed in general as $\frac{\Delta a}{a_0} = \boldsymbol{B}^{l}{}_{1} \cdot \boldsymbol{e}_1 + \boldsymbol{B}^{l}{}_{2} \cdot \boldsymbol{e}_1 + \boldsymbol{B}^{l}{}_{3} \cdot \boldsymbol{e}_1$.

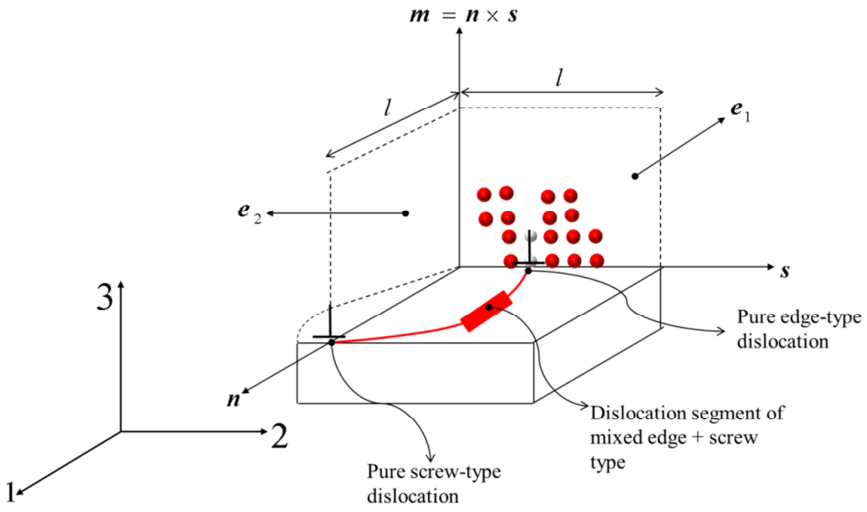


Fig. C 1: Schematic diagram showing the non-local approach adopted to obtain plastic strain gradient approximations.

Appendix D: Relationship between the GND deformation tensor d^{gnd} and the Burger's tensor, G

From Eq. (5-9), in the undeformed crystallographic configuration, the lattice distortion tensor, $\boldsymbol{d}^{\mathrm{gnd}}$ is given by $\boldsymbol{d}^{\mathrm{gnd}} = \begin{pmatrix} \boldsymbol{B}^{l}{}_{1} \cdot \boldsymbol{e}'_1 & \boldsymbol{B}^{l}{}_{2} \cdot \boldsymbol{e}'_1 & \boldsymbol{B}^{l}{}_{3} \cdot \boldsymbol{e}'_1 \\ \boldsymbol{B}^{l}{}_{1} \cdot \boldsymbol{e}'_2 & \boldsymbol{B}^{l}{}_{2} \cdot \boldsymbol{e}'_2 & \boldsymbol{B}^{l}{}_{3} \cdot \boldsymbol{e}'_2 \\ \boldsymbol{B}^{l}{}_{1} \cdot \boldsymbol{e}'_3 & \boldsymbol{B}^{l}{}_{2} \cdot \boldsymbol{e}'_3 & \boldsymbol{B}^{l}{}_{3} \cdot \boldsymbol{e}'_3 \end{pmatrix}$. Now, the Burgers' tensor, $\boldsymbol{G}$, in the undeformed configuration is [75]$\boldsymbol{G} = \mathrm{curl}(\boldsymbol{F}^{\mathrm{P}})$. Hence, the normalized Burger's discontinuity $\boldsymbol{B}^{l}$ is given by $\boldsymbol{B}^{l} = \mathrm{curl}(\boldsymbol{F}^{\mathrm{P}})\boldsymbol{n}\frac{\Delta A}{L} = \boldsymbol{G}\boldsymbol{n}\frac{\Delta A}{L}$. The normals $\boldsymbol{n}$ may be expressed in the local lattice orientation as $\boldsymbol{n} = \boldsymbol{R}_{\boldsymbol{0}}^{\mathrm{c^T}}\boldsymbol{e}'$. Thus, $\boldsymbol{B}^{l} = \boldsymbol{G}\boldsymbol{R}_{0}^{\mathrm{c^T}}\boldsymbol{e}'\frac{\Delta A}{L}$, and the Burger's discontinuity in the three orthogonal planes with normals $\boldsymbol{e}'_1$, $\boldsymbol{e}'_2$ and $\boldsymbol{e}'_3$ in the local lattice orientation are $\boldsymbol{B}_{k}^{l} = \boldsymbol{G}\boldsymbol{R}_{0}^{\mathrm{c^T}}\boldsymbol{e}'_k\frac{\Delta A_k}{L_k}$. Therefore, $\boldsymbol{d}^{\mathrm{gnd}} = \boldsymbol{G}\boldsymbol{R}_{0}^{\mathrm{c^T}}\frac{\Delta A_k}{L_k}$. And the lattice distortion gradient $\boldsymbol{F}^{\mathrm{gnd}} = \boldsymbol{I} + \boldsymbol{d}^{\mathrm{gnd}} = \boldsymbol{I} + \boldsymbol{G}\boldsymbol{R}_{0}^{\mathrm{c^T}}\frac{\Delta A}{L}$. The GND deformation tensor, $\boldsymbol{d}^{\mathrm{gnd}}$, is therefore the Burger's tensor but rotated into the local lattice orientation.

Appendix E: Diffraction peaks due to strains in a 2-D spatial field

Calculation of edge dislocation stress fields

The strain fields are calculated for a 2-D spatial field using stress equations summarized in Hull and Bacon [76]. The components of stress tensor (σ) are given for an edge dislocation using the following equations:

$\sigma_{xx} = -Dy\frac{3x^2+y^2}{(x^2+y^2)^2}$, $\sigma_{yy} = Dy\frac{x^2-y^2}{(x^2+y^2)^2}$, $\sigma_{xy} = \sigma_{yx} = Dx\frac{x^2-y^2}{(x^2+y^2)^2}$, $\sigma_{zz} = \upsilon(\sigma_{xx} + \sigma_{yy})$ and

$\sigma_{xz} = \sigma_{zx} = \sigma_{yz} = \sigma_{zy} = 0$, where $= \frac{Gb}{2\pi(1-\upsilon)}$.

The stress tensor is written $\boldsymbol{\sigma} = \begin{pmatrix} \sigma_{xx} & \sigma_{xy} & \sigma_{xz} \\ \sigma_{yx} & \sigma_{yy} & \sigma_{yz} \\ \sigma_{zx} & \sigma_{zy} & \sigma_{zz} \end{pmatrix}$, Poisson's ratio, υ, Burger's vector length, *b,* shear modulus, *G* and the 2-D spatial coordinates are denoted by *x* and *y*. The material properties used here are detailed in Table E1. In order to calculate the broadening due to the strain field, the elastic strain tensor ($\boldsymbol{\varepsilon}$) is calculated from Hooke's law and the deformation tensor, $\boldsymbol{F^e} = I + \boldsymbol{\varepsilon}$ is obtained.

Table E 1: Properties used to calculate strain fields

G (GPa)	*b* (Angstroms)	υ	*x* (Angstroms)	*y* (Angstroms)
82	2.87	0.3	5000	5000

References

1. Keeler, B., *Plastic instability and fracture in sheets stretched over rigid punches.* Trans.ASM, 1963. **56**: p. 25-.

2. Yoshida, K., T. Kuwabara, and M. Kuroda, *Path-dependence of the forming limit stresses in a sheet metal.* International Journal of Plasticity, 2007. **23**(3): p. 361-384.

3. Kuwabara, T., et al., *Anisotropic plastic deformation of extruded aluminum alloy tube under axial forces and internal pressure.* International Journal of Plasticity, 2005. **21**(1): p. 101-117.

4. Betten, J. and M. Waniewski, *The strain path dependence of multiaxial cyclic hardening behaviour.* Forschung Im Ingenieurwesen-Engineering Research, 1998. **64**(9): p. 231-244.

5. Arsenlis, A. and D.M. Parks, *Crystallographic aspects of geometrically-necessary and statistically-stored dislocation density.* Acta Materialia, 1999. **47**(5): p. 1597-1611.

6. Marciniak, Z. and K. Kuczynski, *Limit strains in the processes of stretch-forming sheet metal.* International Journal of Mechanical Sciences, 1967. **9**(9): p. 609-620.

7. Nurcheshmeh, M. and D.E. Green, *Prediction of sheet forming limits with Marciniak and Kuczynski analysis using combined isotropic nonlinear kinematic hardening.* International Journal of Mechanical Sciences, 2011. **53**(2): p. 145-153.

8. Sowerby, R. and J.L. Duncan, *Failure in sheet metal in biaxial tension.* International Journal of Mechanical Sciences, 1971. **13**(3): p. 217-229.

9. Marin, T., P.R. Dawson, and M.A. Gharghouri, *Orientation dependence of stress distributions in polycrystals deforming elastoplastically under biaxial loadings.* Journal of the Mechanics and Physics of Solids, 2012. **60**(5): p. 921-944.

10. Ma, A., F. Roters, and D. Raabe, *Studying the effect of grain boundaries in dislocation density based crystal-plasticity finite element simulations.* International Journal of Solids and Structures, 2006. **43**(24): p. 7287-7303.

11. Yalcinkaya, T., W.A.M. Brekelmans, and M.G.D. Geers, *A composite dislocation cell model to describe strain path change effects in BCC metals.* Modelling and Simulation in Materials Science and Engineering, 2009. **17**(6).

12. Peeters, B., et al., *A crystal plasticity based work-hardening/softening model for b.c.c. metals under changing strain paths.* Acta Materialia, 2000. **48**(9): p. 2123-2133.

13. Hoc, T. and S. Forest, *Polycrystal modelling of IF-Ti steel under complex loading path.* International Journal of Plasticity, 2001. **17**(1): p. 65-85.

14. Tarigopula, V., et al., *Elastic-plastic behaviour of dual-phase, high-strength steel under strain-path changes.* European Journal of Mechanics a-Solids, 2008. **27**(5): p. 764-782.

15. Mollica, F., et al., *Implicit constitutive equations in the modeling of bimodular materials: An application to biomaterials.* Computers & Mathematics with Applications, 2007. **53**(2): p. 209-218.

16. Signorelli, J.W., M.A. Bertinetti, and P.A. Turner, *Predictions of forming limit diagrams using a rate-dependent polycrystal self-consistent plasticity model.* International Journal of Plasticity, 2009. **25**(1): p. 1-25.

17. Viatkina, E.M., W.A.M. Brekelmans, and M.G.D. Geers, *A crystal plasticity based estimate for forming limit diagrams from textural inhomogeneities.* Journal of Materials Processing Technology, 2005. **168**(2): p. 211-218.

18. Wu, P.D., et al., *Evaluation of anisotropic yield functions for aluminum sheets.* International Journal of Plasticity, 2003. **19**(1): p. 121-138.

19. Sai, K., L. Taleb, and G. Cailletaud, *Numerical simulation of the anisotropic behavior of 2017 aluminum alloy.* Computational Materials Science, 2012. **65**(0): p. 48-57.

20. Honeycombe, R.W.K., *The plastic deformation of metals*. 1968, London: Edward Arnold. xiv, 477.

21. Schaffer, J.P., *The science and design of engineering materials*. 2nd. ed. 1999, Boston ; London: WCB McGraw-Hill. xx, 826.

22. Roters, F., *Crystal plasticity finite element methods in materials science and engineering*, Weinheim: Wiley-VCH. xi, 197.

23. Ashby, M.F., *The deformation of plastically non-homogeneous materials.* Philosophical Magazine, 1970. **21**(170): p. 399-424.

24. Kocks, U.F., *Relation between Polycrystal Deformation and Single-Crystal Deformation.* Metallurgical Transactions, 1970. **1**(5): p. 1121-&.

25. Thompson, A.W. and M.I. Baskes, *The influence of grain size on the work hardening of face-center cubic polycrystals.* Philosophical Magazine, 1973. **28**(2): p. 301-308.

26. Ashmawi, W.M. and M.A. Zikry, *Grain-boundary interfaces and void interactions in porous aggregates.* Philosophical Magazine, 2003. **83**(31-34): p. 3917-3944.

27. Evers, L.P., W.A.M. Brekelmans, and M.G.D. Geers, *Scale dependent crystal plasticity framework with dislocation density and grain boundary effects.* International Journal of Solids and Structures, 2004. **41**(18-19): p. 5209-5230.

28. Nye, J.F., *Some Geometrical Relations in Dislocated Crystals.* Acta Metallurgica, 1953. **1**(2): p. 153-162.

29. Volk, W. and P. Hora, *New algorithm for a robust user-independent evaluation of beginning instability for the experimental FLC determination.* International Journal of Material Forming, 2011. **4**(3): p. 339-346.

30. Situ, Q., M.K. Jain, and D.R. Metzger, *Determination of forming limit diagrams of sheet materials with a hybrid experimental-numerical approach.* International Journal of Mechanical Sciences, 2011. **53**(9): p. 707-719.

31. Pepelnjak, T., A. Petek, and K. Kulzman, *Analysis of the forming limit diagram in digital environment.* Sheet Metal 2005, 2005. **6-8**: p. 697-704.

32. Petek, A., T. Pepelnjak, and K. Kuzman, *An improved method for determining a forming limit diagram in the digital environment.* Strojniski Vestnik-Journal of Mechanical Engineering, 2005. **51**(6): p. 330-345.

33. Butuc, M.C., et al., *Plastic Instability in Complex Strain Paths Predicted by Advanced Constitutive Equations.* 8th International Conference and Workshop on Numerical Simulation of 3d Sheet Metal Forming Processes (Numisheet 2011), Pts a and B, 2011. **1383**: p. 194-201.

34. Jie, M., et al., *Forming limit diagrams of strain-rate-dependent sheet metals.* International Journal of Mechanical Sciences, 2009. **51**(4): p. 269-275.

35. Stoughton, T.B. and J.W. Yoon, *A new approach for failure criterion for sheet metals.* International Journal of Plasticity, 2011. **27**(3): p. 440-459.

36. Firat, M., *A numerical analysis of sheet metal formability for automotive stamping applications.* Computational Materials Science, 2008. **43**(4): p. 802-811.

37. Cullity, B.D. and S.R. Stock, *Elements of x-ray diffraction*. 3rd edition, New international edition. ed. ii, 650 pages.

38. Nervo, L., et al., *Comparison between a near-field and a far-field indexing approach for characterization of a polycrystalline sample volume containing more than 1500 grains.* Journal of Applied Crystallography, 2014. **47**: p. 1402-1416.

39. Nuffield, E.W., *X-ray diffraction methods*. 1966, New York ; London: Wiley. xii, 409 p.

40. Woolfson, M.M., *An introduction to X-ray crystallography*. 2nd ed. 1997, Cambridge: Cambridge University Press. xii, 402 p.

41. Poulsen, H.F., et al., *Three-dimensional maps of grain boundaries and the stress state of individual grains in polycrystals and powders.* Journal of Applied Crystallography, 2001. **34**: p. 751-756.

42. Wong, S.L., et al., *A framework for generating synthetic diffraction images from deforming polycrystals using crystal-based finite element formulations.* Computational Materials Science, 2013. **77**: p. 456-466.

43. Withers, P.J., et al., *Recent advances in residual stress measurement.* International Journal of Pressure Vessels and Piping, 2008. **85**(3): p. 118-127.

44. Pagliaro, P., et al., *Known Residual Stress Specimens Using Opposed Indentation.* Journal of Engineering Materials and Technology-Transactions of the Asme, 2009. **131**(3).

45. Cihak, U., et al., *Characterization of residual stresses in turbine discs by neutron and high-energy X-ray diffraction and comparison to finite element modeling.* Materials Science and Engineering a-Structural Materials Properties Microstructure and Processing, 2006. **437**(1): p. 75-82.

46. Dye, D., et al., *Diffraction strain measurements for the characterization of residual stresses in welds for gas turbine applications.* Trends in Welding Research, Proceedings, 2003: p. 878-885.

47. Webster, P.J., et al., *Synchrotron X-ray residual strain scanning of a friction stir weld.* Journal of Strain Analysis for Engineering Design, 2001. **36**(1): p. 61-70.

48. Korsunsky, A.M., et al., *Probing Deformation Substructure by Synchrotron X-ray Diffraction and Dislocation Dynamics Modelling.* Journal of Nanoscience and Nanotechnology, 2010. **10**(9): p. 5935-5950.

49. Oddershede, J., et al., *Measuring the stress field around an evolving crack in tensile deformed Mg AZ31 using three-dimensional X-ray diffraction.* Acta Materialia, 2012. **60**(8): p. 3570-3580.

50. Wilkinson, A.J. and T.B. Britton, *Strains, planes, and EBSD in materials science.* Materials Today, 2012. **15**(9): p. 366-376.

51. Lee, E.H., *Elastic-Plastic Deformation at Finite Strains.* Journal of Applied Mechanics, 1969. **36**(1): p. 1-&.

52. Hill, R. and J.R. Rice, *Constitutive Analysis of Elastic-Plastic Crystals at Arbitrary Strain.* Journal of the Mechanics and Physics of Solids, 1972. **20**(6): p. 401-&.

53. McGinty, R.D. and D.L. McDowell, *Application of multiscale crystal plasticity models to forming limit diagrams.* Journal of Engineering Materials and Technology-Transactions of the Asme, 2004. **126**(3): p. 285-291.

54. Serenelli, M.J., M.A. Bertinetti, and J.W. Signorelli, *Study of limit strains for FCC and BCC sheet metal using polycrystal plasticity.* International Journal of Solids and Structures, 2010. **48**: p. 1109-1119.

55. Huang, Y., *A user-material subroutine incorporating single crystal plasticity in the ABAQUS finite element program.* Harvard Internal report, 1991.

56. Harewood, F.J. and P.E. McHugh, *Comparison of the implicit and explicit finite element methods using crystal plasticity.* Computational Materials Science, 2007. **39**(2): p. 481-494.

57. Schmitt, J.H., E. Aernoudt, and B. Baudelet, *Yield Loci for Polycrystalline Metals without Texture.* Materials Science and Engineering, 1985. **75**(1-2): p. 13-20.

58. Gerken, J.M. and P.R. Dawson, *A crystal plasticity model that incorporates stresses and strains due to slip gradients.* Journal of the Mechanics and Physics of Solids, 2008. **56**(4): p. 1651-1672.

59. Clayton, J.D., D.J. Bammann, and D.L. McDowell, *A geometric framework for the kinematics of crystals with defects.* Philosophical Magazine, 2005. **85**(33-35): p. 3983-4010.

60. Clayton, J.D., C.S. Hartley, and D.L. McDowell, *The missing term in the decomposition of finite deformation.* International Journal of Plasticity. **52**(0): p. 51-76.

61. Cullity, B.D. and S.R. Stock, *Elements of X-ray diffraction*. 3rd ed. 2001, Upper Saddle River, N.J.: Prentice Hall. xviii, 678 p.

62. Collins, D., *Strain path effects in ferritic steel polycrystals.* University of Oxford Internal Report, 2013.

63. Guruprasad, P.J. and A.A. Benzerga, *Size effects under homogeneous deformation of single crystals: A discrete dislocation analysis.* Journal of the Mechanics and Physics of Solids, 2008. **56**(1): p. 132-156.

64. Britton, T.B., *Calculating GND densities using a linear strain gradient approach*, T. Erinosho, Editor. October, 2013: London.

65. Kanjarla, A.K., et al., *Study of internal lattice strain distributions in stainless steel using a full-field elasto-viscoplastic formulation based on fast Fourier transforms.* Acta Materialia, 2012. **60**(6-7): p. 3094-3106.

66. Neil, C.J., et al., *Modeling lattice strain evolution at finite strains and experimental verification for copper and stainless steel using in situ neutron diffraction.* International Journal of Plasticity, 2010. **26**(12): p. 1772-1791.

67. Dawson, P.R., D.E. Boyce, and R.B. Rogge, *Correlation of diffraction peak broadening to crystal strengthening in finite element simulations.* Materials Science and Engineering a-Structural Materials Properties Microstructure and Processing, 2005. **399**(1-2): p. 13-25.

68. Erinosho, T.O. and F.P.E. Dunne, *Lattice strain distributions due to elastic distortions and GND development in polycrystals.* Journal of the Mechanics and Physics of Solids, 2014. **67**: p. 62-86.

69. Dawson, P., et al., *Computing residual stresses in polycrystals following plastic straining.* Simulation of Materials Processing: Theory, Methods and Applications, 1998: p. 323-328.

70. Miller, M.P., et al., *Experimental measurement of lattice strain pole figures using synchrotron x rays.* Review of Scientific Instruments, 2005. **76**(11).

71. Miller, M.P., et al., *Measuring and modeling distributions of stress state in deforming polycrystals.* Acta Materialia, 2008. **56**(15): p. 3927-3939.

72. Obstalecki, M., et al., *Quantitative analysis of crystal scale deformation heterogeneity during cyclic plasticity using high-energy X-ray diffraction and finite-element simulation.* Acta Materialia, 2014. **75**: p. 259-272.

73. Erinosho, T.O., A.C.F. Cocks, and F.P.E. Dunne, *Coupled effects of texture, hardening and non-proportionality of strain on ductility in ferritic steel.* Computational Materials Science, 2013. **80**: p. 113-122.

74. Collins, D.M., *Ductility under non-proportional strain paths in ferritic steel.*

75. Cermelli, P. and M.E. Gurtin, *Geometrically necessary dislocations in viscoplastic single crystals and bicrystals undergoing small deformations.* International Journal of Solids and Structures, 2002. **39**(26): p. 6281-6309.

76. Hull, D. and D.J. Bacon, *Introduction to dislocations*. 4th ed. 2001, Oxford: Butterworth Heinemann. vii, 242 p.